

Single Emitters Coupled to Bow-Tie Nano-Antennas

INAUGURALDISSERTATION

ZUR ERLANGUNG DER WÜRDE EINES DOKTORS DER PHILOSOPHIE
VORGELEGT DER
PHILOSOPHISCH - NATURWISSENSCHAFTLICHEN FAKULTÄT DER
UNIVERSITÄT BASEL

von

Javad Najafabadi Farahani
aus Teheran, Iran

Institut für Physik
Universität Basel



Basel, 2006

Vorgelegt der Philosophisch-Naturwissenschaftlichen Fakultät auf Antrag
der Herren Professoren:

Prof. Dr. B. Hecht

Prof. Dr. D.W. Pohl

Dr. Rer. Nat. H.-J. Eisler

Prof. Dr. H.-J. Güntherodt

Basel, den 30 Jaunuar 2006

Prof. Dr. H.-J. Wirz, Dekan

Abstract

Approaching a metallic tip to a single quantum emitter quenches the photoluminescence by opening non-radiative decay channels for the excited-state. This is one of the main problems in nano-optics research which prohibits optical studies on single emitters in contact with the tip with high resolution and high sensitivity. In this thesis I have shown that a bowtie nanoantenna can be used to overcome the quenching problem at the single chromophore level. Bowtie antenna tip interacts with the dipole of the single emitter. This is most probably the first study on this type of measurements which opens new pathways for many disciplines. Semiconductor nanocrystals were selected as a single emitter system due to their relatively high photo-stability. Based on fluorescence confocal studies, saturation behavior of single CdSe{ZnS} nanocrystal (NC) is studied under one- and two-photon excitation. In one-photon excitation (1PE) laser wavelength of 532 nm and in two-photon excitation (2PE) laser wavelength of 830 nm were used to excite the fluorophore. Due to the broad distribution in photoluminescence (PL) intensity of nanocrystals, power dependence studies were done based on an average over ~ 90 nanocrystals. Using focused ion beam, bowtie antennas are sculptured at the apices of silicon nitride AFM tips, which were fully-coated with a homogeneous layer of 40 nm of aluminum film. Details of structuring procedures used to fabricate well-defined bowtie antennas with smallest possible feedgaps are described. Interaction of bowtie nanoantennas with single semiconductor nanocrystals, is investigated using PL intensity and excited-state lifetime of the nanocrystal as two intrinsic signatures of the single emitter. Proximity of the feedgap of a bowtie nanoantenna to a single nanocrystal under one-photon excitation leads to enhanced emission in addition to enhanced excitation. This effect is shown, by increasing the PL intensity of the nanocrystal and shortened lifetime, in contact with the bowtie antenna feedgap. These results were compared with a fully-coated tip which lead to complete quenching of the nanocrystal PL. Thus, the observed effects in PL intensity and lifetime of the nanocrystal in contact with the antenna are originated from the metallic nanostructure. Under two-photon excitation, PL intensity is enhanced but there is no change in the lifetime of the nanocrystal in contact with the bowtie antenna. This is caused by enhanced excitation through the antenna, induced by enlarging the absorption cross section of the nanocrystal in contact with the antenna. Since, fluorescence of single nanocrystal in contact with the bowtie antenna is "*not quenched*", more detailed studies on their interaction were performed. Under two-photon excitation absorption cross section of one nanocrystal was measured with and without the presence of antenna. Free nanocrystal showed a two-photon absorption cross section in the order of $6.3 \times 10^{-37} \text{cm}^4 \text{s}$ which in contact with the bowtie antenna increased to $20.2 \times 10^{-37} \text{cm}^4 \text{s}$. This proves that enhanced excitation observed in 2PE is caused by a larger absorption cross section of the system induced by the antenna structure. Emission polarization of nanocrystals was studied under 1PE

using polarization microscopy. From these studies, in- and out-of-plane angles as well as the absolute value of the projection of the transition dipole moment on the sample plane were determined. Results showed in contact with the bowtie antenna, the in-plane angle turns towards the orientation of the antenna. This is induced by the strong dipole of the antenna in contact with the nanocrystal. Moreover, modulation depth and the absolute value of the transition dipole were increased dramatically in contact with the bowtie nanostructure. The results show that antenna/NC system has a highly polarized emission, whose polarization direction is determined by the antenna dipole. Photon antibunching of nanocrystals under 1PE was done with and without the presence of the antenna tip. Shorter lifetime of the excited-state in contact with the bowtie antenna immediately appears in antibunching results. This shows that the "dead time" for single photon generation, caused by excitation-recombination cycles, is much shorter in contact with the antenna. Therefore, a nanocrystal in contact with the bowtie antenna is a more efficient single photon source. Moreover, taking into account the emission polarization of the antenna/NC system, polarization of single photons generated from the nanocrystal in contact with the antenna can be tuned by antenna orientation. Thus, single photons provided by antenna/NC system can have strong potentials in quantum cryptography. As a result, coupling single quantum emitters (here nanocrystal) to bowtie nanoantennas will produce a new type of emitter with widely adjustable photophysical properties, which can be called a "*tunable superemitter*". Emission characteristics of the antenna/NC system is highly determined by the coupling intra-superemitter.

To My Mother

Contents

Abstract	iii
Abbreviations	ix
1 Introduction	1
1.1 Outline	4
2 Basics	7
2.1 Single Emitters	7
2.1.1 Single Molecules	7
2.1.2 Single Semiconductor Nanocrystals	8
2.2 Metallic Nano-Structures	9
2.2.1 Isolated Particles	10
2.2.2 Coupled Particles	14
2.2.3 Resonant Antennas	17
2.2.4 Materials Aspects	20
2.3 Single Emitter near Metallic Nanostructures	22
3 Confocal Microscopy of Single Emitters	29
3.1 Principle of Confocal Microscope	30
3.2 One Photon Excitation (1PE)	31
3.2.1 Description of the 1PE Confocal Set-up	32
3.2.2 Data Acquisition	37
3.2.3 Principle of TTTR Operation	38
3.2.4 Sample Preparation	39
3.2.5 1PE Confocal Microscopy of Single Emitters	42
3.3 Two Photon Excitation (2PE)	47
3.3.1 Principle of 2PE	47
3.3.2 Description of the 2PE Confocal Set-up	49
3.3.3 2PE Confocal Microscopy of Single Emitters	50
3.4 Nanocrystals <i>vs</i> Single Molecules	51
3.5 Power Dependence of Single Nanocrystals	54
3.5.1 Theory	54

3.5.2	Results	57
4	Antenna Tip Fabrication	61
4.1	Metal Evaporation	62
4.2	Micro-Fabrication of Nano-Antennas	65
4.2.1	Structuring on the Flat Substrate	66
4.2.2	Structuring at the AFM Tip Apex	69
4.2.3	Fabricated Bow-Tie Antennas	70
5	Tip - Quantum Dot Interactions	75
5.1	Tip-Sample Force-Interactions	76
5.2	Fully Coated Tips: Quenching	79
5.3	Antenna Tips: Enhancement	80
5.3.1	One Photon Excitation	82
5.3.2	Two Photon Excitation	86
6	Characteristics of "Antenna/NC" System	95
6.1	Absorption Cross Section	96
6.1.1	Theory	96
6.1.2	Results and Discussions	97
6.2	Emission Polarization	101
6.2.1	Introduction and Theory	101
6.2.2	Results and Discussions	105
6.3	Photon Anti-Bunching	110
6.3.1	Introduction	111
6.3.2	Theory	115
6.3.3	Results and Discussions	117
7	High-Resolution Optical Microscopy	123
7.1	Introduction	123
7.2	Results	128
8	Summary	131
	Bibliography	135
A	Emission Polarization Measurements	149
A.1	Measurements	149
A.2	Data Correction	152
A.3	Data Interpretation	154
B	Photon Anti-bunching Measurements	157
	List of publications	161

List of abbreviations

1PE	One-Photon Excitation
2PE	Two-Photon Excitation
AFM	Atomic Force Microscope
APD	Avalanche Photodiode
a.u.	arbitrary unit
C-QED	Cavity-Quantum Electro Dynamics
cw	Continuous Wave
EP	Emission Polarization
FIB	Focused Ion Beam
HROM	High-Resolution Optical Microscopy
HRTEM	High-Resolution Transmission Electron Microscopy
MBE	Molecular Beam Epitaxy
MD	Modulation Depth
NC	Nano Crystal
NSOM	Near-field Scanning Optical Microscopy
OM	Optical Microscopy
PD	Degree of Polarization
PL	Photoluminescence
qdot	Quantum Dot
SCOM	Scanning Confocal Optical Microscope
SEM	Scanning Electron Microscopy
SNOM	Scanning Near-field Optical Microscope
SP	Surface Plasmon

SPP	Surface Plasmon Polariton
TAC	Time-to-Amplitude Converter
TCSPC	Time-Correlated Single Photon Counting
TEM	Transmission Electron Microscopy
TH	Time-Harp
TTTR	Time-Tagged Time-Resolved

Chapter 1

Introduction

With further development in science and technology there has been a strong tendency to explore nature at the nanometer scale. This trend apparently began with Feynman when he declared "*there's plenty of room at the bottom*" [1]. Although Feynman's original ideas were mainly based on the techniques available at that time, the era of nano-scale research started with the invention of STM [2] and AFM [3]. Many technologies have been introduced based on these techniques for manipulating small objects at nanometric scales (see e.g. [4, 5]). Although AFM and STM provide useful information about topography and electronic structure of the surface, many other questions such as spectroscopic properties and chemical composition remain unanswered which can be investigated using optical methods. The amount of information provided via optics is far more than other techniques. Using optical techniques not only information about the physical size of an object can be obtained but also at the same time spectroscopic characteristics can be studied. The main problem which arises on the way of light to be used for nano research is the "*diffraction limit*". The diffraction limit defines the smallest volume to which light can be focused by a lens. According to Abbe, the

diffraction limit is defined as follows [6]:

$$d_{focus} = 0.61 \frac{\lambda}{NA} \quad (1.1)$$

Here d_{focus} is the diameter of the focus, λ the wavelength of light and NA the numerical aperture of the lens. Assuming a wavelength at the lower limit of visible spectrum, say 400 nm and using a high-numerical aperture objective lens ($NA = 1.45$), the diameter of the focus is in the order of 170 nm. However, length scales of interest for nanoscience and nanotechnology are smaller than 100 nm [7]. This is by far beyond the capability of conventional optical techniques. Invention of scanning near-field optical microscopy extended the potential of optics beyond this limit and opened the path for optics at nanometric scales [8] which started the era of "nano-optics". The goal of "nano-optics" is to address dimensions beyond the diffraction limit and to resolve objects with sizes down to a few nanometers using light [9]. These desired objects can be small metallic nano-structures or single fluorescent species, *etc.* [10]. In addition to resolving single fluorescent emitters, understanding and manipulating their radiation properties is of special interests for nano-optics research. Results of such modified fluorescent properties can be used for many purposes such as quantum information processing [11]. The main reason that single emitters are preferred compared to the ensemble level is the electronic structure of single emitters, consisted of an electronic ground state and electronic excited state, known as "two-level" system. Such a single emitter which represents a well defined nano-optical model system can emit single photons, similar to a single atom [12]. Fig. 1.1a shows schematically structure of a hybrid semiconductor colloidal nanocrystal, known as "*artificial atom*" [13] which has been used in current work. Emission properties of nanocrystals is

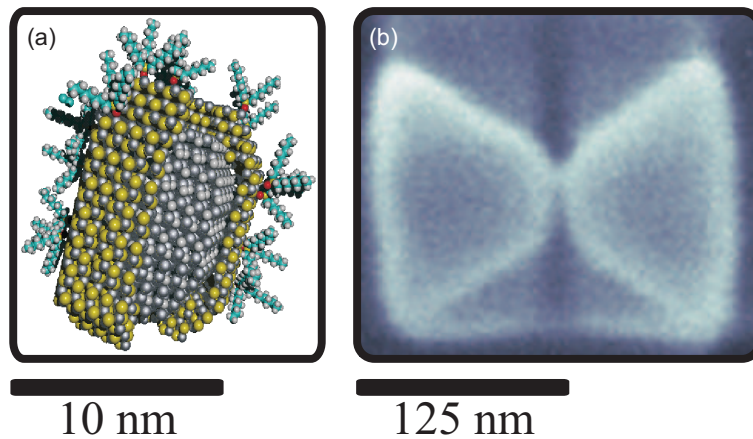


Figure 1.1: (a) Structure of a colloidal semiconductor nanocrystal. (b) SEM image of a bowtie nanoantenna.

explained in section 2.1.2.

In nano-optics, it is of special interest to investigate the change in emission properties of single emitters in contact with a "tip". In such a configuration the *tip* can probe the *near-field* of the *single emitter* and *vice versa*. However, the nano-optics approach based on a metallic [14] or dielectric [15] tips suffers from fluorescence quenching of the single emitter in contact with the tip. Quenching which leads to complete (or partial) depletion of the fluorescence intensity prohibits optical studies on emission characteristics of single emitters with high-resolution and high-sensitivity. Therefore, finding new possible schemes to overcome quenching processes can have strong impacts on optics research at nanometer scales. In this thesis will be shown and documented how a specific type of metallic nanostructure known as "*bowtie nanoantenna*" fabricated at the apex of a tip, can be used to overcome the quenching processes which is done via controlled manipulation of the emission properties of semiconductor nanocrystals (as a single emitter). As a results one single emitter can be sensitively probed with high-resolutions, defined by the antenna structure. Fig. 1.1b shows an SEM

image of such bowtie nanoantenna. It consists of two closely spaced metallic triangles, called the "antenna arms", separated by a very small distance called the antenna "feedgap". Upon laser illumination a bowtie antenna develops a strong dipole along the antenna. Charge oscillations inside each arm give rise to strong electromagnetic (EM) fields inside the feedgap of the antenna. Antenna feedgap, once closely enough spaced with respect to the single emitter can interact with the dipole of the single emitter (Fig. 1.1b). In this picture, bowtie antenna and nanocrystal act as two interacting isolated single dipoles. Coupling of a single emitter to the bowtie nanoantenna upon proper illumination will produce a new type of emitter which can be called a "superemitter" whose radiations properties are mainly inherited from the bowtie antenna rather than the quantum emitter. The superemitter is formed via controlled tailoring of the emission properties of the single quantum emitter in contact with the bowtie antenna, without non-radiative dissipation of the excited-state energy inside the single emitter.

1.1 Outline

In the first chapter, a review of single emitters and their emission characteristics is presented. Section 2.1.1 gives an overview of single molecules. Single semiconductor nanocrystals are reviewed in section 2.1.2. Section 2.2 presents a general overview of different types of metallic nano-structures and their potential to be used for nano-optics research. In particular we will discuss metallic particles (section 2.2.1) and antenna-type structures (section 2.2.2). In chapter 3 the optical setups used for one- and two-photon excitations are described. This is followed by a description of data acquisition and methods used for preparation of single molecule and nanocrystal samples. General issues regarding the imaging of sin-

gle molecules and quantum dots excited by one and two photon excitation are discussed, next. Photoluminescence intensity of quantum dots versus excitation power is illustrated which gives us enough understanding of the saturation behavior of quantum dots based on an average over 90 single nanocrystals. Chapter 4 presents the micro-fabrication of antenna structures and different steps that are necessary for their production. Finally in chapter 5, the interaction of a single emitter system (quantum dots) with antennas is studied. The results are compared with experiments with fully-coated tips to cross-check that the observed effects originate from the antenna structure. Three important effects of the antenna on the quantum system are discussed in chapter 6. This includes, the absorption cross section, the emission polarization and the photon-antibunching. High-resolution optical microscopy using bowtie nanoantennas is presented in chapter 7. The fact that a bowtie antenna does not quench the emission of single emitters, opens the road for a new type of highly sensitive, high resolution optical microscopes based on optical nanoantennas.

Chapter 2

Basics

2.1 Single Emitters

Single quantum emitters can be defined as objects with an electronic ground state and an electronic excited state which react as a single dipole, similar to single atoms. Upon photonic irradiation with enough energy, electrons can be excited from the ground state to the excited state which will be followed by a relaxation of the excited electron. Here two type of single quantum emitters are discussed, single *organic dye* molecules and *semiconductor nanocrystals* (quantum dots).

2.1.1 Single Molecules

In an organic molecule, the lowest energy electronic transitions is between the highest occupied molecular orbital (HOMO) and the lowest unoccupied molecular orbital (LUMO). Excitation of the molecule can be resonant into the vibrational ground state of the LUMO or non-resonant involving higher vibrational modes of the LUMO. Non-resonant excitation is usually followed by internal relaxation to the ground state of the LUMO which is a fast process, on the order of *1ps*

[16]. Radiative relaxation of the excited electron to vibrational levels of HOMO leads to generation of photons, which are red-shifted with respect to the excitation. This process which is known as fluorescence or photoluminescence. In single organic molecules it has an excited state lifetime on the order of 1-10 ns. However, relaxation of the excited electron can also be non-radiative via vibrations or collisions which leads to releasing of phonons [9]. Chapter 2 discusses fluorescence confocal microscopy of two types of molecules: (1) DiI which has a good absorption cross section under one-photon excitation and (2) RhodamineB with good absorption cross section under two-photon excitation.

2.1.2 Single Semiconductor Nanocrystals

Quantum dots are semiconductor structures with physical sizes smaller than the Bohr radius of an exciton. In a bulk semiconductor illuminated by photons with enough energy, an electron is excited from the valence band to the conduction band leaving a positively charged hole behind. However, in a nanometer sized semiconductor the generated electron-hole pair (exciton), is confined to a region that is smaller than the Bohr radius. Therefore, their electronic structure will be dominated by quantum confinement [17]. Generated electron-hole pair sees a "particle-in-a-box" potential in all three dimensions which leads to discrete atom-like energy levels. As a results, quantum dots are often referred to as "*artificial atoms*". Energy of the lowest exciton state in a spherical quantum dot, is [18],

$$E_{exciton} = \frac{\hbar^2\pi^2}{2m_e R^2} + \frac{\hbar^2\pi^2}{2m_h R^2} + E_g \quad (2.1)$$

Where E_g is the intrinsic bandgap energy of the bulk semiconductor material, R is the radius of the quantum dot, $m_{e(h)}$ is the electron (hole) effective mass, and

$\hbar = h/2\pi$ in which h is the Planck's constant. Within this equation the energy of the lowest excited exciton changes as the inverse square of the quantum dot radius. Therefore, by tuning the size of quantum dots their emission wavelength can be tailored [13].

Quantum dots can be prepared in different ways, but colloiddally prepared quantum dots known as nanocrystals have many applications, based on their variable properties [19]. Diameter of nanocrystals can be tuned between ~ 15 to 100 \AA . This can be compared with bulk Bohr exciton diameter of for instance CdSe nanocrystals which is around 112 \AA [17]. Depending on the size of the nanocrystal emission wavelength changes. The sample used in our experiments is CdSe nanocrystals with a hexagonal Wurtzite structure. CdSe forms the core of the nanocrystal with a diameter of around 5 nm , which leads to an emission wavelength centered at 585 nm ¹. CdSe{core} is overcoated with ZnS{shell} which leads to a tremendous increase in quantum yield of the nanocrystal [20]. In chapter 2 fluorescence properties of such nanocrystals have been studied.

2.2 Metallic Nano-Structures

Metallic nanostructures with at least one dimension between 1 to 100 nm have attracted growing attention in the field of nano-optics, due to their fascinating optical properties. This is specifically due to their strong potential to be used as probes for near-field optics [21]. Investigations of such structures have been fueled by current expertise in micro/nanofabrication. In a top-down approach, focused ion beam milling and deposition has provided the way to produce well-defined nanostructures of metal. A bottom-up approach using chemical techniques has

¹QDot Corporation, 585 Streptavidin Conjugate, catalog number 1001-1

allowed preparation of well-controlled nanostructures in very small scales down to a few nanometers [22, 23]. In this section optical properties of two types of metallic nanostructures are described. Section 2.2.1 is about behavior of a single metallic nanoparticle under illumination by electromagnetic (EM) waves. This will be followed by characteristics of two metallic nanoparticles in vicinity of each other forming an "antenna" whose radiation properties in contact with a single quantum emitter, are the main focus of current thesis.

2.2.1 Isolated Particles

Absorption and scattering of light are two major consequences of metallic particles under laser illumination. These two components define the extinction of each particle. Under resonant excitation, collective oscillations of free electrons lead to *surface plasmons (SP)* which have a radiative lifetime of around $10fs$ [24]. Such resonant excitations lead to strong absorption, scattering and local electromagnetic field enhancement. The frequency and intensity of *SPs* depends sharply on the dielectric function of the material as well as the dielectric function of the surrounding environment [24, 25], size [26, 27] and shape [25, 28] of the nanoparticle. Under irradiation, electrons are driven by the electric field and coherently oscillate at the *plasma frequency*, ω_p . For a bulk metal with infinite size the plasma frequency can be written as [29],

$$\omega_p = \sqrt{\frac{Ne^2}{\epsilon_0 m_e}} \quad (2.2)$$

Where N is the number of electrons ϵ_0 is dielectric constant of the vacuum and e and m_e are charge and effective mass of electron. In reality, since an electromagnetic wave impinging on a metal surface has a certain penetration

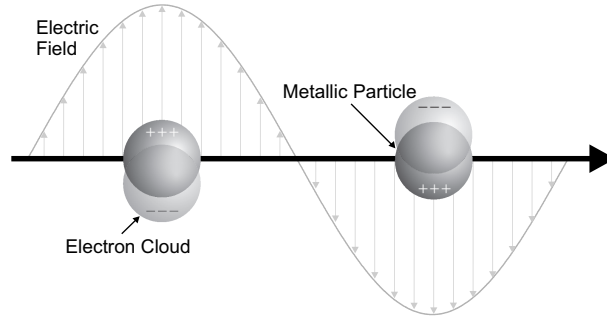


Figure 2.1: Schematic representation of plasmonic oscillations of a metallic sphere showing the conduction electron charge cloud.

depth, just the electrons on the surface are the most significant, whose quantized plasma oscillations are called "*surface plasmon polariton*" (SPP) [30]. For a metal-vacuum interface, applying the boundary conditions results in a surface plasmon mode of $\omega_p/\sqrt{2}$ in frequency. Such *SPs* represent a longitudinal surface charge density which can travel across the surface, a *propagating* SPs (PSPs). Intensity of SPs propagating along the metallic surface gradually decays over the 10-200 micrometers [24]. Propagation length, L_{psp} , can be formulated as,

$$L_{psp} = \frac{1}{2K_{psp}} = \frac{c}{\omega} \left(\frac{\epsilon_m + \epsilon_d}{\epsilon_m \epsilon_d} \right)^{3/2} \frac{\epsilon_m^2}{\epsilon_m} \quad (2.3)$$

In which, K_{psp} is the imaginary part of the complex surface plasmon wavevector. ϵ_m and ϵ_d are the dielectric function of metal and dielectric, respectively with c as the speed of light and ω the light frequency.

In metallic nanostructures (e.g. nanoparticles) since collective excitation of free electrons is confined to a finite volume, *localized* SPs (LSP) are formed. Figure 2.1 show a schematic picture of such LSPs, where conduction electrons of a metallic particle oscillate coherently in response to the electric field of light. For a particle in vacuum resonance frequency equals $\omega_p/\sqrt{3}$ [29].

Mie theory by defining the extinction cross section of a particle (R) much smaller than the wavelength of light (λ) [31] (i.e. $\lambda \gg R$) gives the resonance absorption conditions. For a particle with ε_1 and ε_2 as real and imaginary parts of the dielectric function located in a medium with dielectric constant of ε_m , plasmon absorption appears when $\varepsilon_1 \approx -2\varepsilon_m$. A consequence of such "resonant" light absorption is strong polarization of the particle (Eq. 2.4) as shown in Fig. 2.1. Accumulated charge on the metal-dielectric interface results in a very strong amplification of the EM field on the metal surface. Therefore, polarizability of the particle plays a very important role in enhanced fields on the surface. The higher the polarizability, the higher is the field enhancement. Due to the localized fields, nanoparticles have attracted strong interests for near-field optics research [32, 33, 34]. We can assume an isolated spherical particle much smaller than the wavelength of light with radius, R and dielectric function of $\varepsilon = \varepsilon_1 + i\varepsilon_2$, illuminated by electromagnetic fields develops an internal polarization, P_{in} , oscillating coherently with respect to the driving field, E_0 . The external electromagnetic field collectively created by this internal polarization can be represented by the field of a dipole, \mathbf{p} , located at the sphere center which scales with sphere volume as [35],

$$\mathbf{p} = 4\pi\varepsilon_0\varepsilon_m \left(\frac{\varepsilon - \varepsilon_m}{\varepsilon + 2\varepsilon_m} \right) R^3 E_0 \quad (2.4)$$

With ε_m dielectric constant of the surrounding medium and ε_0 is the permittivity of the vacuum. P_{in} is related to the local internal electric field strength E_{in} as well as the incident field E_0 [35] shown as,

$$P_{in} = \varepsilon_0(\varepsilon - \varepsilon_m)E_{in} = 3\varepsilon_0\varepsilon_m \left(\frac{\varepsilon - \varepsilon_m}{\varepsilon + 2\varepsilon_m} \right) E_0 \quad (2.5)$$

P_{in} and E_{in} are independent of r within isolated spheres. The electromagnetic fields outside the particle is a superposition of the incident field E_0 and dipole field due to \mathbf{p} . Above the particle surface the local field is maximum and given by [35],

$$E_{surf} = \frac{3\varepsilon}{\varepsilon + 2\varepsilon_m} E_0 \quad (2.6)$$

As it was mentioned, at the plasmon resonance where the real part of the dielectric constant of the particle ε_1 approaches -2 , the fields inside and outside of the particle will be very large. Amplitude of these fields depends highly on the imaginary part of the dielectric constant ε_2 . Noble metals such as, *Ag* and *Au* have fairly small ε_2 thus they can develop very strong fields. At a given excitation wavelength the local field intensity near the metal surface is related to the induced dipole, \mathbf{p} [35] which also determines the absorption and Rayleigh scattering cross sections given by,

$$\sigma_{abs} = \frac{8\pi^2 R^3 \sqrt{\varepsilon_m}}{\lambda} \left| \text{Im} \left(\frac{\varepsilon - \varepsilon_m}{\varepsilon + 2\varepsilon_m} \right) \right| = \frac{2\pi}{\lambda \varepsilon_0 \sqrt{\varepsilon_m}} \left| \text{Im} \frac{p}{E_0} \right| \quad (2.7)$$

and

$$\sigma_{sca} = \frac{128\pi^4 R^6 \varepsilon_m^2}{\lambda} \left| \frac{\varepsilon - \varepsilon_m}{\varepsilon + 2\varepsilon_m} \right|^2 = \frac{8\pi^3}{3\lambda^4 \varepsilon_0^2} \frac{p^2}{E_0^2} \quad (2.8)$$

Extinction is the sum of absorption and scattering. For small particles absorption is the dominant process in extinction and as particle size increases, scattering takes over. Various shapes of nanoparticles have been studied theoretically. Results show that at corners with high curvature electromagnetic field enhancement and localization is much more than the spherical particle. This is

sometimes referred to as "lightning rod" effect which is explained in chapter 7. Moreover, theoretical calculations on isolated nanorods show that the resonance wavelength is highly dependent on the rod length [36]. Increasing the rod length redshifts the resonance peak caused by larger dipolar separations. Since nanoparticles concentrate the electromagnetic energy in a sub-wavelength region without significant thermal dissipation, they can act as antennas. Although nanoparticle as non-resonant antennas has been extensively used for surface-enhanced raman spectroscopy (SERS) [35, 37] there exist only few results regarding the interaction of single particle and single emitters as a nano-optics approach [38, 33]. Although isolated metallic particles, upon irradiation develop enhanced EM fields on the surface but they are known to be inefficient antennas for field enhancement purposes. This has been proved by observation of fluorescence quenching near nanoparticles [39, 40] which means the weight of enhanced EM fields on the surface of nanoparticles is not sufficient to overcome the quenching processes [34]. In the next section two adjacent metallic nanoparticles are described. Such a metallic nanostructure a specific length can be act as an efficient resonant antenna with strong potential for field enhancement schemes.

2.2.2 Coupled Particles

In the previous section, resonance behavior of an isolated metallic particle was described in which shape and size as well as the dielectric constants, play the main roles in electronic excitations which lead to EM field enhancement on the surface of the particle. However, electric field existing between two adjacent metallic particles is totally different in properties and amplitude as well as confinement. In the case of two metallic particles close to each other, the gap (defined as the separation between two particles) plays a very important role in the optical response.

This is due to coherent capacitive coupling between particles which dramatically increases the field enhancement and profoundly changes the internal polarization of each particle [35]. Fig. 2.1 showed the polarization of an isolated particle upon EM illumination. Similar to this picture, we assume two metallic particles along the x -axis illuminated by laser light (wavelength λ and intensity I_0) propagating along y -axis and polarized along the x -axis. In resonance conditions, both particles are highly polarized due to the electric field of light, similar to Fig.2.1. In the gap region there are opposite charges accumulated which oscillate harmonically with the electric component of light. Closely spaced opposite charges in the gap area are source of electric field enhancement in the gap, $|E|^2$. Therefore field enhancement inside the gap is highly dependent on the charge density (ρ_q) on both sides of the gap. Intensity of the incident field (I_0) dramatically increases the charge density and therefore field enhancement. Polarization of the particle (p_λ which is a function of the dielectric constant of the particle depending on the incident wavelength influences the field enhancement dramatically. Moreover, separation (d) between opposite charges is a very important factor. The smaller the separation (smaller gap size) the higher is the field enhancement. Overall all these factors can be written as,

$$|E|^2 \propto \rho_q \cdot I_0 \cdot d^{-n} \cdot p_\lambda \quad (2.9)$$

In resonance conditions, where $\varepsilon_1 \approx 2$, $p(\lambda)$ reaches its maximum, which therefore causes a very strong EM field enhancement inside the gap. In equation 2.9, d is the size of the feed gap meaning how closely the opposite charges are spaced with respect to each other. Smaller feedgaps lead to stronger field enhancements inside the gap. Theoretical simulations show that below 100 nm gap size, stron

coupling between two metallic particles occur which leads to significant field enhancement [36]. In this separation regime, near-field of the dipole polarization of one particle induces quadropolar and higher order moments in the close neighbor particle which leads to coherent oscillating higher order multipole moments [41]. Amplitude of these multipole moments is proportional to the excited electronic states of the metal. Due to high polarizability of metals, nature of the metallic excited state changes from volume excitation to a surface excitation as two particle approach [35, 41]. Metal surfaces in the gap produces huge fluxes of electrons which is the origin of enhanced fields in the gap and is highly confined to the gap region. Hence, EM field confinement of two-adjacent particles is dependent on the gap size. In addition to EM fields inside the gap, dipole-dipole interactions in the gap leads to very strong forces which are proportional to the light intensity and d^{-4} [42]. As it can be understood, for two metallic particle close to each other gap plays the dominating role in determining the optical response of special interest "field enhancement" and "field confinement". Theoretical simulations for coupled nanorods show that electric field enhancement and optical resonance frequency is highly dependent on the gap size [36]. In gaps smaller than 100 nm, charge distribution intra- and inter-particle is highly influenced by the size of the gap. When two particles are coupled, opposite charges are strongly localized to the ends of the two metallic particles at the gap. Strong attraction across the gap competes against the intrarod forces that drive the intrarod charges. This can cause redshifting the resonance behavior with decreasing the gap size. In such a picture two-coupled metallic particles can be assumed as an "antenna" whose field enhancement and confinement are far more than an isolated metallic particle. However, antenna behavior is not only determined by polarization of each particle. In antenna with specific length determined by the incident wave length,

EM field enhancement inside the gap is enormous. This leads to radiation of the antenna from the gap. In order to understand the antenna behavior radio-wave antennas can be good examples.

2.2.3 Resonant Antennas

According to *radio-wave technology* standards, antennas can be defined as devices which can radiate EM waves and convert free-space waves to guided waves [43]. The very first question that should be answered is how does an antenna radiate? A simple example is an open ended conducting wire attached to a AC electric source which drives the free electron inside the metal [44]. Acceleration of charges at the source-end of the wire and their deceleration on the reflection from the other end, produces radiated field at both ends and the remaining part of the antenna. Therefore, charge acceleration due to induced fields and deceleration due to impedance discontinuities are responsible for electromagnetic radiation. With this picture the way an antenna receives electromagnetic waves can be simply understood. Upon illumination, electromagnetic waves drive the charges inside the metal whose motions, i.e. acceleration-deceleration, leads to an electric field in the center of the antenna or in other words in the "gap". The total length of the antenna is an important factor for resonance behavior of an antenna with respect to the incident fields. This is because, standing waves current caused by the electromagnetic radiation travels a distance of $\lambda/2$ inside the metal in one-half of a period [44]. Therefore, "charge build-up" at the gap reaches its maximum when the total length of the antenna equals $\lambda/2$, known as the *resonance* condition. An antenna with this characteristic length scale is a resonant antenna, which contain enormous EM fields inside the gap and is capable of radiating EM waves. In determining the resonant length of the antenna refractive index of the

environment is an important factor. In this case average of the refractive indices of the surrounding environments of the antenna (n_{av}) is taken into account. Therefore, total length of a resonant antenna equals $L_T = \lambda/(2n_{av})$. However, if the incident light is at optical frequencies, total length of the resonant antenna can not exceed from a 100-200 nm. Moreover, gap size in such an antenna will be on the order of a few tens of nanometer. As a result, an antenna which is resonant on optical frequencies can be called a *resonant nanoantenna*. Localized electric field which is confined in the gap is of special interest for nano-optics purposes. The main question is whether a resonant nanoantenna can be also realized in the nanometer scales [45] or in other words, whether light at optical frequencies can be used to drive charges in an antenna? Experimental observations on resonant optical nanoantennas in accordance with theoretical calculations show that for a dipole antenna with total length of $L_T = 255nm$, resonance appears at 830 nm laser wavelength [46]. In *resonant* coupling between the excitation light and antenna, highly non-linear processes inside the antenna gives rise to a super-continuum white light radiated from the gap. Absence of the gap and slight de-tuning from resonance length, changes the behavior drastically. These results prove the possibility of creating highly localized electromagnetic fields inside the gap of a *resonant optical antenna* illuminated in IR. According to these results antenna-length already deviates from the radio-wave antenna principles which would predict a total length of 330 nm for $\lambda = 830nm$ ($n_{av} = 1.25$).

The aim of the current thesis is to study the response of a bowtie nanoantenna in the VIS/IR spectrum as probed by a single quantum emitter. Figure 2.2 describes all the processes involved in a bowtie nanoantenna under laser illumination. Incident electromagnetic waves induce charge accumulations on each arm of the antenna oscillating harmonically with electric field of light. For optimum

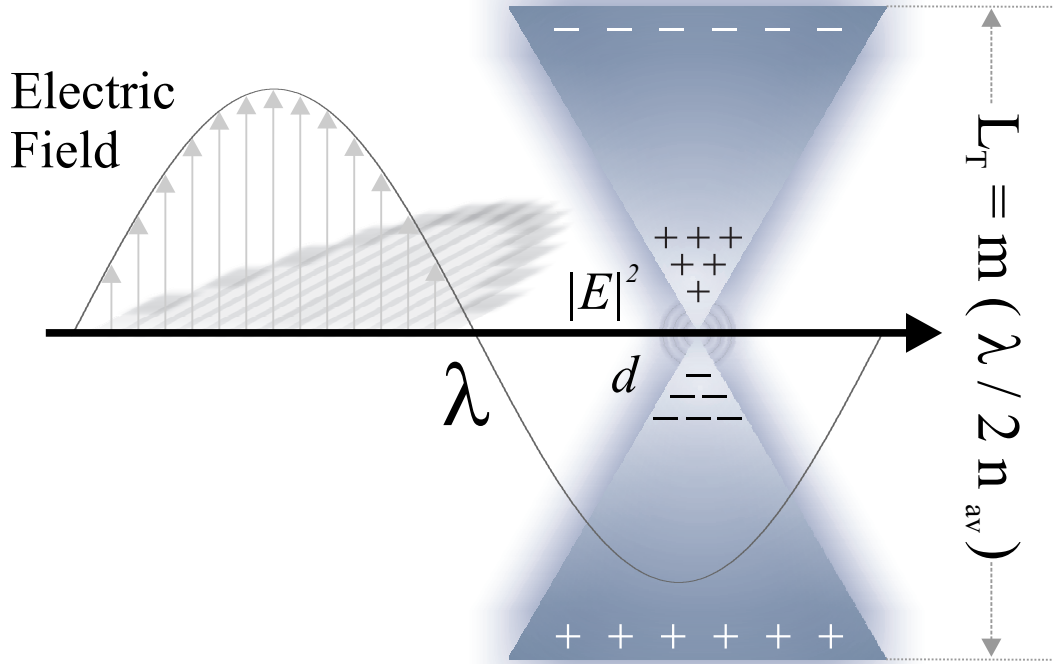


Figure 2.2: Schematic representation of a bow-tie antenna under illumination with laser light which induces opposite charges in the gap between the two triangles. λ is the wavelength of the incident light. Opposite charges in the gap lead to field enhancement of $|E|^2$. L_T is the total length of the antenna depending on the average refractive index of environment, n_{av} and d the size of feed gap. In this equation m is introduced as the correction factor for optical frequencies as compared with radio-wave antennas.

coupling and charge build-up on each arm resonant length should be taken into account which in Fig. 2.2 is shown by $L_T = m(\lambda/2n_{av})$. Here m is introduced as correction factor according to deviation from radio-wave antennas. According to dipole antennas irradiated in IR $m = 0.77$ [46], taking into account a glass substrate with refractive index of 1.5 and air with refractive index of 1.

Bowtie nanoantennas have attracted much attention in the scope of nano-optics [47, 48, 49, 50]. Triangular shape of each arm with their sharp corner inside the gap is apparently the main reason. The sharp corner of each arm

leads to strong charge concentration at the edge of each triangle inside the gap. Moreover, localization of fields inside the gap is more likely to increase while two sharp edges with opposite charges are closely spaced. Finite difference time domain (FDTD) calculations show that angle of the corner of each triangle is very important in antenna response [51] studied in the mid-infrared ($\lambda = 10\mu$). Smaller angles create higher charge density in corner of the triangles and therefore higher field enhancement. Experimental observations on bowtie antennas show that the resonance peak is dramatically influenced by the gap size [49]. This gap-dependence of the resonance peak is significant when the light is polarized along the long axis of the bowtie [47]. *For bowties with 88 nm length of each arm and gap width of around 50 nm resonant wavelength of $\sim 710\text{nm}$ and for gap width of around 20 nm resonant wavelength of $\sim 840\text{nm}$ with ITO/SiO₂ substrate have been measured* [49]. By detecting the two-photon excited photoluminescence of gold resulting from a transition between the d valence band and sp conduction band, electromagnetic field enhancement of bowtie antennas have been studied [48]. Illumination of a bowtie antenna with 75 nm each arm and 20 nm gap size gives rise to a field enhancement of greater than 10^3 . Although this effect is highly polarization dependent, confinement is in the order of 650 nm^2 which is fairly bigger than the gap existing in the nanostructure.

2.2.4 Materials Aspects

Optical properties of metal in the visible range is different from the radio-wave spectrum. In the visible (VIS) and IR wavelengths imaginary part of the dielectric function increases. Real (ϵ_1) and imaginary (ϵ_2) parts of the dielectric constant of metals in near-infrared (NIR) are defined according to Drude free-electron theory [52].

$$\varepsilon_1 = 1 - \frac{\lambda^2}{\lambda_p^2} \quad (2.10)$$

And

$$\varepsilon_2 = \frac{\lambda^3}{\lambda_p^2} \cdot \tau' \quad (2.11)$$

Where $\omega \gg 1/\tau$, where ω is the frequency of light and τ is the relaxation time. In which $\lambda_p^{-2} = Ne^2/\pi m_0 c^2$ and $\tau' = 2\pi c\tau$. Where, N is density of conduction electrons, m_0 is their effective optical mass, e is the charge of an electron and c is the speed of light.

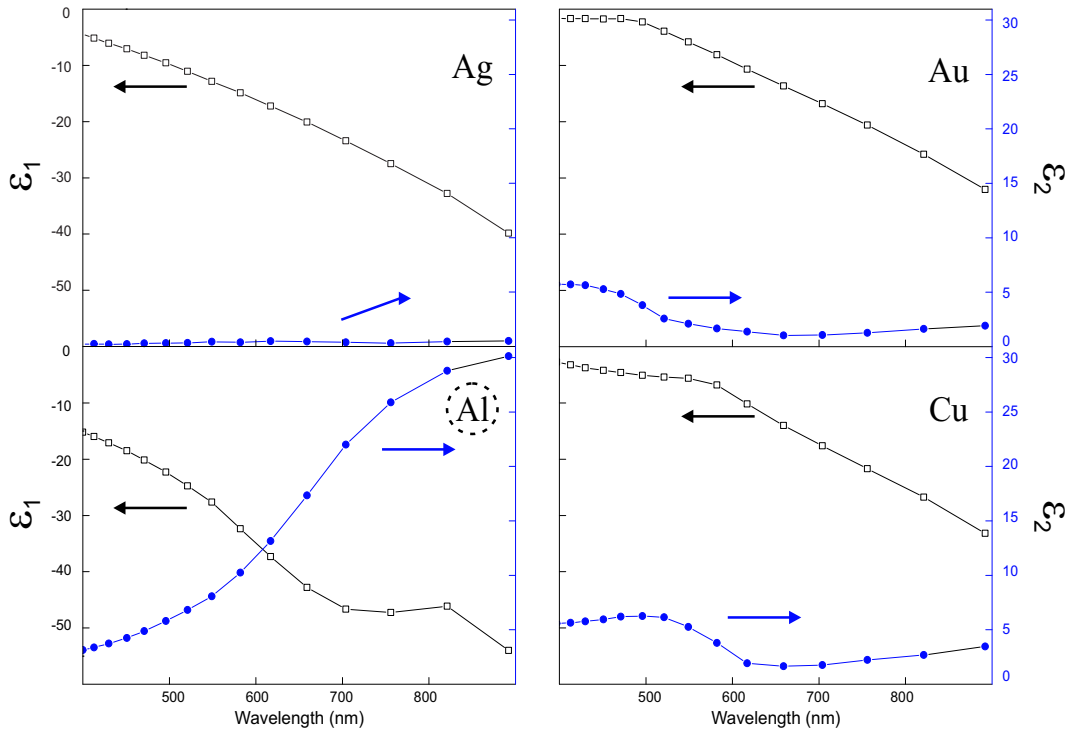


Figure 2.3: Dielectric properties of silver, gold, aluminum and copper in the VIS/NIR region (400-900 nm). Black hollow rectangles are real part of the dielectric function, ε_1 , and blue solid circles are the imaginary part, ε_2 . Data for silver, gold and copper was taken from reference [52] and for aluminum from website: <http://www.luxpop.com>.

Imaginary part of the dielectric constant which determines the ohmic losses inside the metal should be as low as possible. Three metals are known to have low ohmic losses, silver, gold and aluminum whose dielectric properties in VIS/NIR are shown in Fig. 2.3. Silver with its strong tendency for reaction with sulfur in ambient environments is not a good candidate for an antenna. Especially, a nanometric antenna which has a thickness of less than 50 nm. such a thin layer of metal can easily be degraded in the air. The other options for proper material selection are gold and aluminum. At 532 nm (Fig. 2.3), imaginary part of aluminum is slightly higher than the counterpart for gold. This difference is more enhanced when the incident wavelength increases to 830 nm. At this wavelength aluminum is the lossiest metal amongst all. However, due to restriction of microfabrication technique (FIB milling) aluminum was selected compared to gold. Under ion beam bombardment gold melts and the final metallic structure can not be neatly designed. Several experiments with focused ion beam showed that aluminum is the best candidate as material to be used for antenna fabrication.

2.3 Single Emitter near Metallic Nanostructures

A metallic or dielectric *tip* is one the main tools in nano-optics research. Interactions of a *tip* with a single quantum emitter have been investigated in different configurations [14, 15, 53]. One of the main motivations for these efforts, is confinement of the *effects* at the apex of the tip. This for instance can be used to develop highly sensitive optical microscopes with high resolutions (chapter 6). Since the *tip* in nano-optics can go into the near-field of a single emitter alterations of the emission and absorption properties can be studied in-detail. This interaction can be used for instance in increasing the efficiency of single photon

sources (chapter 5). However, proximity of a quantum emitter to a metal structure results in energy transfer to density fluctuations of the free electron gas. The associated currents generate radiation fields outside and Ohmic losses inside the metal. Depending on the relative weight of the two effects, the radiation intensity of the coupled system is enhanced or decreased. Both radiation and Ohmic losses depend on the shape, size and the material of the metallic nanostructure as well as its spatial distance with respect to the quantum emitter. Therefore, all these factors should be taken into account in designing suitable structures to increase the radiation efficiency of single emitters. In radio-wave technology, such optimized structures are known as "antennas" which can be a good starting point for optical field enhancement schemes [45]. A single quantum emitter positioned inside the *subwavelength* size *feedgap* of such an antenna couples to the antenna arms. Optimized design of optical antennas might differ from radio-wave antenna. This is because, optical properties of metals in radio-wave regime are different than that at optical frequencies. At optical frequencies potential for resonant plasmon excitation and damping due to Ohmic losses, increase.

In order to understand the processes which take place between the tip and a single quantum emitter, we consider a perturbed fluorophore system in close proximity with a tip. Approaching a metallic tip to a dipolar emitter perturbs the fluorescence either by quenching or enhancement [54]. Quenching is related to non-radiative energy transfer from the excited quantum emitter to the metallic surface [55] which is dissipated thermally or by coupling to propagating surface plasmons which decay over a certain distance. This effect has been observed in case of metallic [14] tips close to a single molecule. However, dielectric tips [15] close to single molecules cause similar effects, i.e. quenching. But in case of dielectric tips quenching the fluorescence is known to be due to conversion

of evanescent field components to propagating field components at supercritical angles in the upper half space.

A classical dipole \mathbf{p} , excited by the local electric field, E_{local} is written as [56],

$$\frac{d^2\mathbf{p}}{dt^2} + \omega^2\mathbf{p} + k\frac{d\mathbf{p}}{dt} = \frac{e^2}{m_e}\bar{\mathbf{f}} \cdot E_{local}(t) \quad (2.12)$$

Where ω and k are the angular frequency and total decay rate of the transition, $\bar{\mathbf{f}}$ denotes the oscillator strength. In a perturbed system, the total dissipated power is the sum of the intrinsically (P_i) and electromagnetically (P_{em}) dissipated power. According to Poynting's theorem the latter is related to the local fields,

$$P_{em} = P_{em}^0 + (\omega/2)Im\{\mathbf{p}^* \cdot E_{local}\} \quad (2.13)$$

Here, "0" refers to unperturbed situation, such as in free space. The total radiated power in the free space is $P_{em}^0 = |\mathbf{p}|^2\omega k^3/(12\pi\epsilon_0\epsilon)$ and is independent of the environment. For a dipole in an inhomogeneous environment the total field is the contribution of unperturbed field (E_0) and scattered field (E_s),

$$E_{total} = E_0 + E_s \quad (2.14)$$

Therefore, normalized decay rate and radiated power becomes,

$$\frac{k}{k_0} = \frac{P}{P_0} = 1 + \frac{6\pi\eta\epsilon_0\epsilon}{\gamma^3|\mathbf{p}|^2}Im\{\mathbf{p}^* \cdot E_s\} \quad (2.15)$$

η is quantum yield of the free system, ϵ and γ are dielectric constant and wave number of the medium. Equation 2.15 shows the change in radiated power and decay rate of a dipole in an inhomogeneous environment. Quenching is referred to when quantum efficiency defined as ratio of radiative rates to the total decay

rates decreases or $\eta \rightarrow 0$. This is usually referred to as increasing the non-radiative rates which therefore shortens the lifetime. In quenching shortening of the lifetime is associated with a reduction of the emission intensity. Theoretical considerations based on a dipolar emitter near an interface [55, 57] show that this effect is highly dependent on the orientation of the dipole with respect to the interface.

In contrary to quenching, enhancement is described as when quantum efficiency of the perturbed system stays the same or is even more than the unperturbed system. This is usually explained by increasing the radiative rates via coupling of the dipole emitter to a macroscopic dipole referred to "enhanced emission" [58]. Another possibility is enlarging the absorption cross section which is sometimes referred to as "enhanced excitation". Absorption rate, Ω of such a single emitter in the free emitting state is a product of absorption cross section, σ and the local electric field of the laser, $|E_L|^2$,

$$\Omega = \sigma |E_L|^2 \quad (2.16)$$

Local electromagnetic field enhancement caused by an external dipole, increases the strength of *local excitation fields*. This is denoted by α which results in enhanced absorption (or enhanced excitation) rate, thus $|E_L|^2$ is replaced by $|\alpha|^2 |E_L|^2$. The second effect of the enhancement is reflected in the emission process, which causes an increase in the radiative rates (k_r). Emission enhancement factor, α' is introduced for the enhanced emission. Therefore, k_r is replaced by $|\alpha'|^2 k_r$. k'_2 is introduced as the decay rate of the system in the presence of the probe. This is because, the decay rate in the presence of the probe might have some contribution from non-radiative rates opened by the tip. Ratio of the *non-*

resonant fluorescence rate in the presence of the tip to the fluorescence rate of the free emitter, or in other words enhancement ratio, α_T can be written as [59],

$$\alpha_T = |\alpha|^2 \cdot |\alpha'|^2 \cdot \frac{k_{21}}{k_{21} + k'_{21}} \quad (2.17)$$

Here due to considering a non-resonant fluorescence, decay rates of the resonant emission is neglected. Equation 2.17 shows that the total enhancement is a product of enhanced excitation, $|\alpha|^2$ and enhanced emission $|\alpha'|^2$. Enhanced excitation is done via increasing the absorption cross section of the system, in this case no significant change in the lifetime is expected. On the other hand, for a system excited close to the saturation level, increasing the radiative rates of the photoluminescence in contact with the probe leads to enhanced emission. This is usually observed by a reduction in the lifetime in addition to increased emission intensity. It should be mentioned that the increase in the PL intensity associated with the a reduction in lifetime happens only when the excitation intensity is close to saturation. Far from saturation the reduction in lifetime does not necessarily lead to an increase in the emission intensity.

As a result, single quantum emitter sees different channels in contact with the tip. Proximity with the tip can lead to quenching of the fluorescence or enhancement. If the localized electric field of the probe, increases the absorption cross section and/or increases the radiative rates, fluorescence is enhanced. Otherwise, non-radiative decays associated with the tip will lead to quenching of the fluorescence. Enhancement via enhanced excitation or enhanced emission is confined to the localized electric fields. Moreover, in case of enhanced emission, radiation properties of the single emitter are modified. Quenching which is also localized to the probe dimensions, leads to complete (or partial) depletion of the

emission. In the scope of current thesis, localized electric field at the feedgap of bowtie nanoantennas are exploited to for the purpose of "field enhancement". In comparison fully-coated tip quenches the fluorescence which confirms that the observed enhancement is originated from the antenna structure at the apex of the tip.

Chapter 3

Confocal Microscopy of Single Emitters

In this work, single emitters are used to probe the EM fields in the feedgap of bowtie nanoantennas. Using the two intrinsic signatures of the single emitters, PL intensity and lifetime, we can obtain enough knowledge about the interaction between the single emitter and the antenna. However, these characteristics of the single chromophore system should be studied in advance. In this chapter fluorescence of several type of single emitters are studied using confocal microscopy.

3.1 Principle of Confocal Microscope

Contrast mechanism in optical microscopy is caused by either scattered or absorbed light by the species on the sample. However, in simultaneous measurement of several points in the sample, each point in the image can be clouded by light originated from other points in the sample. Confocal configuration was introduced by Marvin Minski [60] to remove this background light. There are several optical configurations that are known as confocal microscope but they are all based on one fact, that is, light originated from non-focal area in the sample plane can not pass through a detection pinhole. Although the confocal detection scheme does not improve the resolution considerably, it leads to strong background suppression. Fig. 3.1 shows schematically principle of confocal microscope that has been used in our experiments. Details of the setup including all the optical components are described in section 3.2.1.

In Fig. 3.1 only the objects located in focal point on the sample will be imaged by the detector. Light originated from other point on the sample is blocked by the detection pinhole. Since fluorescent objects on the sample are randomly dispersed this is a very important aspect for a confocal setup used for fluorescence microscopy. In this section a home-made confocal setup which has been used for experiments is described. Confocal optical measurements performed on the single emitter level provide very important information about the characteristics of the single chromophore system which will be used in contact with the bowtie nanoantenna. Different types of single emitters excited by one- or two-photon absorption will be studied. With such studies using confocal microscopy, fluorescence properties of the free chromophore system can be understood.

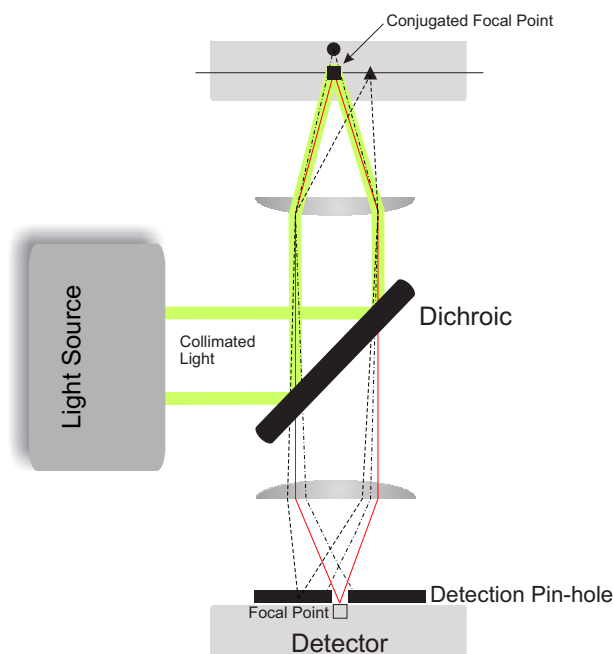


Figure 3.1: Principle of confocal microscopy. Excitation and detection path for a scanning confocal microscope and 3 objects in the sample are shown. As can be seen after excitation by laser light, only the rectangular object which is in the *focal* point on the sample is detected by the detector. Light originated from other points of the sample is blocked by the detection pinhole.

3.2 One Photon Excitation (1PE)

In one-photon excitation photons with enough energy excite the electron of a chromophore from the ground state to the excited state. In two-photon excitation, simultaneous absorption of two photons with half the required energy (twice the wavelength) leads to electronic excitation. Radiative relaxation or fluorescence emission which is a characteristic of the chromophore system stays the same in wavelength and polarization. Both excitation schemes including the respective optical setups are explained in the following.

3.2.1 Description of the 1PE Confocal Set-up

Figure 3.2 shows schematically different parts of the confocal set-up used for one photon excitation experiments. It is a sample scanning confocal optical microscope (SCOM) based on an inverted microscope (Zeiss Axiovert 135).

The laser source is a pulsed laser system (Time Bandwidth Products, GE-100). Pulsed laser source is with repetition rate of 80 MHz and pulse duration of 10 ps, and is frequency doubled to $\lambda = 532$ nm. Repetition rate of 80 MHz gives a temporal pulse spacing of 12.5 ns. For lifetime measurements of CdSe quantum dots whose lifetime varies up to around 40 ns and is centered around 20 ns, repetition rate of the laser should be reduced which is done by a pulse picker.

The pulse Picker is an electro-optic crystal modulator made of Potassium Dideuterium Phosphate (Conoptics Inc., M350-160). The crystal is placed in front of the laser and is driven through the control electronics (Conoptics Inc., M25D), by which the repetition rate of the laser can be tuned from 40 MHz down to a single shot. The control electronics receive a trigger signal from laser cavity corresponding to one laser pulse and gives a signal to the crystal modulator. Out of each 15 laser pulses one passes through, and the other pulses are separated based on the polarization response of the crystal. Therefore, the crystal introduces very strongly polarized laser pulses whose repetition rate is set to 5 MHz (200 ns between successive laser pulses). Positioning of the crystal modulator dramatically influences the pulse picking quality. Slight mis-adjustments can lead to bad pulse picking which will immediately appear as spikes in lifetime measurements. For precise crystal alignments, first the laser was aligned in a straight line without any deviation in vertical and horizontal directions in a distance of about one meter. In the next step crystal modulator was integrated in the path. This was done confirming that laser enters the center of the crystal and exits from the center.

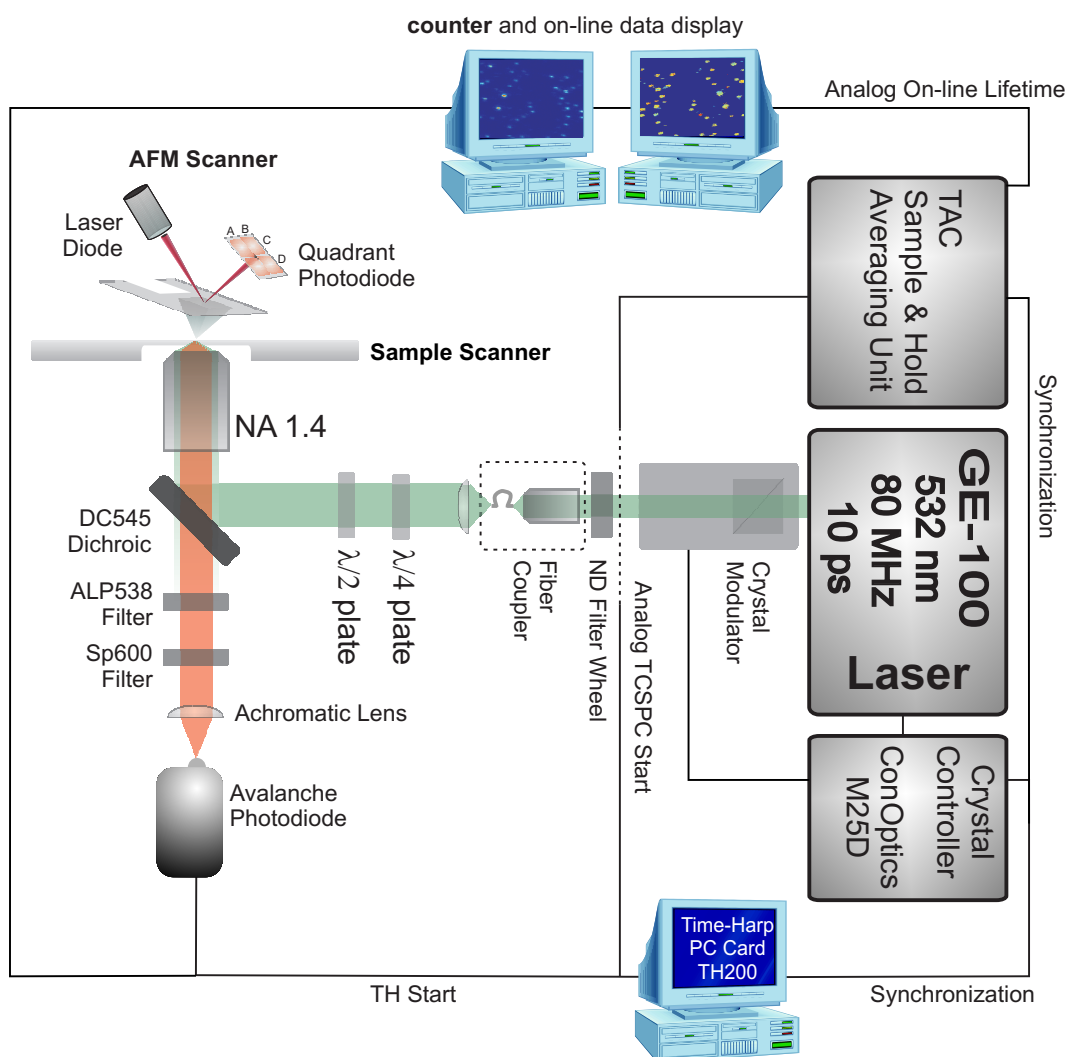


Figure 3.2: Schematic representation of one-photon excitation confocal set-up. Light of 532 nm is released from the laser cavity. Pulse lasers is pulse-picked to 5MHz, by the crystal modulator, driven by MD25D electronics. Pulse picked light is then coupled to an optical fiber. Waveplates control the excitation polarization. Dichroic (DC545) reflects the light to the back-aperture of the objective lens which also collects the fluorescence. Cut-off filters ALP538 and SP600 are used to block the excitation light and AFM laser with optical densities better than 6. An achromatic lens focuses the light to the active area of the APD. Sample scanner and AFM scanner, scan the sample or the tip around the focal area.

This position is not necessarily optimal with respect to optimum pulse suppression. Further improvement of the crystal position was done using a photodiode. The photodiode detects the laser at the exit of the crystal and its output signal is displayed using an oscilloscope. Turning the crystal tube in axial direction positions the polarization axis of the crystal with respect to laser polarization. For a horizontally polarized laser source (known as crossed operation¹), the best pulse picking is observed in exactly 90° angular difference between the polarization axis of the crystal and laser polarization. Further improvement in pulse picking is done by aligning the crystal in two other directions, pitch and yaw. Yaw corresponds to the horizontal angle along the laser propagation and pitch corresponds to the vertical angle along the laser propagation. Final adjustments are done using the instrument response in lifetime measurements. With this procedure pulse-picking qualities better than specifications given by the company (250:1) have been achieved, more than 300:1. One major drawback of the pulse picker is the prolongation of laser pulses after crystal by a factor 2-3.

Pulse-picked laser light after passing through a neutral density filter wheel for intensity adjustments is coupled to a single mode optical fiber for spatial filtering. Coupling efficiency plays a very important role for the light after the pulse picker, because intensity of the laser light is reduced by almost 93%. Light coming out of the fiber is collimated by an achromatic lens and is sent to the back aperture of the objective lens by a dichroic mirror (545DC, Omega Optical), Fig. 3.3. Dichroic mirror reflects the light below 545 nm (at 50%) and transmits the longer wavelengths. On the way towards the dichroic a set of half- and quarter waveplates are used for controlling the excitation polarization.

The objective lens (Zeiss, Plan-Apochromat, ×63, 1.4 numerical aperture, ∞)

¹ConOptics Inc., Modulator Manual

focuses the light on the sample plane to a diffraction limited spot. The same objective is also used to collect the light from the sample plane (Epi-configuration). Back aperture of the objective lens is defined around 8 mm. Assuming $n_{glass}=1.503$, illumination (and collection) angle of the objective is 70° .

The light collected by the objective and transmitted through the dichroic after passing through a cut-off filter (ALP538, Omega Optical) is focused on the $200\ \mu\text{m}$ active area of the single photon counting avalanche photodiode (SPAD) (SPCM-ARQ 13, Perkin-Elmer) which serves as the confocal pinhole. The cut-off filter (ALP538) removes the laser light transmitted through the dichroic with optical density better than 6. With slightly tilting this filter laser light can be seen with the APD in a controlled way. This is for instance used for fine aligning the crystal modulator of the pulse picker. For experiments with the tip in contact an additional cut-off filter (SP600, Chroma Filters) was added to the detection path which blocked the AFM laser completely with an optical density better than 6, shown in Fig. 3.3. This filter (SP600) blocks the wavelengths above 600 nm ($OD \gg 6$), below 600 nm increases to around 80% in a range 2-3 nm. This was specially designed to collect the fluorescence as efficient as possible. *Collection efficiency* of the optical setup for tip experiments in one-photon excitation was determined to be $\sim 2.2\%$ of the nanocrystal spectrum at the ensemble level. This was done by taking into account all the optical components in the path, as well as the quantum efficiency of the avalanche photodiode.

Sample scanning can be done by a Physik Instrument (PI) scanner. The PI scanner is either driven by microscope (Veeco, Bioscope) or Time-Harp (TH) computer card (Time-Harp 200, PicoQuant, Berlin). Microscope scanner gives two signals (triggers) for scanning which can be used for image reconstruction. Frame trigger which shows the beginning of an image and the end. And line trigger

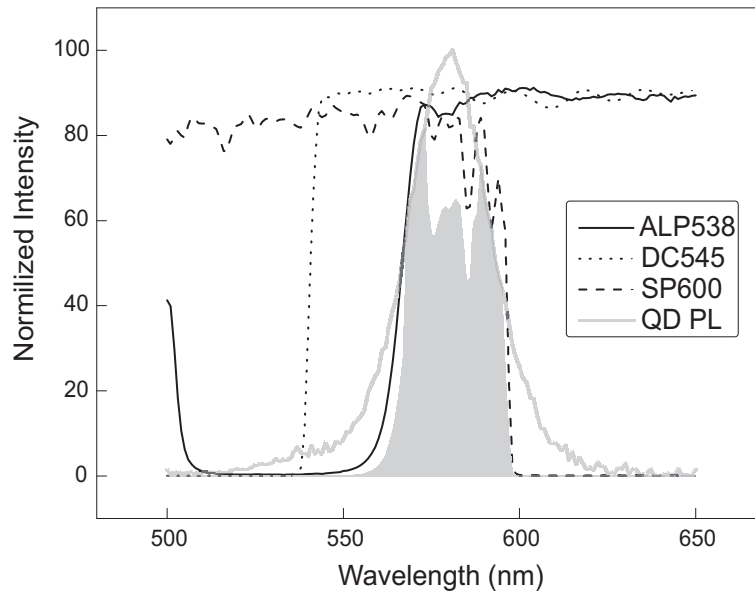


Figure 3.3: Transmission spectra of all filters in the detection path of the one-photon excitation setup used for confocal imaging and tip experiments. Gray line is the emission spectrum of QDot sample at the ensemble level. The shaded area is the portion of the photoluminescence which is detected by APD.

which shows the beginning and the end of each scan line. Time-harp scanner (SCX 200) scans the sample and acquires data with time-tagged time-resolved (TTTR) in scanning mode. The basics of the TTTR measurements are explained in section 3.2.3. Moreover, AFM scanner is combined with the optical setup for studies on tip sample interactions (chapter 5). In this case tip is scanned arounds the focal area by the AFM scanner. As it was mentioned SP600 is used to block the AFM laser completely. In this case frame and line triggers of the scanner is used for image reconstruction of the PL intensity and lifetime as a function of the tip position.

3.2.2 Data Acquisition

For on-line intensity display output of the APD is directly counted by microscope counter (Veeco, Bioscope) which is also scanning the sample. For each forward line, sample is scanned and on the backward the data is displayed. On-line lifetime display is acquired by a home-built device based on time-correlated single-photon counting (TCSPC) technique. In TCSPC, APD provides the "start" pulse upon detecting a photon. The corresponding laser pulse which has caused the photon generation gives the "stop" pulse. Time interval between the start and stop pulse is the "arrival time" of the photon. By histogramming the arrival times lifetime of the system is determined [61]. This type of lifetime measurements [62] is based on three separate electrical units. Time interval between start and stop pulses is converted to a voltage pulse using time-to-amplitude converter (TAC). The voltage amplitude of the pulse varies based on the distance between the two pulses, *in time*. A sample and hold unit samples the TAC voltage and holds the voltage level until another voltage is sampled (i.e. another event). In final step, an averaging unit averages the arrival time of a few events and determines the lifetime. For precise lifetime measurements arrival time of at least 100 photons should be averaged. Averaged voltage is inversly proportional to the lifetime data. The averaged value is displayed as the lifetime of each pixel in the scan image as a voltage read-in and displayed by the Bioscope. Although this technique can be used for on-line display a better quantitative measurement of the photoluminescence lifetimes should be done by digital electronics which is a very powerful data acquisition technique. Digital lifetime measurement is done by time-Harp PC card (Time-Harp 200, PicoQuant, Berlin). The time-harp in oscilloscope mode can show lifetime decays with onboard histogramming but for imaging purposes TTTR mode is used which is a flexible way of data acquisition.

In the next section principles of this mode of data acquisition is described.

3.2.3 Principle of TTTR Operation

In TTTR mode there is no histogramming, instead arrival time of each event together with a time tag from an independent digital clock are sampled. Figure 3.4 is a schematic representation of this operation. As can be seen measurements starts with a marker shown as "marker7" in the data stream. This marker which originates from the time-harp card is generated with the *start* button of the measurement. For each photon event arrival time of the photon with respect to the corresponding laser pulse and with respect to the starting point (i.e. marker7) is saved in the file.

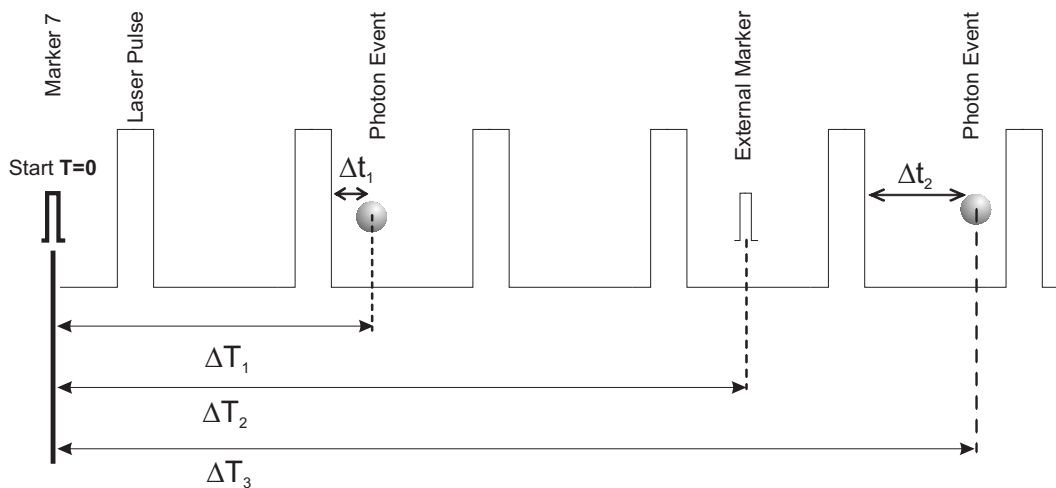


Figure 3.4: Principle of TTTR operation.

With feeding external markers one can have full control on the stream of photons and evaluate intensity of photons as well as lifetime with respect to an *external* event. In our case *frame* and *line* triggers of the sample scanner were used to reconstruct the intensity and lifetime images. In addition by feeding the frame and line triggers of AFM tip scanner, intensity and lifetime data of a single

fluorophore were reconstructed as a function of the tip position, whose results are shown in chapter 4. In order to obtain a lifetime image, arrival time of photons with respect to the exciting laser pulse (t) were histogrammed for each pixel. Exponential fit to the histogram defined as,

$$F = A \cdot \exp\left(\frac{-t}{\tau}\right) \quad (3.1)$$

gives the lifetime for each pixel (τ). For precise determination of the lifetime, histogramming and fitting are done for pixels with at least 100 photons. In pixels which have less amount of photons no lifetime value is displayed in the lifetime image, which means there is no lifetime data available. This is shown as *deep-blue* in confocal images and *white* in tip-scan images. However, this threshold for some experiments with lower signal was reduced to 50 photons per pixel. Intensity images were obtained by counting the number of photon events falling into each pixel of the image.

3.2.4 Sample Preparation

Preparation of single chromophore samples is an important step for each experiment reported here. The first step, which is very critical, is the cleaning of the microscope cover-slips. As-purchased glass slides were first cleaned with lens cleaning tissues for removing dusts and large particles, in a way that after cleaning no contamination on the glass can be seen by "eyes". This was followed by baking the glasses at $550^{\circ}C$ for 600 minutes. After baking, a few of the glass slides were tested by the optical setup which under relatively high laser powers (under 1PE, $\sim 3\mu W$) showed no fluorescence. Monthly optical inspection of the glass slides were performed to keep track on environmental changes.

For single DiI molecules highly diluted dispersion of DiI molecules in toluene were *spin coated* on the cleaned glass substrate. Polymethylmethacrylate (PMMA) was added to the solution for fixation of single molecules on the surface. For this purpose, dilution of DiI in toluene was mixed with one volume percent of 1%wt PMMA in toluene which results in a film thickness of less than 20 nm. Spin coating of $\sim 100\mu\text{lit}$ of the solution was done with the speed of 20,000 rpm for all the samples. Samples of Rhodamine B molecules for two photon excitation were prepared by the same procedure as DiI.

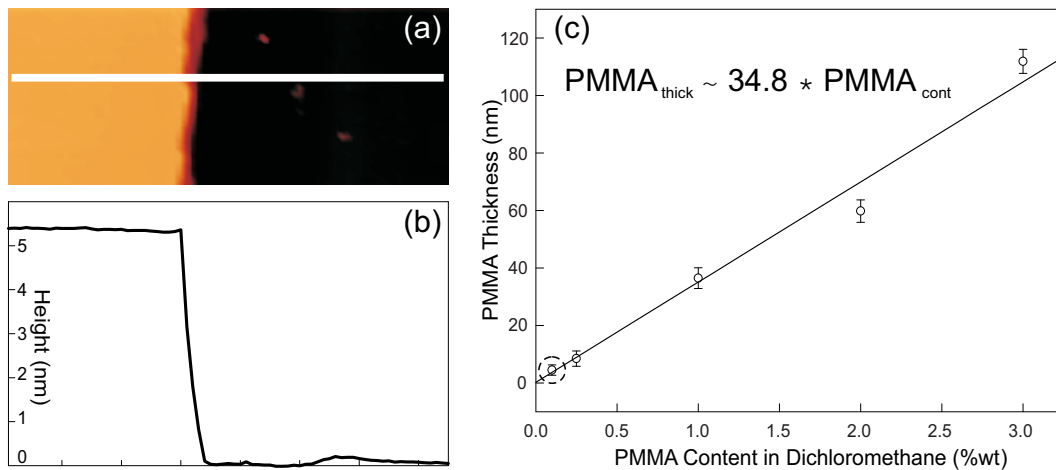


Figure 3.5: (a) contact-mode AFM topography image of a scratch caused by a sharp needle. Sample is 0.1% PMMA in Dichloromethane which is circled in (c). (b) Line profile through the entire image shown in (a) which shows a step of 5 nm. (c) Thickness measurements of PMMA film prepared by spin coating solution of PMMA in Dichloromethane as a function of the PMMA content. Data points are thicknesses averaged over 5 scratches whose standard deviation gives the error bars.

Samples of semiconductor nanocrystals purchased from Quantum Dot Corporation (Qdot 585 Streptavidin Conjugate) were prepared differently. First nanocrystals were diluted by the buffer solution provided by the company (QDot Corp.) down to 2 nM which leads to almost one nanocrystal per squared micron in the confocal image, found empirically. Since diluted dispersion of nanocrystals

degrades over time, it was prepared in small amounts. Diluted nanocrystal solution was spin coated on the glass substrate. In the *next* step the whole surface was covered by spin coated PMMA. Using the polymer layer in quantum dot samples has different purposes. Fixation of nanocrystals by the PMMA film in confocal imaging is one of the reasons for having this polymer layer on the top of nanocrystal sample. In experiments with tip in contact, there is a high probability that nanocrystals are picked up by the tip. Therefore, polymer layer protect the nanocrystals and prevents pickup by the tip. An important property of the polymer film is the thickness of the film which should be as small as possible. In tip experiments while a nanocrystal is sensing the electric field of the antenna, the separation between nanocrystal and the antenna should be as low as possible. This is controlled by the amount of PMMA in the solvent. To study the film thickness, PMMA was dissolved in Dichloromethane and spin coated on the cleaned glass surface. Using a sharp needle a scratch was created on the film. Using AFM, the thickness of the film was measured. Figure 3.5 (a) shows an AFM image of a corner of the scratch on polymer film whose line profile is shown in Fig. 3.5 (b). The data shown in Figs. *a&b* are measured on the sample of 0.1% PMMA in dichloromethane show the thickness of the polymer layer in the order of 4-5 nm. To calibrate the measurements, standard grooved AFM samples were measured afterwards and their result were compared with measured polymer thicknesses. Films with thickness less than 4 nm were also tried which were very unstable in contact with the tip. For thinner films, after a few scan lines tip removed a large portion of the polymer from the surface. Therefore 0.1%wt of PMMA in dichloromethane was taken as standard for all samples of nanocrystals, circled in Fig. 3.5c. In order to study the variation of the film thickness with PMMA content, different solutions of PMMA in dichloromethane were prepared

and their thickness were measured using the technique described above, results are shown in figure 3.5c. Data points are averaged over 5 line profiles in different regions of the sample surface. Standard deviations of the averaging form the error bars. It shows a linear dependence of the film thickness as a function of the PMMA content with a slope of 34.8 (nm/%wt). Samples of PMMA in toluene showed almost twice the thickness compared to samples with dichloromethane as solution. This was one reason for selecting dichloromethane as the solvent. Moreover, dissolving PMMA in dichloromethane was done relatively fast, which in case of toluene needed sonicating for a few minutes.

3.2.5 1PE Confocal Microscopy of Single Emitters

Lifetime of the excited state in single molecules is dependent on the orientation of the transition dipole moment. Lifetime of a molecule oriented parallel to the dielectric interface is shorter than the perpendicular ones [63]. Moreover, orientation of the molecules with respect to the illumination polarization determines the coupling strength between molecule and excitation field [64]. For a molecule with transition dipole \vec{p} under illumination by electric fields \vec{E} , transition rate is proportional to $|\vec{E} \cdot \vec{p}|^2$. Highest transition probability and highest count rate occurs when the light is polarized along the transition dipole of the molecule. Therefore, orientation of the transition dipole of single molecule is an important characteristic which dramatically influences their photoluminescence behavior. Annular illumination has been proposed to map out the 3D orientations of transition dipole moments of single molecules [65]. Annular illumination (Fig. 3.6e) in contrary to full illumination (Fig. 3.6a) changes the field distribution inside the laser focus. Under full illumination, illumination angle using a high numerical aperture objective lens (NA=1.4) is around 70°. However, annular illumination with blocking

the central part of the beam (using a disk) while entering the objective changes the illumination angle. In our case, with disk diameter of 4 mm and objective back-aperture of 8 mm, illumination angle becomes $\theta_1 - \theta_2 = 35^\circ$. This enhances the longitudinal field components as compared to transverse components. As a result, molecules with different orientations probe different field components represented by different patterns in the confocal images. Therefore, in order to select a proper probe for the experiments with bowtie nanoantennas, luminescent properties of single molecules should be studied.

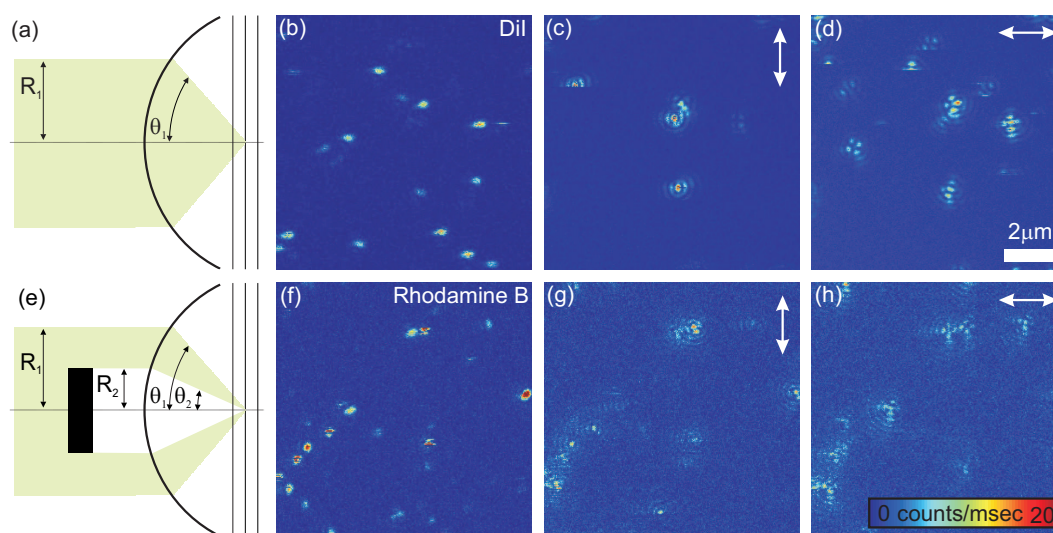


Figure 3.6: One photon excitation confocal image of DiI molecules embedded in PMMA. (a) Confocal image with complete illumination under 200 nW laser intensity. (b) Describes the annular illumination configuration and the angles. (c) DiI molecules under annular illumination, arrow shows the laser polarization in the image. (d) Annular illumination with cross polarized light with respect to (c).

Confocal images of DiI and RhodamineB are shown in Figs. 3.6b&f. Laser polarization in both images is the same as *c&g*. Different single molecules show different photoluminescence rates which is highly dependent on the orientation of the transition dipole of each single molecule. Annular illumination was used to de-

termine the orientation of each molecule. Figures 3.6 *c&d* show DiI molecules and *g&h* show RhodaminB molecules under annular illumination. Patterns observed from DiI molecules in *c* change while turning the polarization by 90-degree *d*. In addition, comparing *c&d* and some single molecules which were absent in *c* are not appearing with turning polzation in *d*. This might be attributed to inefficient coupling of the field components to transition dipole, therefore no fluorescence is detected. RhodamineB molecules also show different patterns under annular illumination (*g&h*), depending on the orientation of each transition dipole. With turning the laser polarization similar changes as DiI take place. More information about annular illumination and precise determination of 3D orientation of transition dipole using annular illumination patterns can be found elsewhere [66]. Due to strong response of single molecules to the local field distribution, they have very strong potential for field enhanced experiments with the tip. The main problem on this way is their relatively high photobleaching quantum yield which will be discussed later.

Single semiconductor nanocrystal are another type of single emitters whose fluorescent behavior can be used to probe the field of the bowtie nanoantenna. Originated from their semiconductor nature, photoluminescent is caused by the formation of electron-hole pairs inside the nanocrystal, radiative relaxation leads to generation of photons. The absorption behavior of a nanocrystal is highly influenced by its physical size [67]. Nanocrystal quantum dots are known to have very high quantum efficiencies which is measured cery close to unity [68]. Figure 3.7 shows the absorption and emission of nanocrystal sample measured at the ensemble level¹.

Emission of the sample is centered at 585 nm with a width of around 25

¹Measured by OceanOptics spectrometer, USB2000

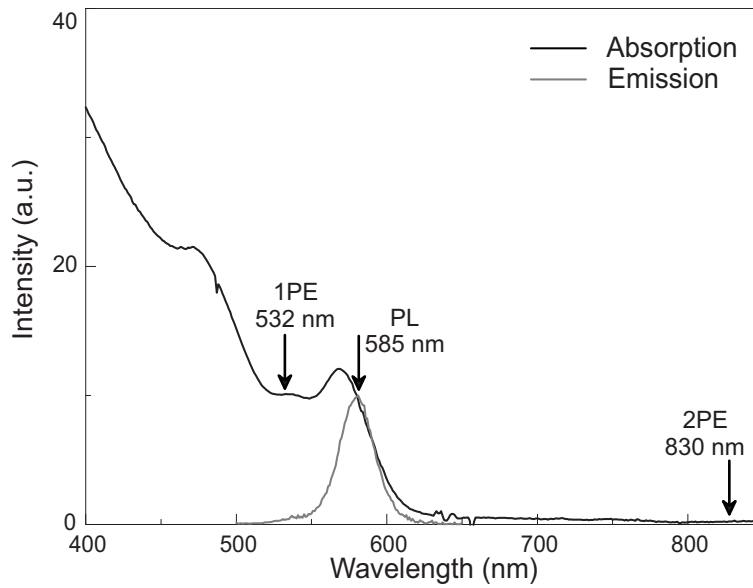


Figure 3.7: One-photon absorption and emission of quantum dot nano crystals. Black is absorption and gray is emission. The arrows show the emission peak which is at 585 nm, 532 nm arrow is the one-photon excitation wavelength and 830 nm is the two-photon excitation wavelength.

nm. Excitation frequencies for one- and two-photon excitation are marked on the absorption spectrum. Under one-photon excitation using a laser wavelength of 532 nm, non-resonant emission leads to a redshift in the emission wavelength, 585 nm. Energy difference between excitation and emission is more enhanced under two-photon excitation compared to one-photon processes. This is an important feature which will be used for interpretation of results in contact with bowtie nanoantennas under two-photon excitation. Fluorescence confocal microscope was used to study single nanocrystal under one-photon excitation. Results shown in Fig. 3.8. With laser intensity of 200 nW single nanocrystals can be imaged with very good signal-to-background ratio which was kept as standard laser power for one-photon experiments with nanocrystals. Intensity image of nanocrystals (Fig. 3.8a) shows a rather broad distribution of count rates among

single nanocrystals. This can be attributed to the different orientation of the transition dipole moments with respect to the exciting electric field, as for single molecules. However transition dipole moment of nanocrystals is different than the one for single molecules. Nanocrystals, unlike single molecules, do not have a linear transition dipole. They possess a two-dimensional degenerate transition dipole along the xy -plane of the wurtzite structure. Electronic transitions occur along this "bright plane" [17].

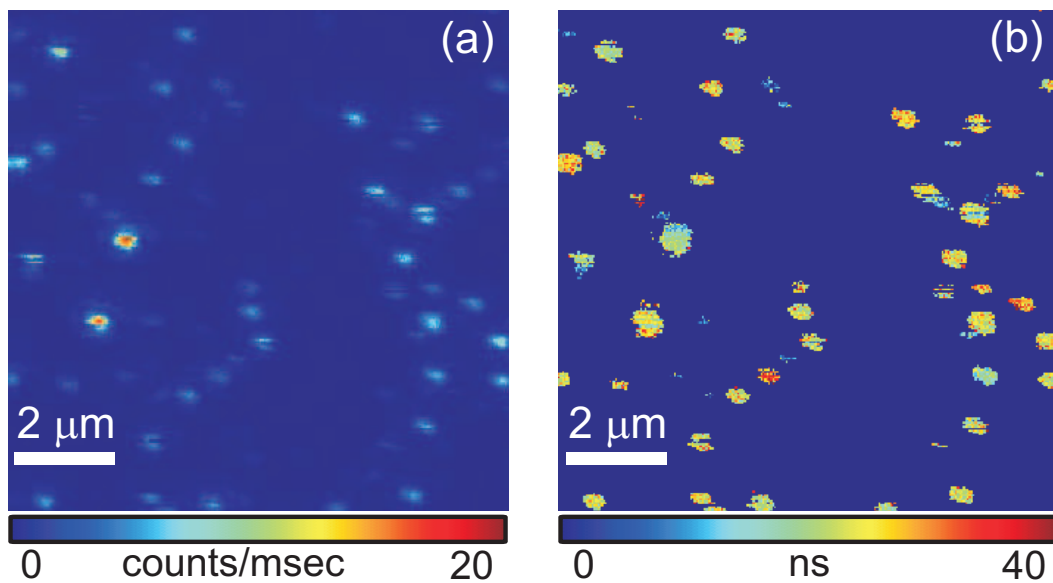


Figure 3.8: Confocal image of single semiconductor nanocrystals under one-photon excitation (a) intensity image and (b) lifetime image.

Fluorescence intensity provides some information about excitation and emission channels of single emitters. However, lifetime of the excited-state of the fluorophore is also an important characteristic response which requires detailed studies. Excited-state lifetime provides the knowledge about radiative and non-radiative transitions of the single emitter. Therefore, for each intensity of nanocrystals lifetime image is also presented. Figure 3.8b shows the lifetime image of the qdots with intensity image in Fig. 3.8a. Measured lifetime of the excited-state

of colloidal CdSe{ZnS} nanocrystals is centered around 20 ns in agreement with the literature [69]. Distribution of excited-state lifetimes is also broad, covering a span between ~ 10 -40 ns. This can also be described with the diversity in orientation of the transition dipole with respect to the dielectric interface. Hence, due to variations in photoluminescent behavior specifically PL intensity, an accurate data should be based on average over very many of them. Section 3.5 shows studies on saturation behavior of single nanocrystals which have been statistically analyzed over ~ 90 single nanocrystals.

3.3 Two Photon Excitation (2PE)

The main motivation for performing two-photon excitation with wavelength of 830 nm, is the dependence of the bowtie nanoantenna response on the laser wavelength. Micro-fabrication techniques are restricted in downscaling the antenna sizes to very small structures. Therefore, using a laser with longer wavelength (830 nm) can help to compensate possible micro-fabrication limits. This requires fluorescence studies on single chromophores under two-photon excitation using confocal microscopy. As a result of these studies, PL intensity and lifetime of single emitters as well as the saturation behavior can be understood.

3.3.1 Principle of 2PE

Two-photon excitation is a process in which a fluorophore is excited by simultaneous absorption of two photons with half of the required energy. In the corresponding one-photon excitation, this process is done by absorption of one photon with enough energy[70]. Figure 3.9a shows the principle of one- and two-photon

excitations schematically. Under both excitation schemes emission frequency of the fluorophore remains the same. To perform the two-photon process time intervals between excitation photons should be very short. Therefore, pulse duration of the laser needs to be small to increase the possibility for two photons to be absorbed simultaneously. This is usually done using short pulsed lasers, in the range of 100 femtoseconds, below saturation two-photon fluorescence count rate can be written as [71],

$$C_f \propto \frac{\eta \xi \sigma^{(2)} N_A^4 I^2}{\lambda^2 \tau f} \quad (3.2)$$

in which η is the fluorescence quantum efficiency, ξ is the photon detection efficiency, $\sigma^{(2)}$ is two photon absorption cross section, N_A is the numerical aperture of the objective lens, I is laser intensity, λ center wavelenth of the laser pulse, f repetition rate of the laser, and τ is the pulse width. As it can be seen two-photon fluorescence signal is inversely proportional with the laser pulse duration.

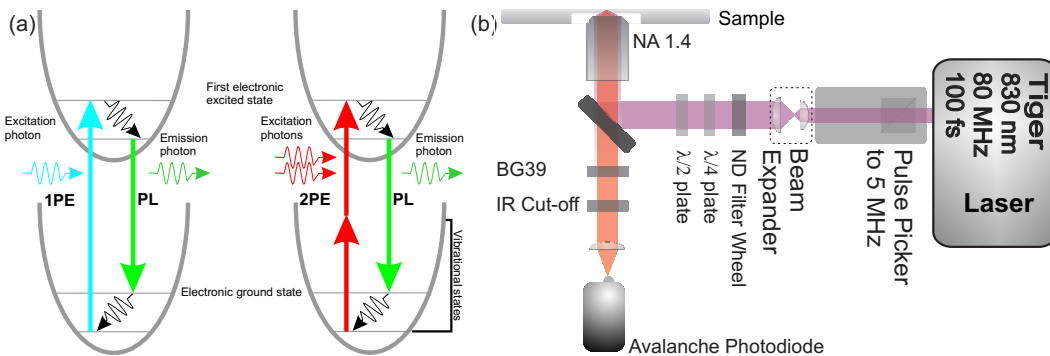


Figure 3.9: (a) Schematic representation of one and two photon excitation. As can be seen in 2PE two photon with half the energy excite the electron simultaneously to the excited state. Excited electron after recombining emits a photon whose energy is determined by the energy difference between the two levels. (b) Home-made Confocal set-up for 2PE.

A very important feature of two-photon excitation is shrinking the excitation

volume to the actual focal point [71]. This increases the signal-to-background ratio considerably. This might be attributed to the possibility of two-photon absorption only inside the laser focus. Simultaneous absorption of two-photons by the single emitters changes the dependence of emission intensity on the excitation power. Below saturation, power dependence of the PL intensity is linear which changes to quadratic under two-photon excitation. This has been observed for instance for case of single nanocrystals [72].

3.3.2 Description of the 2PE Confocal Set-up

Laser source in our two photon experiments is a femto-second laser (Tiger, Time Bandwidth Products, Zurich). Center wavelength is 830 nm and pulse duration 100 fs. Repetition rate of the laser cavity is 80 MHz which is reduced to 5 MHz for lifetime measurements using the pulse picker. The diameter of the beam as released from the cavity is around 2 mm which expanded to 8 mm using a telescopic beam-expander. Intensity and polarization of the expanded beam were controlled using a set of neutral density filters and waveplates. Waveplates used here are broad-band plates from CVI Laser, fabricated specifically for femtosecond lasers. Using a dichroic mirror (770DCXR, Chroma Technology Inc.), laser light was reflected to the back-aperture of the objective lens. BG39 (Schott Glass) and SP600 (Chroma Technology Inc.) were used to block the remained infrared light and AFM laser in the detection path, whose transmission spectra are shown in figure 3.10. Experimental results based on confocal images of single molecules and nanocrystals showed that a combination of both cutoff filters results in a better signal-to-background and signal-to-noise ratio. *Collection efficiency* of the optical setup for two-photon excitation was determined around $\sim 1.8\%$. This is slightly less than the one-photon setup which is caused by BG39 removing a large

portion of the fluorescence.

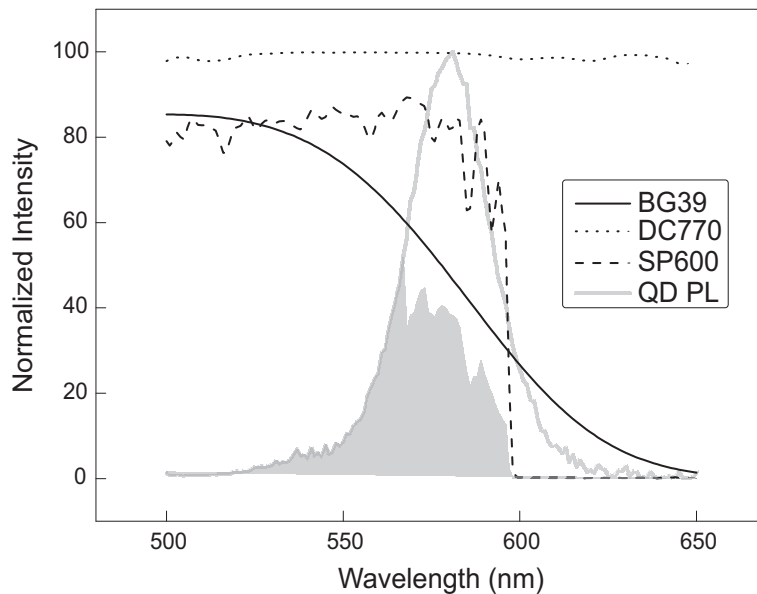


Figure 3.10: Transmission spectra of all filters in the detection path of two-photon excitation setup used for confocal imaging and tip experiments. Gray line is the emission spectrum of QDot sample at the ensemble level. The shaded area is the portion of the nanocrystal photoluminescence which is detected by APD.

3.3.3 2PE Confocal Microscopy of Single Emitters

Absorption cross section of single emitter system under two-photon excitation is much smaller than the one-photon process. For dye molecules this is usually around $\sim 10^{-50} \text{cm}^4 \text{s}$ [73]. For instance for Exalite-428 embedded in PMMA is measured around $30 \times 10^{-50} \text{cm}^4 \text{s}$ [74]. However, semiconductor nanocrystals have very large absorption cross section under two-photon excitation as compared with other types of emitters [75]. Measured in solution, two-photon absorption cross section of nanocrystal is $2 - 47 \times 10^{-37} \text{cm}^4 \text{s}$, which is the highest reported two-photon absorption cross section. For our experiments, two types of fluorophores (molecular dyes and nanocrystals) with sufficient two-photon absorption cross section

were selected. RhodamineB, as the molecular dye, was selected which is a well known molecule with good two-photon absorption cross section (as well as one photon) [71]. Moreover, as mentioned already semiconductor nanocrystals with large two-photon absorption cross section (qdots) are another candidate for two-photon experiments. Two-photon fluorescence confocal images of both emitters are shown in Fig. 3.11, *a&b* are intensity images of Rhodamine B and nanocrystals. Under the same laser power ($60\mu W$) nanocrystals show relatively higher PL intensity than rhodamineB molecules. Lifetime image of qdots under two-photon excitation (Fig. 3.11c) shows similar values as in one-photon excitation, around 20 ns.

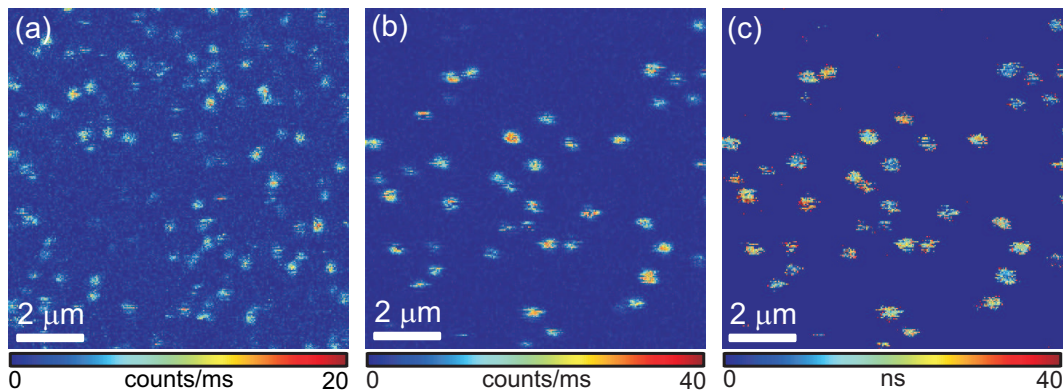


Figure 3.11: PL intensity and lifetime images of Rhodamine B (a) Nanocrystals (b &c) under 2PE.

3.4 Nanocrystals vs Single Molecules

Photo-stability is an important characteristic for an emitting probe in nano-optics. Stability is mainly related to photobleaching time, which is the time that a single emitter, located inside the laser focus, can emit photons before it photobleaches. Time scale of most experiments for probing the interaction between

the tip and the single emitter, is beyond a few minutes. Therefore, stability is an important factor in single emitter selection. Such a selection influences the data quality and information obtained from the tip-emitter interaction, dramatically. Here, a comparison between the stability of rhodamineB molecules and nanocrystals is presented. The results show the reason why nanocrystals have been selected as the probe for tip-experiments.

In order to compare the stability of single Rhodamine B molecules to single nanocrystals in one- and two-photon excitation, time-traces of both systems were acquired which are presented in Fig. 3.12. Under one-photon excitation, (Fig. 3.12a&b) nanocrystal shows a higher count rate which is continuously emitting over a few minutes. Single molecule counterpart, (b), bleaches faster with lower PL intensity. This comparison shows the higher potential of single nanocrystals over single rhodamineB molecules in one-photon experiments. The difference is even more pronounced under two-photon excitation shown in Fig. 3.12. It can be seen that qdots are clearly the dominant probe in two-photon processes. They emits a higher rate of photons over the entire experiment. In the time-trace shown in (c) after 900 seconds bleaching is not observed. However, Rhodamine B molecule with relatively lower PL intensity, turns off completely after almost 150 sec.

Photobleaching of single molecules is known to be due to chemical changes under laser excitation, especially reaction with oxygen in the presence of air. Thus, with supplying nitrogen environment single molecule bleaching time can be extended which introduces strong blinking effects [76]. Blinking of single molecules in nitrogen environment is due to longer lifetimes of the triplet states [77]. Quantum dots also show blinking behavior known as fluorescence intermittency of nanocrystals which is known to be due to charge trapping on the

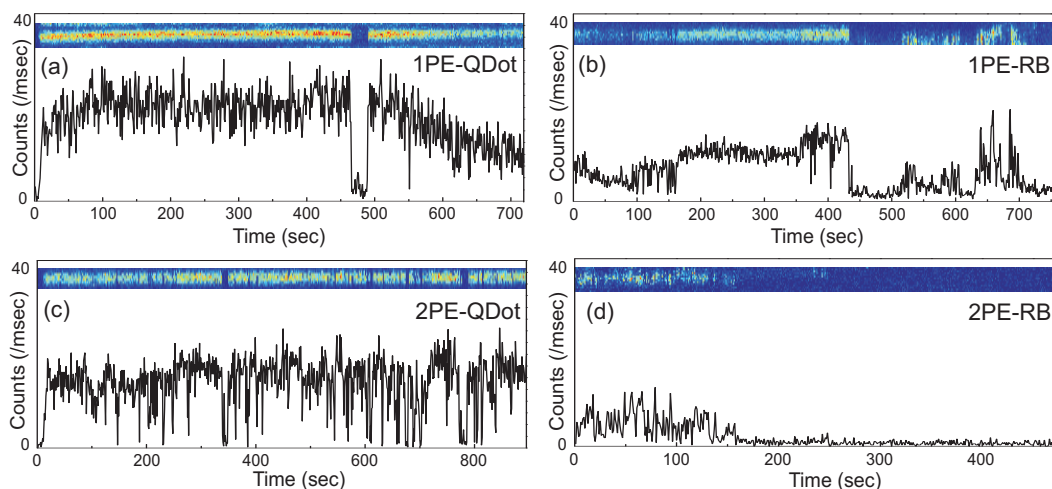


Figure 3.12: Comparison of the stability of the single emitters under one ((a) & (b)) and two ((c) & (d)) excitations.

surface of quantum dot or Auger ionization processes [78]. Photobleaching of quantum dots is most likely caused by chemical changes inside the laser focus, for instance oxidation, however this is only an speculation [78]. Comparing the photostability of nanocrystals and rhodamineB molecules based on the measurements shown in Fig. 3.12 show that nanocrystals are more stable system to be selected for antenna tip experiments. For such experiments fluorophore must emit photons for several minutes up to about an hour while located inside the laser focus. This is simply not the case for single rhodamineB molecules. Therefore, single $CdSe\{ZnS\}$ semiconductor nanocrystal were selected as probes for antenna experiments. Photoluminescence saturation behavior of nanocrystals will be studied in detail in the following section.

3.5 Power Dependence of Single Nanocrystals

Since PL intensity of single emitters (as two-level systems) saturates at high laser intensities, power dependence studies of the PL count rate is an important diagnostic measurement of the chromophore system. From this measurements saturation behavior of the chromophore system is understood, which relates the excitation level to possible electronic transitions inside the single emitter. This section presents statistical power dependence studies on nanocrystal system, from which saturation level of the system is measured. Saturation behavior of single emitters is an important factor in experiments with tip. For instance, once the system is pumped close to saturation, emission enhancement leads to leads to increased PL intensity in addition to lifetime reduction. Therefore, understanding this parameters of the chromophore system is important.

3.5.1 Theory

With increasing the excitation intensity, the emission rate of a two-level system increases to a certain level. Beyond this level emission intensity saturates which means there is no longer increase in the PL rate with increasing the excitation intensity. This describes the saturation behavior of a two-level system which is characterized by two parameters, R_∞ and I_s . R_∞ corresponds to the highest emission intensity which occurs at very high excitation powers. I_s is the excitation intensity at $R_\infty/2$ [16]. In order to obtain the power dependence of a two-level system, population of ground and excited states upon laser illumination must be considered. Figure 3.13 shows the conditions of the system schematically. I is the excitation intensity where n is dependent on the excitation scheme. $n = 1$ for one-photon and $n = 2$ for two-photon excitation. $\sigma^{(n)}$ is the absorption cross

section of the system k_{12} denotes the excitation rate and k_{21} the relaxation rate which is a sum of radiative and non-radiative rates. Since we consider a non-fluorescence, γ is the relaxation rate from higher vibrational states to the excited state which is much faster than k_{21} [79]. $|1\rangle$ represents the ground state and $|2\rangle$ corresponds to the excited state.

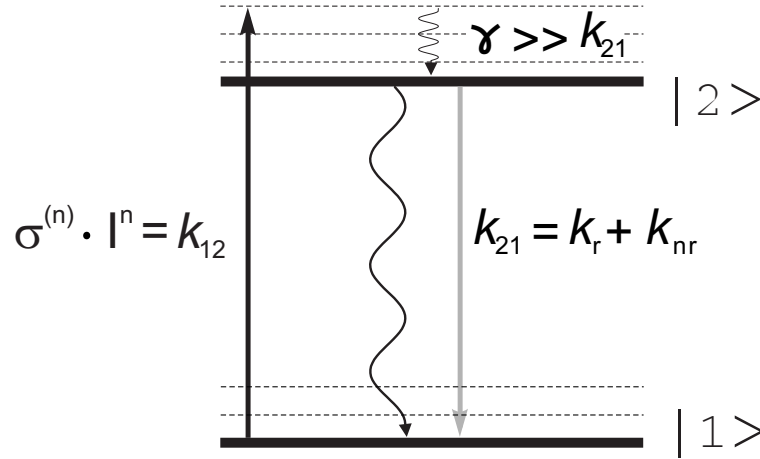


Figure 3.13: Simplified Jablonski diagram of a two-level system. $\sigma^{(n)}$ is the absorption cross section, I is the excitation intensity, k_{12} is the excitation rate and k_{21} is the recombination rate. k_r and k_{nr} are radiative and non-radiative rate, respectively. γ is the relaxation rate from higher vibrational states to the excited state due to non-resonant pumping and $n=1$ for 1PE and $n=2$ for 2PE.

Upon excitation by the laser, population of the states can be written as,

$$\dot{p}_1 = -k_{12}p_1 + k_{21}p_2 \quad (3.3)$$

$$\dot{p}_2 = k_{12}p_1 - k_{21}p_2 \quad (3.4)$$

Written in a matrix format we have,

$$\begin{pmatrix} \dot{p}_1 \\ \dot{p}_2 \end{pmatrix} = \begin{pmatrix} -k_{12} & k_{21} \\ k_{12} & -k_{21} \end{pmatrix} \begin{pmatrix} p_1 \\ p_2 \end{pmatrix} \quad (3.5)$$

Using,

$$p_1 + p_2 = 1 \quad (3.6)$$

equation 3.3 is re-written,

$$\dot{p}_1 = -kp_1 + k_{21} \quad \text{with} \quad k = k_{12} + k_{21} \quad (3.7)$$

With solution for p_1 ,

$$p_1 = \frac{k_{12}}{k} \quad (3.8)$$

Excitation rate depends on the absorption cross section ($\sigma^{(n)}$) and excitation intensity (I^n). Here n is again the parameter depending on the excitation ($n=1$ for one-photon and $n=2$ for two-photon process). Therefore we have,

$$k_{12} = \sigma^{(n)} \cdot I^n \quad \text{and} \quad R = p_1 \cdot k_r \quad (3.9)$$

In which R is the fluorescence rate of the system. Solving equations 3.8 and 3.9 we will have the following format for the power dependence,

$$\frac{R}{k_r} = \frac{\sigma^{(n)} I^n}{\sigma^{(n)} I^n + k_{21}} \quad (3.10)$$

Assuming the system is at saturation we have the following assumptions in which R_∞ is the count rate at saturation and I_s is the intensity at $R_\infty/2$,

$$k_{21} = I_s^n \sigma^{(n)} \quad \text{and} \quad R_\infty = k_r \quad (3.11)$$

Based on the relations of 3.11, equation 3.10 can be re-written,

$$R = R_\infty \frac{\left(\frac{I}{I_s}\right)^n}{1 + \left(\frac{I}{I_s}\right)^n} \quad (3.12)$$

Equation 3.12 can be re-formatted for one- and two-photon excitations. For one-photon excitation (n=1) we will have,

$$\text{1PE Power Dependence} \quad R = R_\infty \frac{(I/I_s)}{1 + (I/I_s)} \quad (3.13)$$

And for two-photon excitation (n=2) will be written as,

$$\text{2PE Power Dependence} \quad R = R_\infty \frac{(I/I_s)^2}{1 + (I/I_s)^2} \quad (3.14)$$

Equation 3.13 shows the linear dependence of the emission intensity on the laser power below saturation which under two-photon process becomes quadratic, equation 3.14.

3.5.2 Results

Meaningful saturation data about single nanocrystals should be based on statistics over many quantum dots. The main reason for this is the large variations in emission intensity of nanocrystals under the same excitation power which is reflected in Figs. 3.8 and 3.11. For this purpose, photoluminescence confocal images with different laser powers were acquired under both one- and two-photon excitation of a freshly prepared sample. Each of the nanocrystal in the image form a diffraction-limited spot with a size of around 300 nm which approximately

has a Gaussian intensity distribution. All the pixels with intensity values between the maximum of each spot and 90% of the maximum were averaged. The results of this average determines the count rate of that specific dot at a specific intensity. To determine the emission intensity at each laser power, count rate of all dots were averaged which results in the emission count rate at the used laser power. The standard deviation of the final averaging was used to quantify the distribution of PL rates over all dot at each power, which forms the error bars.

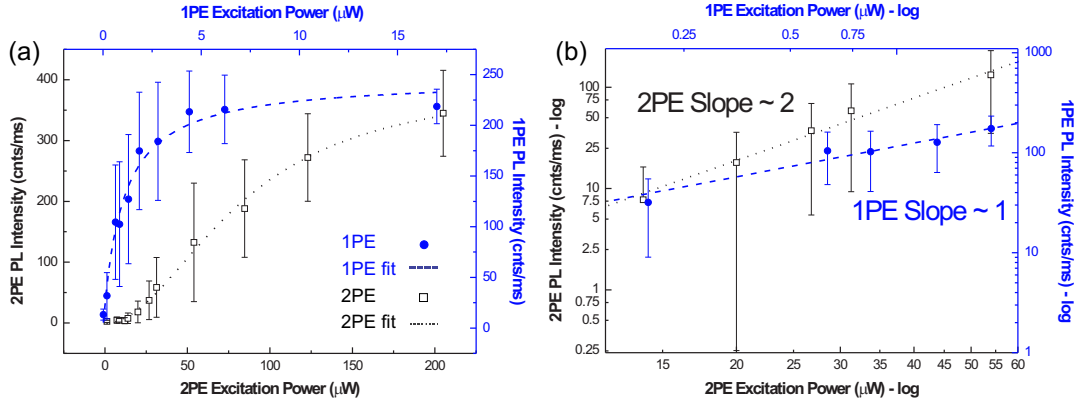


Figure 3.14: (a) Dependence of PL rate of CdSe{ZnS} quantum dots on the laser power. Averaged over ~ 90 single dots. (b) Log-log scale of data points below $2 \mu W$ for 1PE and below $60 \mu W$ for 2PE.

Figure 3.14a shows the data for both types of excitation. Solid-blue circles are the data for one-photon excitation with axes on right and top. Hollow-black rectangles are the data for two-photon excitation with axes on left and bottom. Both data are averaged over around 90 nanocrystals falling into the confocal image. With fitting the power dependence curves based on equations 3.13 and 3.14, saturation intensity and count rate at saturation can be determined (i.e. I_s and R_∞ , respectively). Under one-photon excitation count rate saturates at 246 counts/ms whose corresponding saturation power is $0.98 \mu W$. Under two-

Table 3.1: Saturation data of single nano crystals based on ~ 90 different dots

Saturation Data	1PE	2PE
R_∞ (cnts/ms)	246 ± 10.1	396 ± 11.3
I_s (μW)	0.98 ± 0.14	82 ± 3.4
I_s (W/cm^2)	24.5 ± 3.5	820 ± 34
$\sigma^{(n)}$	$5.9 \pm 2 \times 10^{-15} (cm^2)$	$20 \pm 16 \times 10^{-37} (cm^4 \cdot s)$

photon excitation, saturation of PL count rate occurs at 396 counts/ms with corresponding saturation power of $82 \mu W$. However, it should be taken into account that these values are convoluted with the detection efficiency of the setup, which around 2% for both one- and two-photon setups. Dashed-blue line and dotted-black line are the fit for one- and two-photon excitations, respectively. Saturation data obtained based on this fit are shown in table 3.1. It should be mentioned that excitation power is replaced by excitation intensity. To calculate the intensity, laser power data should be divided by $0.04 \mu m^2$ for one- and by $0.1 \mu m^2$ for two photon excitations. These numbers are based on the diameter of the diffraction-limited laser focus. Although statistics show that the count rate at saturation is about the same for both one- and two-photon excitations, saturation intensity for two-photon is much higher which as mentioned earlier is due to the two-photon processes. Another important point in table 3.1 is the absorption cross section ($\sigma^{(n)}$) of quantum dots calculated based on the data taking into account the emission wavelength at 585 nm corresponding to 2.12 eV with the energy of $3.4 \times 10^{-19} J$. Calculated values are, $\sigma^{(1)} = 5.9 \pm 2 \times 10^{-15} cm^2$ and $\sigma^{(2)} = 20 \pm 16 \times 10^{-37} cm^4 s$. These results match are in close agreement with data presented in literature for one- [67] and two-photon [75] excitations.

In order to confirm that the observed effects are one- and two-photon processes, data points below the onset of saturation in PL count rate were selected, which corresponds to below $60 \mu W$ for 2PE and below $2 \mu W$ for 1PE. These data

points are plotted in a log-log scale in Fig. 3.14 (b). As in (a) solid-blue circles are one-photon excitation and empty-black rectangles are two-photon excitation data points. Linear fit to one-photon excitation data points shows a slope of ~ 1 and for two-photon excitation results a slope of ~ 2 . This confirms that measured signals are in accordance with the characteristics of each excitation regime.

Chapter 4

Antenna Tip Fabrication

As it was described in section 2.2, resonance behavior of an antenna is highly dependent on the total length of the antenna with respect to the wavelength of the incident light. Therefore, bowtie nanoantennas which are resonant with light at optical frequencies should be fabricated with nanometric dimensions. Feedgap of such antenna which defines the amplitude and confinement of the enhanced EM fields, needs to be as small as possible. In this respect to extend the limits of optics at nanometer scales, confinement of around 10 nm is of major attention. In a top-down approach, choosing the right micro/nanofabrication is the major task. The goal for using these sophisticated microfabrication methods is to be able to design well-defined bowtie antennas at the apex of AFM tips. Length of each arm of such bowtie structures should hardly extend from 100 nm, separated by a small distance of $< 20\text{nm}$. Electron beam lithography (EBL) provides the possibility for fabricating small structures. However, resolution in EBL is not sufficient for designing such small feedgaps. Moreover, pyramidal shape of the tip increases the complexity of the structure which requires more controllable fabrication methods. Therefore, focused ion beam (FIB) as one of the most capable micromachining

techniques (*and most expensive, too*) was selected to perform this task. In focused ion beam milling, an ion beam is used to bombard the sample surface. Collisions between the incident ions with high momentum and enough energy kick out atoms from the surface [80]. Therefore, by scanning the ion beam in a specific pattern desired structures can be sculptured on the surface. In this chapter procedures that have been taken for producing bowtie nanoantennas at the apex of AFM tips are discussed, which include metal evaporation on the surface of pre-cleaned tips and subsequent FIB milling.

4.1 Metal Evaporation

Silicon nitride contact-mode AFM probes made by Veeco Instruments¹ (DNP) were selected as substrates for bowtie nanoantennas. Specifications of these tips are presented in table 4.1. These tips with pyramidal shape have an average base width of $4\mu\text{m}$ and an average height of $3\mu\text{m}$. Nominal tip radius is on the order of 20 nm and average cantilever force constant is in the range of 0.06 (N/m). Since the force constant of the cantilever influences the force between the tip and sample, is an important parameter in contact-mode AFM.

Table 4.1: Specifications of contact-mode AFM tips

Material	Silicon Nitride
Tip Radius (nom.)	20 (nm)
Tip Base Width (nom.)	4 (μm)
Tip Height (nom.)	3 (μm)
Cantilever Force Constant (nom.)	0.06 (N/m)

Due to the strong tendency of dust particles to be absorbed at the tip apex, pre-cleaning of the tips before metal evaporation is an important starting point.

¹http://www.veecoprobes.com/probe_detail.asp?ClassID=1

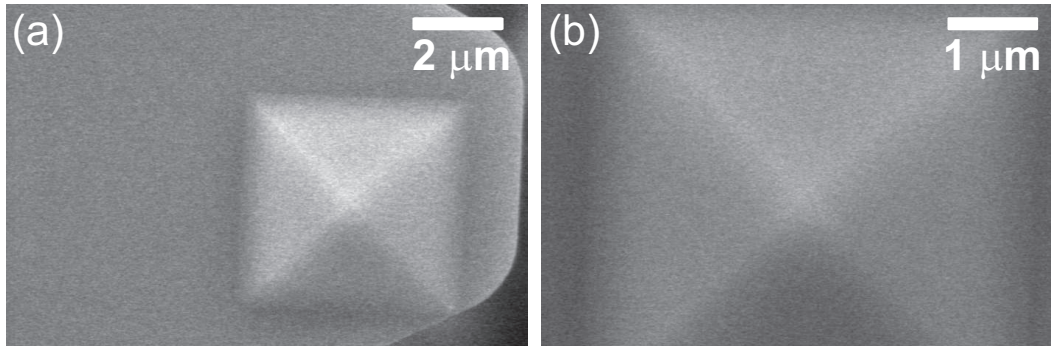


Figure 4.1: (a) and (b) SEM image of the cleaned tip before metal evaporation showing the surface of the Si_3N_4 tip.

For pre-cleaning, a batch of tips were left in ethanol container for 15 minutes. During this period, dust particles which were possibly absorbed at the tip apex were washed away by the solution. The result of such a procedure is a clean surface of the tip. Figure 4.1 shows an SEM image of a tip directly after cleaning by this method. As can be seen there is no contamination at the surface of the tip. In some cases where the cleaning has not been sufficient, dust particles trapped at the apex could be seen in SEM images. Pre-cleaned tips were transferred to evaporation chamber, *without* drying the remained ethanol on the surface. This was done, to prevent the dust particles to be reabsorbed at the tip apex. The ethanol remained on the tip surface will immediately be sucked away in the vacuum chamber. By this procedure, out of each batch almost 95% of the tips showed completely smooth surfaces after cleaning and they were suitable for BIB milling.

Metal evaporation consists of coating a thin layer of Aluminum on the surface of cleaned tips. This is a very important step, because bowtie antenna will be fabricated at the apex of metall coated tips. Therefore, precise monitoring the environment is necessary. Evaporation ² was done using resistive heating with a

²Evaporation system: Balzers BSV080

tungsten boat under very low pressures ($10^{-6}mbar$). Thickness of the metallic film was monitored using a quartz resonator. In order to make sure that the measured values by quartz resonator are correct, a glass slide was coated under the same conditions as tips. Thickness of the metallic layer was measured by AFM topography on artificially made scratches of the glass surface. Thicknesses measured by quartz resonator were in agreement with AFM measurements. For equal homogeneity in different batches of tip, evaporation rate of $\sim 2nm/sec$ was kept constant for all the tips. During evaporation a thin metallic layer with thickness of 40 nm covers the whole surface of the tip and cantilever. Thicker layer of metal can lead to bending of the cantilever which is not suitable for AFM operation. Visible bending of the cantilever is most probably due to different thermal expansion coefficients of the metal and the Si_3N_4 substrate. On the other hand, during ion beam alignments (stigmatism and focusing) material is removed from the surface. Therefore, thickness of metal should be slightly more than what is wanted for the thickness of the final antenna. Metallic layers with thicknesses less 40 nm can not survive the FIB adjustments. If cleaning and evaporation steps have been done correctly, a "fully-coated tip" with homogeneous metal film on top is achieved. Figure 4.2a shows an SEM image of a fully-coated tip in the top-view which has been prepared under well-controlled conditions. "No" contamination is seen around the tip apex. This quality of fully-coated tips is needed for structuring bowtie antennas at the tip apex.

For information about the tips apex side view images are usually more helpful than top view images. This is because, any type of contamination particles attached to the tip apex appear immediately as a protrusion in the side view. However in top view images this information is covered by charging of the edges. Therefore, more detailed analysis of the tip is done using the side view image,

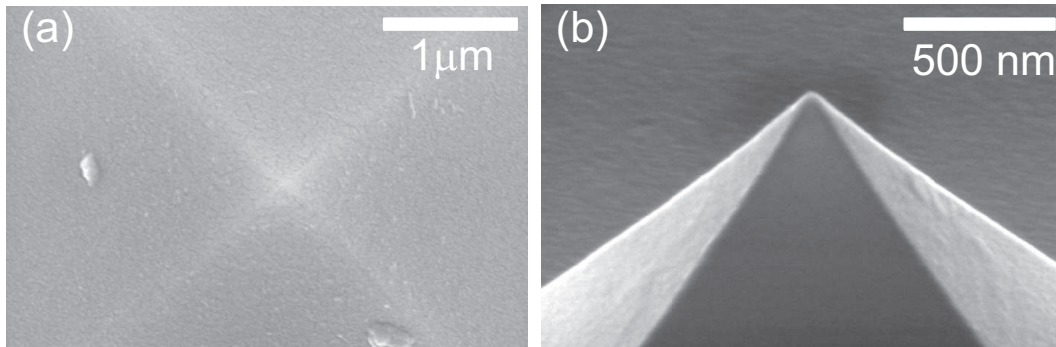


Figure 4.2: SEM image of the fully coated tip which shows the smooth surface of metal film necessary for FIB milling (a) Top view & (b) Side view.

Fig.4.2b. This image shows the very clean tip apex which is perfect for FIB milling.

4.2 Micro-Fabrication of Nano-Antennas

Designing antenna structures on fully-coated flat substrate and apex of AFM tips was done using focused ion beam milling (FEI Nova 600³). Milling parameters, including pattern positioning and exposure time were found using trial structures on the flat substrate which is explained in part 4.2.1. For this purpose one region of the cantilever surface, which is made of the same material as the tip, was selected as flat substrate. After finding the right milling parameters on the flat substrate, patterns can be placed on the tip apices. However, some small adjustments of the pattern at the tip apex is needed. These changes are mainly introduced by the conical shape of the tip, which will be explained. By this approach, minimum amount of tips are used for designing the patterns.

³EMPA, Duebendorf and EPFL, Lausanne

4.2.1 Structuring on the Flat Substrate

After placing the sample in dual-beam chamber, sample is tilted by 52° . In this condition, ion beam is normal to the sample surface. An ion beam image of the cantilever surface is shown in Fig. 4.3a. Based on several trial structures, ion beam current was found 10 pA as the best choice for our samples. Ion beam with current of 100 pA has a large diameter which is not suitable for fine structures [80]. In contrary, 1 pA has small radius but due to long exposure times needed for milling can not define sharp structures. This can be attributed to heating the metal by time which leads to melting. Moreover, dielectric substrate (Si_3N_4) can also causes drifts induced by charge accumulation of the surface. Moreover, since each ion current needs separate alignment in focus and stigmatism, 10 pA current was kept constant for all the patterns. Calibration file required for ion beam was selected to be Silicon small (*Si_small*) found by the quality of the trial structures. Calibration file determines the time required for each specific milling depth. This is calculated automatically by the software for each specific calibration file, taking into account ion beam current and size of the pattern. However, for more controlled milling in our work, exposure times were reduced to numbers which yielded better structures. These milling times are presented in tables 4.2 and 4.3. Each bowtie antenna was structured in three separate steps which are discussed in the following sections.

Pattern 1: Triangles

In the first step two triangles are milled away. Triangular shape of the pattern defines the bowtie shape of the antenna. This is shown by two white triangles in Fig.4.3b. Each triangle has a base width of 700 nm and height of 200 nm. These dimensions depend on the length scales of the desired structures. For each triangle exposure time of 5 sec was found optimum with 10 pA current

on the flat substrate as described in table 4.2. In milling the triangles a small distance between them is necessary. This is due to the overlap of the ion beam in the upper and lower triangles which leads to large gaps in the final antenna structure. Optimum distance between the triangles on the flat substrate was found 50 nm at best. With larger distances between triangles, the final bowtie antenna will not have sharp edges at the feedgap of the antenna, which is not favorable. Taking into account all the conditions mentioned, both triangles can be milled away *in series*, i.e. sequentially. The result of this step is an infinite bowtie structure remained on the surface.

Pattern 2: Linecut

In the structure left from the first step two arm of the bowtie antenna are connected. A linecut separates two arms of the antenna and forms the antenna feedgap. Therefore this step which is shown in Fig. 4.3c is very important in the quality of the final antenna. For an ideal antenna, feedgap should be as small as possible. With a current of 10 pA, 2 sec exposure time lead to smallest possible gap on the flat substrate. Since ion beam current of 1 pA has smaller radius could be a good option for the linecut which would lead to small gaps. This idea was tried on some tips, but as it was mentioned already since 1pA ion beam needs different stigmatism and focusing, size and quality of the final feedgap was worse.

Pattern 3: Boxes

To this step, an infinite bowtie antenna with separated arms is fabricated. Milling the two white boxes shown in Fig.4.3d, determines the length of each antenna arm. Distance between the two boxes is equivalent to the total length of the final antenna, L_T . For boxes with dimensions of $420 \times 450(nm^2)$ optimum exposure time was found 10 sec per box.

After milling all the patterns, ion beam can image the surface. Fig.4.3e shows

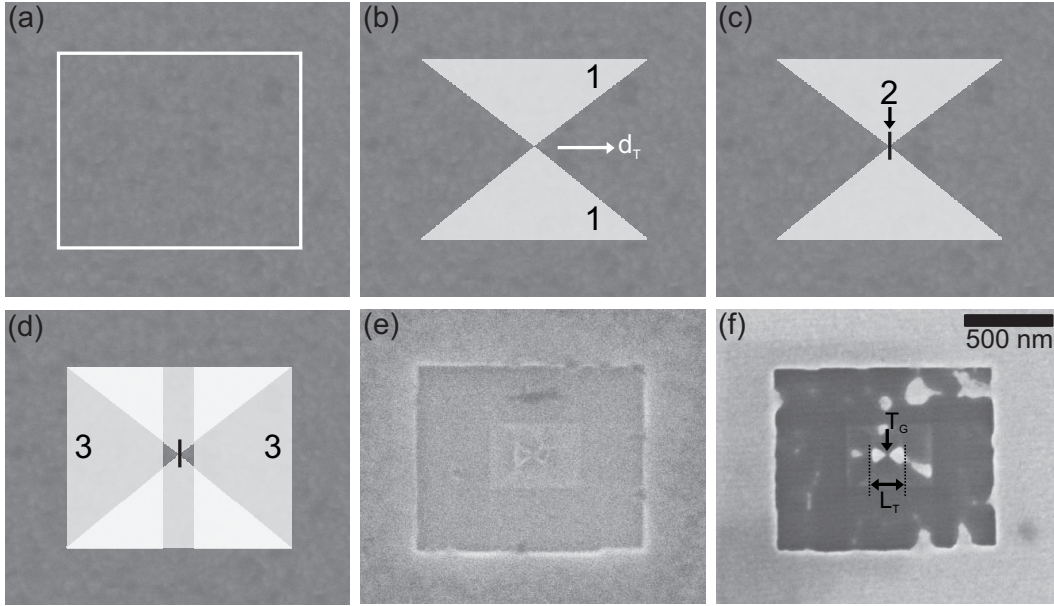


Figure 4.3: (a) Ion beam image of a region on cantilever surface. The white rectangle shows the area of interest for milling. (b) **Pattern1 : Triangles**, two white triangles are milled by the ion beam. Distance between the triangles is (d_T) is 50 nm for optimum gap size. (c) **Pattern2 : Line**, linecut shown by the black line creates the feed gap. (d) **Pattern3 : Boxes**, the two white boxes shown, will be milled to define a specific length for the bowtie antenna. (e) Ion beam image of the antenna fabricated by previous steps. (f) Electron beam image of the same area as *e*. T_G and L_T are the gap size and total length of the antenna, respectively. All images and patterns are in the same scale as (f).

Table 4.2: Details of FIB Structuring on the flat substrate

Pattern	Mater. File	Ion Cur.	Time ^a	Dim.(nm)	Distance
1: Triangles	Si_small	10 pA	5 sec	700×200	50 (nm)
2: Line	Si_small	10 pA	2 sec	100	
3: Boxes	Si_small	10 pA	10 sec	420×450	L_T

^a Exposure times for triangles and boxes are times per triangle and/or box.

an ion image of the bowtie antenna made by the above procedure on the flat substrate. A more clear image of the surface is provided by the electron beam (Fig.4.3f) from which dimensions of the antenna can be measured. This image shows a bowtie nanoantenna which consists of two triangular arms separated with a small gap (T_G). Specifications of each pattern for structuring on the flat substrate is presented in table 4.2. These patterns can in principle be applied to the apex of fully-coated tips. However, due to pyramidal shape and conical angle of the tip each pattern undergo some small changes which will be illustrated in the next section.

4.2.2 Structuring at the AFM Tip Apex

In the previous section fabricating bowtie nanoantennas on a flat substrate was described. Milling parameters obtained, based on these trial structures are good starting point for antenna fabrication at the tip apex. Of course, due to conical angle of the apex some changes will be necessary which are discussed here in detail. Figure 4.4a shows an ion image of the tip apex, on the top-view. Ion beam stigmatism was kept the same as flat substrate. Due to different height of the tips with respect to each other and with respect to cantilever surface (flat substrate) ion beam focusing was done for each individual tips. In the following step how each pattern is applied to the tip apex is explained.

Pattern 1 & 2: Triangles

Figure 4.4b shows two white triangles which will be milled away. With a beam current of 10 pA, optimum milling time for each triangle was set to 2 sec. Relatively less exposure time for milling the triangles at the tip apex compared to flat substrate is caused by the conical angle of the tip. In this condition ion beam is not normal to the tip surface. This increases the efficiency of the

Table 4.3: Details of FIB patterning at the tip apex

Pattern	Mater. File	Ion Cur.	Time ^a	Dim.(nm)	Distance
1&2: Triangles	Si_small	10 pA	2 sec	700 × 200	20(nm)
3 : Line	Si_small	10 pA	0.3 sec	100	
4&5: Boxes	Si_small	10 pA	3 sec	420 × 450	L_T

^a Exposure times for triangles and boxes are times per triangle and/or box.

collisions between bombarded ions and atoms of the surface. This can be easily understood in an analogy with angle of the carpenter's hand, sculpturing the on wood. Another change caused by the tip shape is the distance between the two triangles, which is reduced to 20 nm. Due to the pyramidal shape of the tip apex, distance between the ion beam and surface increases as the ion beam moves away from the apex. As a result, the overlap of the ion beam in milling two triangles is reduced.

Pattern 3: Linecut

Figure 4.4c shows the linecut which produces the antenna feedgap. Milling time of 300 ms was found optimum which lead to smallest possible gap, around 20 nm. Less milling times were also tried but due to lack of enough time, ion beam failed to separate two arms of the antenna.

Pattern 4 & 5: Boxes

By cutting the two white boxes in Fig.4.4d, length of each antenna arm is defined. In total, distance between these white boxes in the pattern determines the total length of the antenna (L_T). Minimum possible milling time for each box with an ion beam of 10 pA was found 3 sec.

4.2.3 Fabricated Bow-Tie Antennas

Figure 4.5 shows three type of bowtie nanoantenna tips fabricated by the procedure explained above. Although the tip shown in *a&b* was produced in another

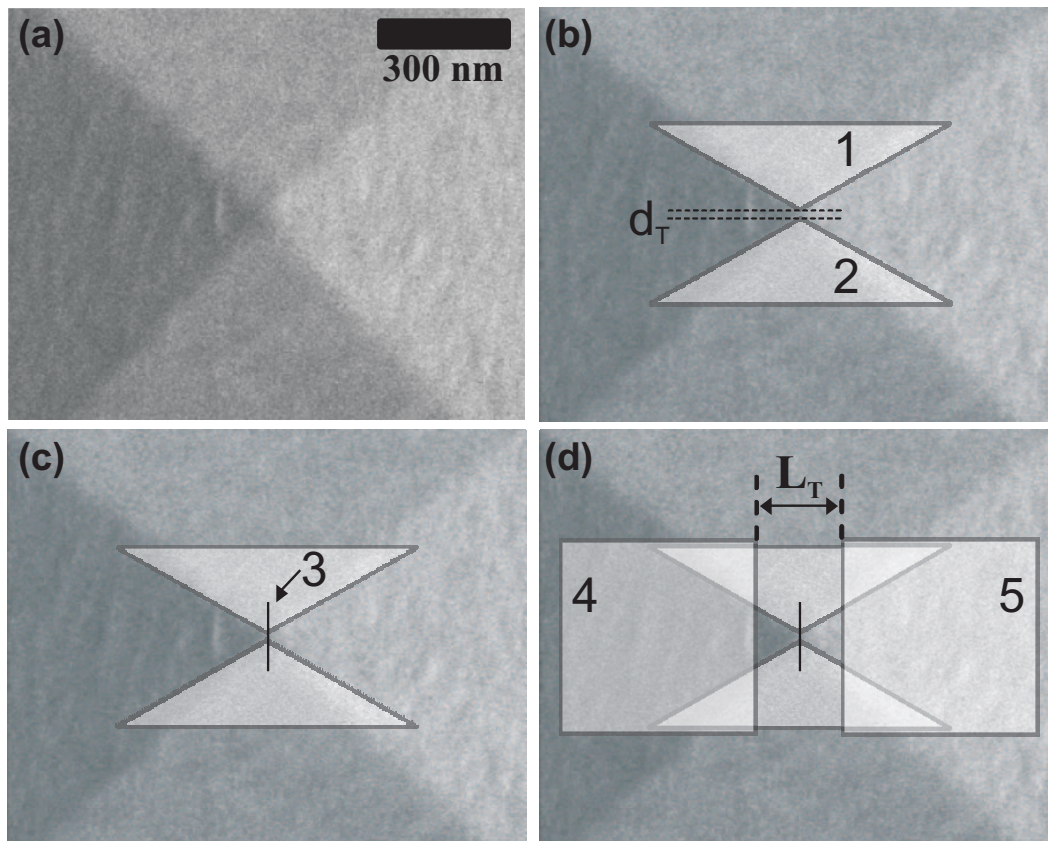


Figure 4.4: (a) Ion beam image of the tip apex, where the structures are supposed to be sculptured. (b) **Pattern1&2 : Triangles**, two white triangles are milled by ion beam which defines the bowtie shape. Distance between the triangles, d_T is 20 nm. (c) **Pattern3 : Linecut**, linecut with exposure time of 300 ms forms the antenna feedgap. (d) **Pattern3&4 : Boxes**, by milling the two white boxes, a bowtie antenna with desired length at the tip apex is formed. L_T determines the total length of antenna. All images and patterns are in the same scale as (a)

batch, but it resembles some of the tips have been produced in this series. Therefore, its properties is explained as a function of the milling steps. Such a tip, with relatively large gap size, was fabricated while triangle patterns are placed with zero distance. As can be seen gap is relatively large (around 70-80 nm). With increasing the distance between the triangles to around 20 nm, feedgap of the antenna reduces to minimum possible. In this case feedgap is completely determined by the **linecut**, such a tip is shown in *c&d*. Controlling the antenna length by fabrication parameters can be seen in comparison between *c&e*. This is controlled by the distance between the **boxes** in FIB patterning as explained earlier in section 4.2.2. It should be mentioned that since the milling is done at the cone of a pyramid, the total length of the antenna is not exactly what is defined by the pattern, i.e. distance between boxes. In Fig.4.4d, distance between the two boxes in the FIB patterns were 200 nm. However, measured from the SEM images, total length of the antenna in this case is around 250 nm. This is visible by a slight contrast of the metal with respect to the silicon nitride substrate.

Obviously, ion beam not only cuts the metal but also some depth of silicon nitride is removed by milling. According experimental experiences, this has been the case only with aluminum. Using gold as the metal, no milling of the silicon nitride was observed. This is probably due to the lack of enough time for ion beam caused by sample drifting. Positioning the boxes more closely will lead to the tip shown in (*f*), with smaller L_T . This tip is already loosing the bowtie shape, therefore, this scale for antenna length ($\sim 150nm$) can be the limit for FIB milling. Apparently these dimensions are at the edge of the FIB capacity defined by the ion beam radius [80] which is a function of the ion beam current (here 10 pA). For tip shown in *a&b*, flare angle of the antenna, radius of curvature of antenna arms and feedgap width determined from SEM images are, 40° , 30 nm

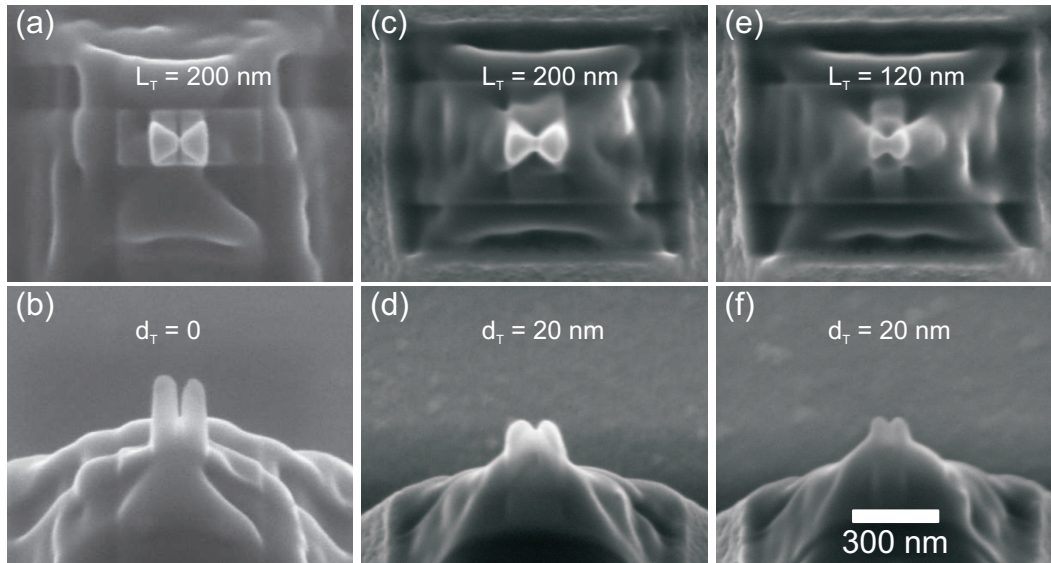


Figure 4.5: SEM images of three different bow-tie antenna fabricated by FIB with different fabrication parameters. (a), (c) & (e) are top views and (b), (d) & (f) are side views. d_T is the distance between the two triangles in ion beam pattern and L_T is the distance between the boxes in ion beam pattern described in figure 4.4.

and 50 nm, respectively. For the other two antenna flare angle stays the same. However, radius of curvature and feed gap width for the bowtie of *c&d* is around 20 nm and 20 nm respectively. Bowtie of *e&f* has the same properties of *c&d* with shorter antenna arms, estimated from SEM image around 150 nm.

Chapter 5

Tip - Quantum Dot Interactions

As it was explained in section 2.3, with approaching a metallic tip to a single quantum emitter, several processes can take place. Metallic tip by opening new decay channels for the emitter can dissipate the energy non-radiatively, which leads to fluorescence quenching. On the other hand, localized EM fields of the tip (antenna feedgap) can enlarge the absorption cross section and therefore, enhanced excitation. Resonant coupling of the antenna dipole to the quantum emitter can lead to enhanced emission via promoting the radiative decay rates. Depending on the weight of each process, either quenching will happen or enhancement. The goal of the experiments in this chapter is to study the interaction of a bowtie nanoantenna in contact with the single quantum emitter. Two signatures of the single emitter, PL intensity and lifetime are used to probe this interaction. Experiments presented here were done under one- and two-photon excitation. In order to probe the interaction between the antenna tip and a single nanocrystal, first one nanocrystal was immobilized inside the laser focus and its position was adjusted by maximizing the count rate. Antenna tip scans an area around the nanocrystal. Photoluminescence intensity and excited-state lifetime

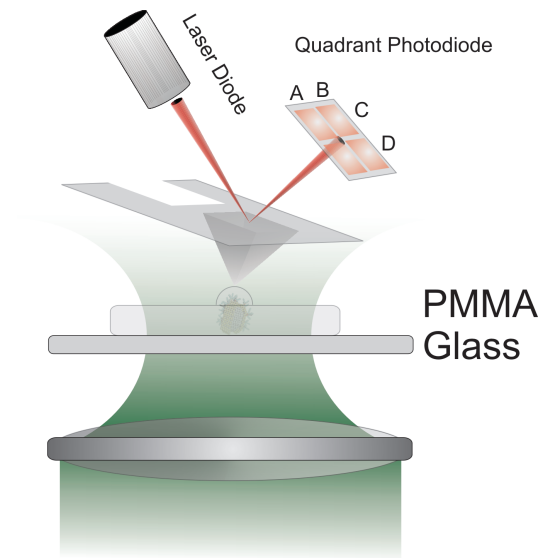


Figure 5.1: Nanocrystal is immobilized inside the laser focus and tips scans around focal area. PL count rate and lifetime of the nanocrystal is measured as a function of the tip position.

of the nanocrystal is measured as a function of the tip position. This is shown schematically in Fig.5.1. When the tip is far from the nanocrystal, the nanocrystal acts as a free emitter. Approaching the tip to the nanocrystal perturbs the emission characteristics and we consider a new system consisted of antenna and nanocrystal, antenna/NC system. A comparison between a fully-coated tip and bowtie antenna tip will help in explaining the results of antenna tips.

5.1 Tip-Sample Force-Interactions

Atomic force microscopy was used to probe the interactions between the tip with sample. AFM tip with the bowtie antenna at the apex approaches the surface and scans on the sample in contact-mode. Apex of the tip consists of aluminum whose mechanical yield strength is much less than silicon nitride. Therefore, in order to maintain the tip performance, forces between the sample and tip should

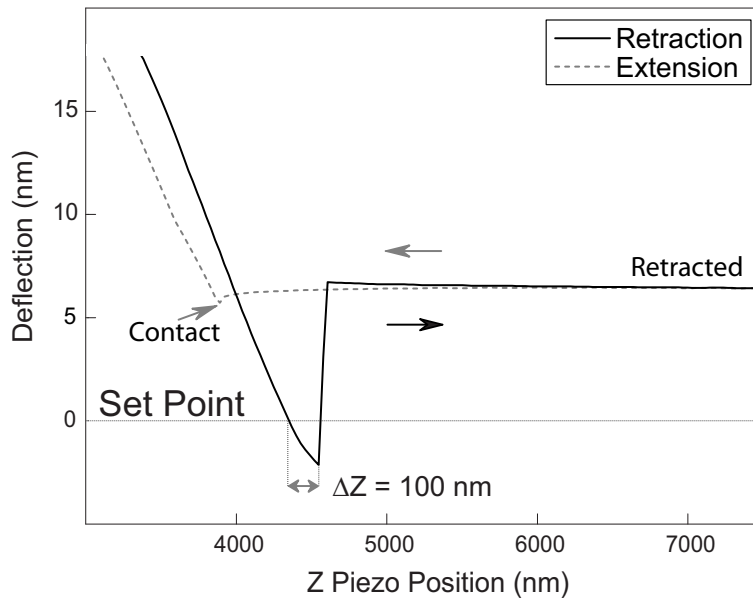


Figure 5.2: Force curve obtained from an antenna tip after experiments.

be as low as possible. High contact forces between the tip and sample can easily deform the bowtie antenna structure leading for instance, to shortcuts between the two arms. This is even more enhanced under laser illumination which heats up the environment by depositing a large amount of energy per excitation pulse. In order to reduce the forces during the experiments set-point was reduced as low as possible.

Figure 5.2 shows the bowtie antenna tip-sample interaction in contact-mode AFM. Tip starts approaching the sample from the point marked as "retracted". As the tip approaches the surface there is no change in the deflection signal of the cantilever, as measured by quadrant photodiode. Dashed gray line shows the approaching procedure. At the contact point with the surface suddenly the deflection signal begins to increase which is a clear sign for the tip going into contact with the sample. Deflection increases as piezo moves downwards until it reaches a plateau. At the onset of contact point between tip and sample a very

small dip in the deflection signal can be seen. This is caused by attractive forces between sample and tip, which causes the tip to snap to the surface. However, retraction response of the tip is different than approach procedure. In retraction (black line in figure 5.2) deflection decreases much further than the retracted level. This is caused by the attractive forces between the tip and the sample surface which keeps the tip in contact although the piezo is moving upwards. This goes on until the pulling force of the piezo overcomes the attractive forces at tip-sample junction. This follows by a sudden separation of the tip which causes the step increase in the deflection signal. After this point tip is no longer touching the sample surface and is completely retracted. Since set-point defines the deflection signal maintained by the feedback loop, distance between the point that deflection signal crosses the set point and the minimum point is directly related to the force between sample and tip. According to this, the distance that piezo travels (Δz) multiplied by the cantilever force constant (K) gives the force ¹

$$F = K \cdot \Delta z = 0.06(N/m) \times 100(nm) = 6(nN) \quad (5.1)$$

Reducing the set-point to the minimum possible level leads to a force of around 6 nN based on the cantilever force constant. This is relatively low force regime between tip and sample which makes the microscope very sensitive to the vibration in the environment and requires the damped optical table.

¹BioScopeTM Scanning Probe Microscope, Instruction Manual, Digital Instruments Inc., Santa Barbara, CA.

5.2 Fully Coated Tips: Quenching

The purpose of this experiments is to see the influence of a fully-coated tip (a metallic interface) on the emission of a single nanocrystal. One single nanocrystal was immobilized inside the laser focus. Laser intensity (1.8 W/cm^2) was kept much lower than the saturation intensity presented in table 3.1. After optimizing the position of the quantum dot inside the focus, metallic tip scans around the nanocrystal while its fluorescence intensity and lifetime are being measured. Corresponding maps are shown in Fig. 5.3. As can be seen in (a) and (b) when the metallic tip is close to the nano crystal fluorescence intensity decreases dramatically. This is a sign of quenching of PL in contact with the fully-coated tip. Fully-coated tip dissipates the energy by opening new decay channels for the excited state. Looking at the lifetime response (Fig. 5.3c) as another tool more detailed knowledge can be gained. In contact with the antenna PL lifetime is much shorter than the free nanocrystal. This shows that the total decay rates in contact with the antenna is more.

Assuming P/P_0 as the relative radiated power to the far field in contact with the probe, for a free system with unit quantum efficiency, position dependent quantum efficiency of can be written as the following [81]:

$$\eta(x, y) = \frac{k_r}{k_r + k_{nr}} = \frac{P/P_0}{k/k_0} \quad (5.2)$$

Where $\eta(x, y)$ is the position dependent quantum efficiency, k_r and k_{nr} are the radiative and non-radiative rates, respectively. $k = k_r + k_{nr}$ in the presence of the probe and k_0 is in the absence of the probe. From equation 5.2 it can be understood that tip as the immediate environment of the emitter opens new decay channels for the emitter which increases the non-radiative rates dramatically.

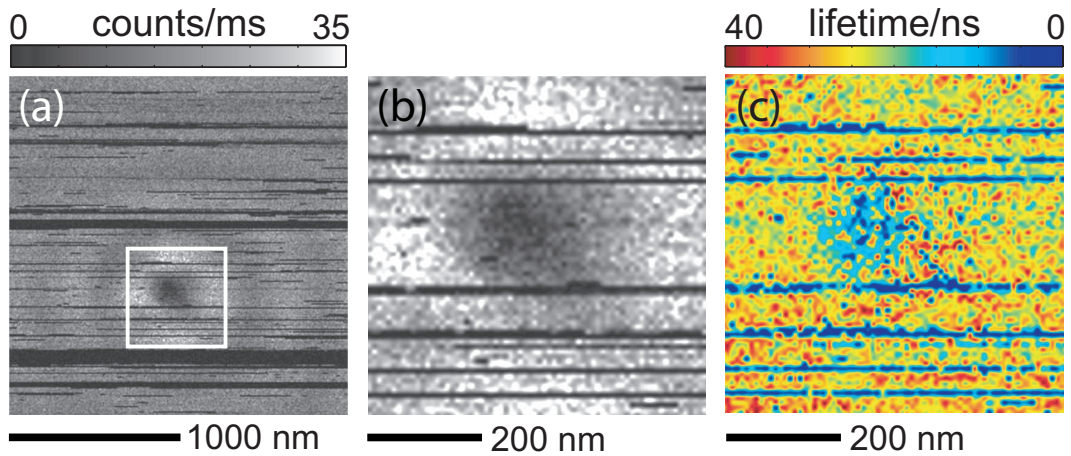


Figure 5.3: PL count rate (a) and (b) where (b) is the zoom of the area marked in (a) with corresponding lifetime image (c) as a function of the fully-coated tip position.

This leads to a reduction in quantum yield and therefore less radiated power and shorter lifetime (τ) since $\tau = 1/k$.

5.3 Antenna Tips: Enhancement

In the previous section it was shown that approaching a metallic tip to a quantum dot located inside the laser focus quenches the photoluminescence by opening new decay channels for the excited state. From a resolution point of view, the quenched area is highly confined to the tip apex and the size of the quenched area can be reduced by sharpening the tip. Thus, using a very sharp metal tip, a single quantum emitter can be resolved by the resolution defined by the tip apex radius [14]. However, quenching is not a favorable effect, since the emitter has been turned "off". Therefore, in order to resolve a single emitter with high-resolution and high-sensitivity, the quenching effect should be overcome. In other words, a proper approach should lead to enhancement of the single emitter rather than

quenching, is the main task in this respect. Field enhancement has been achieved using sharp metallic tips with laser polarized along the tip axis which causes localized enhanced fields at apex of the tip. Although by this method, enhanced excitation has been observed by tip induced two-photon excitation [82], the results hold only for J-aggregates with fast energy transfer along the aggregate. In this case the detected fluorescence originates far away from the tip, and the contact point between the tip and sample is most likely quenched. Field enhancement at apex of sharp metallic tips which is known as "lightning rod effect" has been successfully used tip-enhanced raman imaging of single-walled carbon nanotubes [83] with spatial resolutions down to $\sim 20nm$. Lightning rod effect can be simply explained as, accumulation of harmonically oscillating charges driven by the laser field at the apex of metallic tip, which leads to confined electromagnetic fields. Confined fields at the apex can enhance the absorption of the quantum emitter. According to this picture metallic tips can be used for field enhancement under proper illumination. In order to exploit the localized fields, metal should be in contact with the quantum emitter which introduces an "interplay" between *quenching* and *enhancement*. Therefore, metallic tip quenches the emission by non-radiative relaxation pathways or enhances the emission by localized electromagnetic fields at the apex. Depending on the weight of each effect fluorescence can be either quenched or enhanced. Competitions between these two processes has motivated many theoretical investigations on metallic tip and emitters [81, 84]. Results show that tip material and shape are very important parameters, as well as the distance between probe and single emitters, d which seems to be the major factor. Non-radiative rates induced by the tip vanishes by $1/d^3$, thus with a small separations between the tip and sample, electric field enhancement which is a longer range effect, can overcome quenching [84].

Here, the possibility of using "bowtie nanoantennas" for electric field enhancement has been investigated. Bowtie antennas with localized EM fields inside the gap are very good candidates for field enhancement purposes. Wavelength of incident light is an important issue since it determines the resonance behavior of the antenna. Therefore, experiments presented here have been done with two laser wavelengths 532 nm (1PE) and 830 nm (2PE).

5.3.1 One Photon Excitation

Set-up configuration for one photon excitation is described in section 3.2.1. An antenna tip shown in Fig. 4.5a&b was used to interact with quantum dot. One nanocrystal was immobilized inside the laser focus with wavelength of $\lambda = 532nm$ and repetition rate of 5 MHz with intensity of $1.8 W/cm^2$ which is far below the saturation level. Photoluminescence intensity ($R(x, y)$) and excited-state lifetime ($\tau(x, y)$) of the nanocrystal were measured while antenna scans around and over the quantum dot in $2 \times 2\mu m^2$ area. Corresponding PL rate and lifetime maps are shown in Fig. 5.4 [50]. First row ($a, b\&c$) are for laser polarized along the antenna and in the lower row ($d, e\&f$) laser is polarized perpendicular to the antenna. Orientation of the antenna in the scan image is shown at the bottom left of $a\&d$ and white arrows show the laser polarization.

Count rate and lifetime of the free nanocrystal was determined to be $\approx 15counts/ms$ and $\approx 26ns$, respectively. Looking at figure (b) can be seen that when the antenna crosses over the dot, generates a single maximum of the count rate in the range of $\approx 35counts/ms$ accompanied by strong reduction in the excited-state lifetime (c). This result is clearly in contrary with fluorescence quenching observed with fully-coated tips (Fig. 5.3). Maximum PL intensities are about the same for both polarizations but the excited-state lifetimes differ

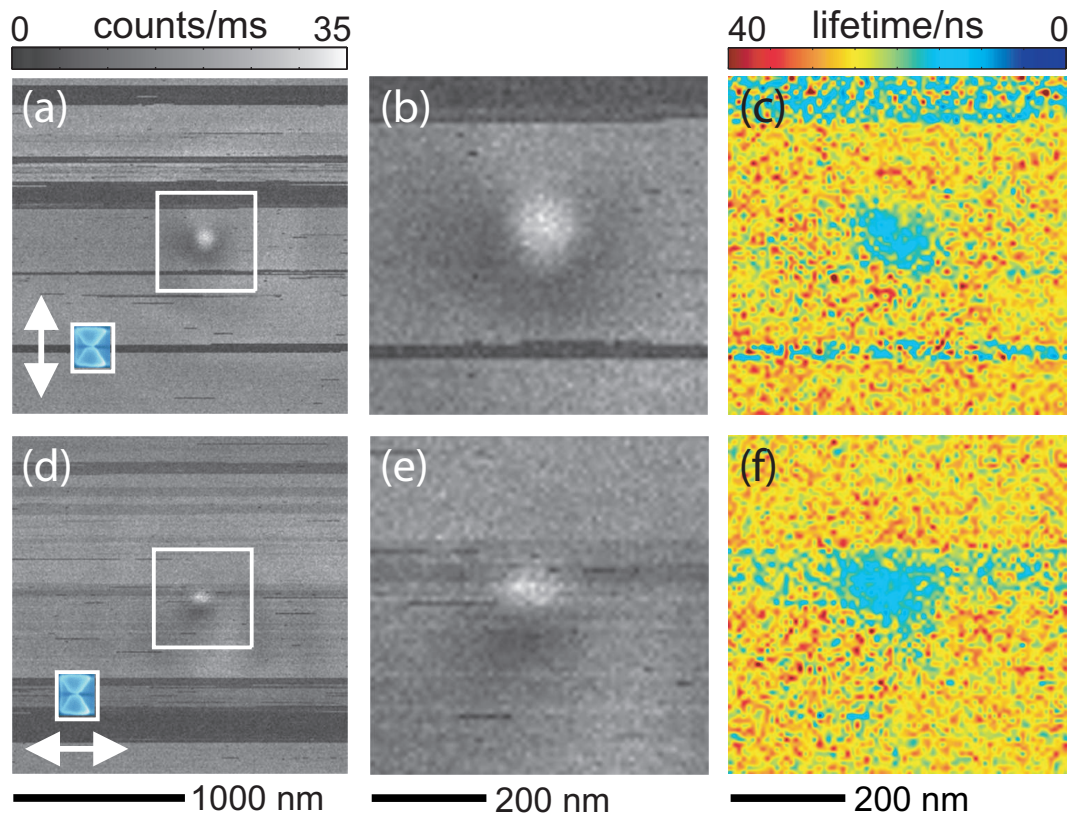


Figure 5.4: PL count rates (a), (b), (d) and (e). (b) and (e) are selected areas in (a) and (d), respectively. (c) & (f) are the corresponding lifetime images of (b) and (e). All images are as a function of the antenna position. Orientation of the antenna in the scan image is shown bottom left of the (a) and (d). White arrows show the laser polarization.

considerably (perpendicular: 10 ns; parallel: 15 ns). Contact point between the antenna feedgap and nanocrystal shows the maximum count rate. However, off center from the gap, count rate images show moderate quenching caused by antenna arms. The asymmetry of the quenched areas is most probably caused by the uneven height of the antenna arms.

Based on the above results, antenna feedgap results in field enhancement which in contact with the single quantum emitter increases the photoluminescence intensity and shortens the excited-state lifetime. Therefore according to

equation 2.17 there are two components in field enhancement, enhanced excitation and enhanced emission. Enhanced excitation, $|\alpha|^2$, is described by enlarging the absorption cross section of the free nanocrystal, σ_0 in contact with the antenna. Therefore nanocrystal coupled to the bowtie antenna has a larger absorption cross section, σ . This can be written as,

$$|\alpha|^2 = \frac{\sigma}{\sigma_0} \quad (5.3)$$

As a result of such process nanocrystal absorbs more photons in contact with the antenna. In other words, bowtie nanoantenna collects the photons from the environment and feeds in to the quantum system. Another enhancement occurs in the emission channel. Enhanced emission, $|\alpha'|^2$, is done by coupling the relaxation pathways of the quantum emitter to the dipole of the antenna feedgap. Depending on the coupling regime total rates of the free nanocrystal, k^0 , in contact with the bowtie antenna changes to k . Ratio of these two rates determines the emission enhancement factor. However, since quantum efficiency of the nanocrystals is very close to unity non-radiative rates can be neglected. Emission enhancement factor can be written as [85],

$$|\alpha'|^2 = \frac{k}{k^0} \approx \frac{k_r}{k_r^0} \quad (5.4)$$

Emission enhancement is due to higher recombination rates, $k > k^0$. Total decay rates of the nanocrystal is a combination of radiative and non-radiative rates. An increase in both rates, can decrease the excited-state lifetime. However, an increase in non-radiative rates leads to depletion of the photoluminescence intensity, as seen for fully-coated tips. Therefore, it can be concluded that the lifetime reduction in contact with the antenna feedgap is due to promoted radiative rates,

which introduces the second part in equation 5.4. Radiative rates of a quantum emitter with transition dipole, μ can be written as [59],

$$k_r = 2\pi\mu^2 \cdot \chi_{21} \cdot \rho_{21} \quad (5.5)$$

Where, χ_{21} is appropriate Franck-Condon factor and ρ_{21} is the density of available photonic states. Thus, influence of antenna feedgap on the radiative rates can be explained by higher density of photonic states in contact with the antenna. This is caused by the "dipole-dipole" coupling between the nanocrystal and antenna feedgap. This introduces some changes in the quantum yield of the system which is not observed in system with unit quantum efficiency (nanocrystals). In the presence of the antenna nanocrystal/antenna system is indistinguishable from an *effective* quantum emitter which can be called a "*superemitter*". Photophysical properties of such a superemitter can be widely adjusted with proper positioning the antenna structure. This is caused by enhanced emission of the qdot photoluminescence as well as enhanced excitation, in contact with the bowtie nanoantenna.

Present experiments demonstrates the tunability of the radiative and non-radiative decay rates of single quantum emitters by the proximity of bowtie nanoantennas forming a tunable superemitter. The absorption and emission properties of a superemitter can be optimized by appropriate combination of *single* quantum emitter and optical nanoantennas. Coupling the nanoantenna to emission or excitation channels requires precise micro/nanofabrication schemes which was done here by focused ion beam. In the above experiments nanoantenna was found to be resonant with both excitation and emission frequencies. Therefore both excitation and emission enhancements were observed. This can be

attributed to the antenna size which is slightly off-resonance with the excitation wavelength (532 nm). According to antenna theory [44] and experimental observation on optical antennas [46], under longer wavelengths (NIR), is more likely to reach the resonance of bowtie nanoantennas with length scales around 200 nm (Fig. 4.5). Therefore, similar experiments were performed under two-photon excitation ($\lambda_0 = 830\text{nm}$) which is presented in the following section.

5.3.2 Two Photon Excitation

In this section the aim is to study the interaction between antenna tips and single nanocrystals under 2PE. At first, response of the antenna tips in contact with the glass cover slips is discussed. Knowledge obtained from this results is used to separate nanocrystal and tip components. Finally qdot-antenna system under 2PE is studied.

Antenna-Glass Interactions under 2PE

Optical set-up used for this experiments is described in section 3.11. A cleaned glass coverslip was used as the sample. IR laser ($\lambda = 830\text{nm}$) with pulse duration of 100 fs was focused on the glass surface using a high numerical aperture objective lens, while tip is scanning around the focal area. Intensity and lifetime data were acquired as a function of the tip position. Fig. 5.5 shows the intensity response of the antenna tip in contact with the glass surface. Antenna tip under illumination by 830 nm laser light show a strong background with laser polarized along the antenna. With laser polarization perpendicular to the antenna, background signal decreases considerably, confirming a excitation polarization dependence for the signal. Lifetime response of this signal (Fig. 5.5c), shows very fast components. This decay is basically the instrument response of the optical setup.

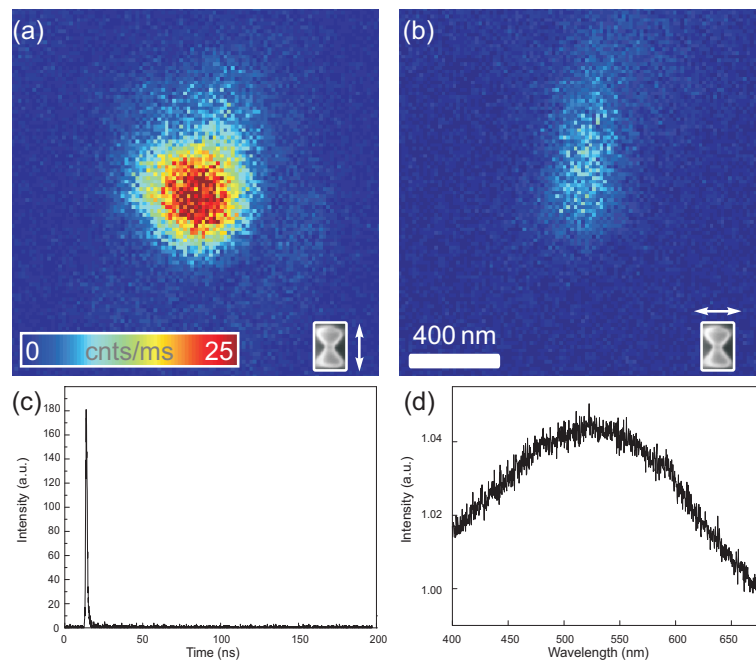


Figure 5.5: Interaction between antenna tip and glass surface. (a) Intensity image of the tip-background with laser polarized along the antenna and (b) polarized perpendicular to the antenna. (c) Lifetime response of the tip background (histogram of the arrival times) which is equivalent to the instrument response. (d) Spectrum of the bright spot observed in (a-b).

Spectral investigations of the background light were done by sending the light in the detection path to a sensitive spectrometer ¹. Dispersed light was detected using a charge-coupled-device (CCD) ². Spectrum of the light with the tip in contact was normalized, by the spectrum acquired with laser source blocked, as well as the spectrum with retracted tip. This normalization removes all the background signal from the spectrum. Corresponding spectrum of the background signal is shown in Fig.5.5d. Antenna tip background covers between 400 to more than 650 nm. The spectrum of the tip-background is in close agreement with white light generated at the feedgap of dipole antenna [46] and photoluminescence observed from metallic nanoparticles [86]. The possibility for second or third harmonic generation at the tip is not valid, because the optical window in acquiring the data in Fig.5.5a is between 550-600 nm.

It can be seen that the tip background spectrally overlaps with quantum dot emission which is centered at 585 nm. Assuming that a quantum dot is present in the interaction area it is not possible to split the signals from the dot and tip, using optical filters. The only difference in characteristic between observed tip background and quantum dot signal is the lifetime response. Quantum dots have a decay with lifetime of around 20 ns. This means photons from quantum dot have longer arrival times than the photons from the tip. This is because nanocrystal emission is a consequence of excitation-recombination cycles. Therefore, temporal gating is the only way to separate these two category of photons, nanocrystal component and tip component.

¹*InSpectrum*, Acton Research Corp., MA

²Andor Technology

Principle of Time-Gated Imaging

As it was explained earlier the only difference between the signal from the tip and quantum dot is the arrival times of the emitted photons. Figure 5.6a shows decay of a quantum dot while the antenna tip is in contact. The sharp peak at the beginning of the decay which is caused by very fast processes, is originated from the tip. The slow part of the decay belongs to nanocrystal photoluminescence. There is the point that the transition appears which is marked at the "gating point" in Fig. 5.6. Gating point is the time that the signal of the tip separates from the nanocrystal PL.

By histogramming all the photons with arrival times less than the gating point, the decay in Fig. 5.6b is obtained. This decay which belong to tip components is a representative of the fast processes inside the metallic antenna structure. Fig. 5.6c shows the result of histogramming of photons with arrival times longer than the gating point, which forms a slow decay (compared to tip component). This gating is necessary to be applied to the results obtained under two photon excitation. Although in Fig. 5.6 only the example of a decay is shown, this technique can be applied to the entire image. This is done while forming the image. Since the data acquisition has been done by TTR measurements which was described in section 3.2.3 arrival time of each photon is stored in the file. For time-gating, each photon that has arrival time of less than gating point (~ 2 ns for clean gating) is stored in the tip component matrix and photon with longer arrival times are stored for qdot component image. By this criterion two signals are easily separated and studies on both effects are feasible which will be described later. Similar type of gated-imaging has recently been applied for biological images studied by second-harmonic generation microscopy [87] for splitting second-harmonic signal from fluorescence signal.

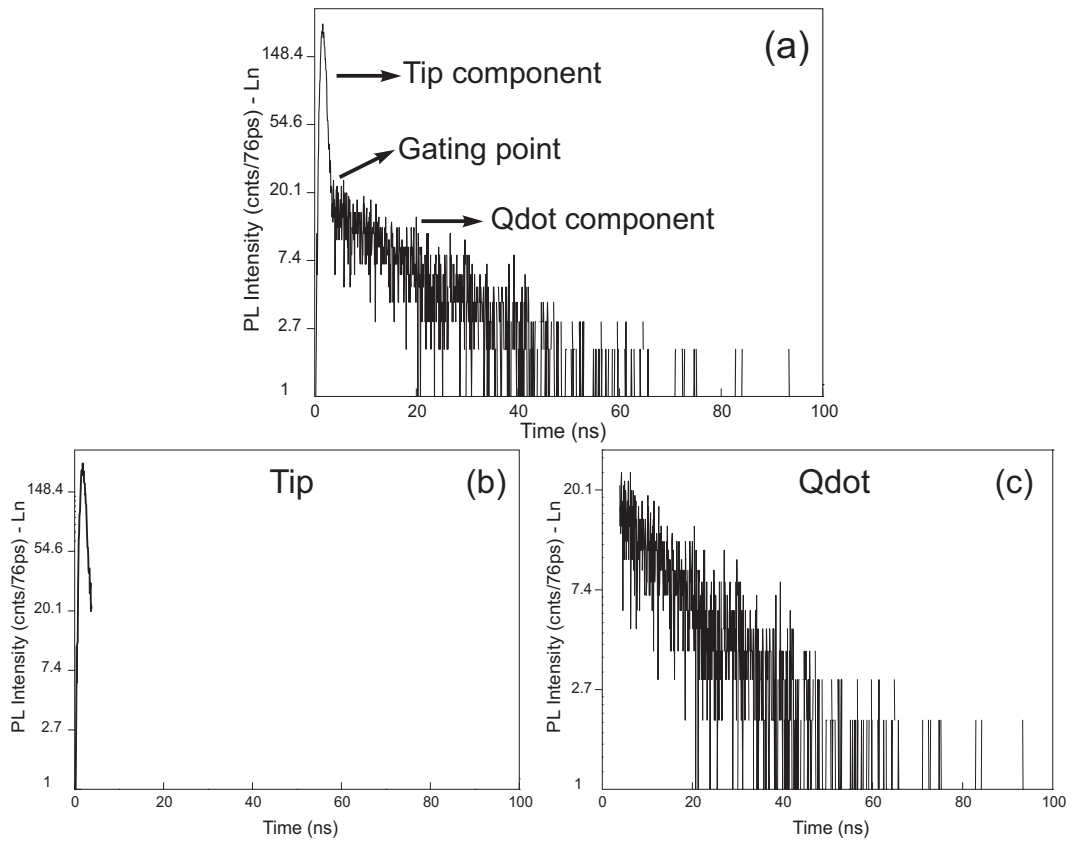


Figure 5.6: (a) Shows the decay of a qdot-tip system. The fast component is originated from the tip and the slow component is from the qdot. Gating point is around 2 ns where photon are separated from each other. (b) After gating, which shows the tip components with arrival times less than the gating point and (c) qdot component with arrival times longer than the gating point.

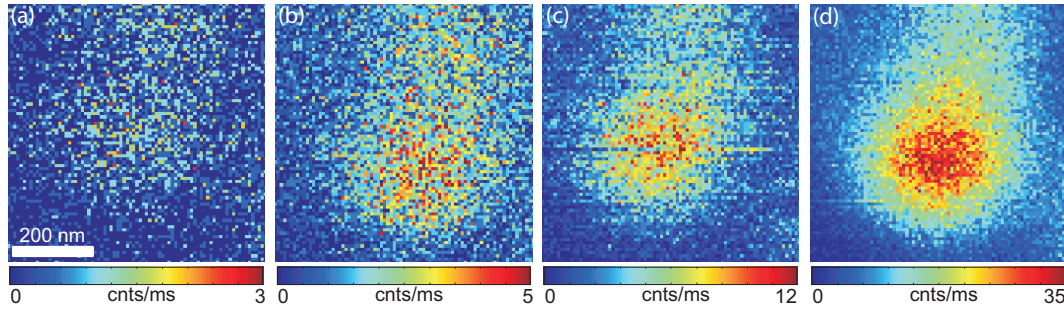


Figure 5.7: Light generated at the apex of the antenna tip under excitation with 100 fs laser with 830 nm wavelength with different powers. The detected photons are fast components (≤ 2 ns) in the scan images which are generated by the tip. (a) 20 μ W (b) 30 μ W (c) 43 μ W and (d) 60 μ W.

Antenna-Qdot Interactions under 2PE

Interaction of a bowtie nanoantenna with a single nanocrystal under 2PE is discussed here. An antenna tip with total length (L_T) of around 150 nm was used for this experiments, Fig. 4.5e&f. A nanocrystal was placed in the focus of the 830 nm femtosecond laser and the signal was improved by proper positioning the qdot inside the focus. PL intensity and lifetime of the nanocrystal were acquired as a function of the tip position. For data analysis, time-gated imaging as it was explained in the last part was applied to the data to separate the tip signal and the qdot signal. Figures 5.7a-d show the signal coming from the tip under different excitation powers (20, 30, 43 and 60 μ W, respectively). As can be seen this effect is highly non-linear with increasing the laser power, growth of the signal is much more enhanced. Power dependence of tip background was precisely quantified. For this purpose from each image shown in Fig. 5.7a-d, the pixels between maximum and 90% of maximum were averaged. Fig. 5.8 shows the power dependence obtained by this method. As plotted in log-log scale, (inset in Fig. 5.8) a slope of ~ 3 is calculated.

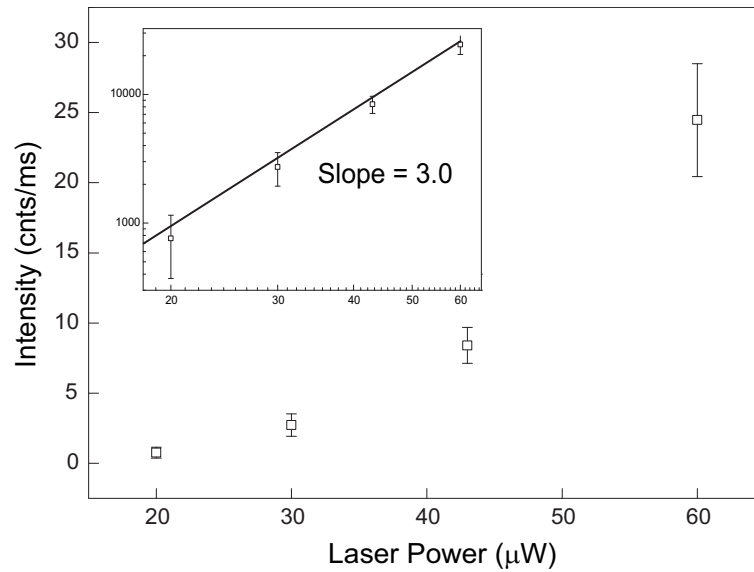


Figure 5.8: Dependence of the light generated by the tip on the laser intensity. Inset shows the log-log data with dashed fit curve of the slope of 3.

Based on these results the observed effect might be attributed to some orders of harmonic generation (e.g. third) [88] by the tip. However, since the optical detection window is centered between 560-600 nm it is not possible to detect photons at these frequencies. Another possibility would be some multi-photon processes in the metallic layer similar to what has been observed for gold [89]. This background could also be attributed to the light generated by the antenna at the tip apex [46].

Considering the qdot components which is the main focus of the experiments some similar effect compared to one-photon excitation (section 5.3.1) can be seen. Figure 5.9 shows PL intensity and the lifetime of the nanocrystal as a function of the tip position under two-photon excitation. Figures (a)-(d) are the intensity images and (e)-(h) are the lifetime maps. Each column is for one laser power from left to right 20, 30, 43 and 60 μW .

Figure 5.9(a-d) clearly show that under two-photon excitation, localized elec-

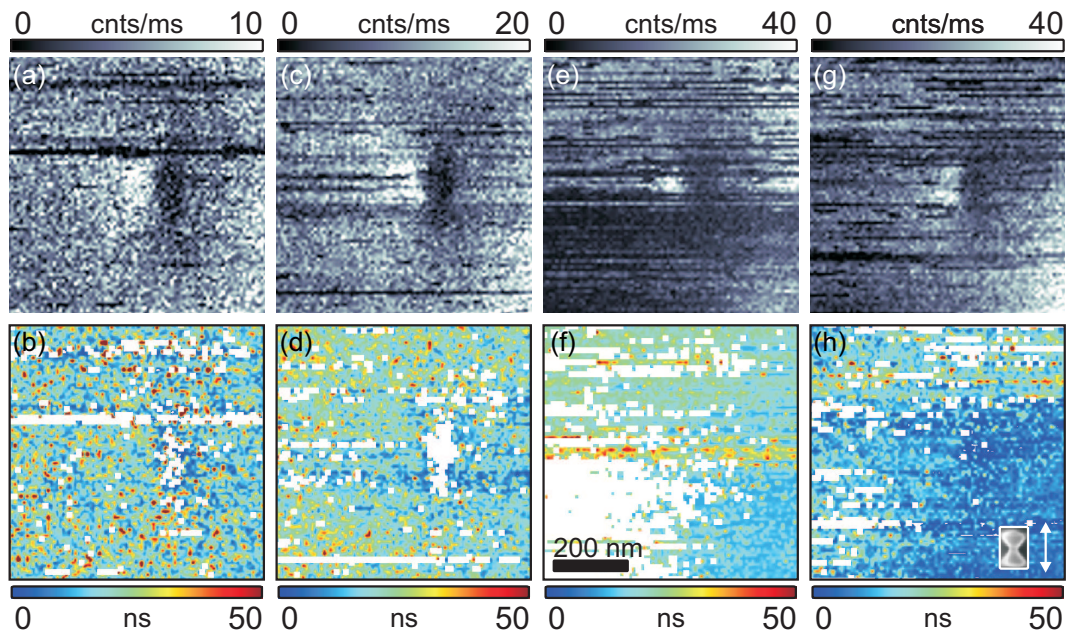


Figure 5.9: Quantum dot with respect to an antenna structure under 2PE by 100 fs laser with 830 nm wavelength. All images are as a function of the tip position. a-d are intensity and e-h are lifetime maps. Each column is for specific laser intensity. a&e: 20 μW , b&f: 30 μW , c&g: 43 μW and d&h: 60 μW . Tip orientation is shown in the bottom-right of (h) and the white arrow is the laser polarization.

tric fields in the feed gap of the antenna can overcome the quenching processes. In contact with the antenna qdot luminescence is more than the free nanocrystal. Another important point in figures 5.9a-d is the dependence of this effect to excitation power. With increasing the laser power from from 20 to 43 μW (a)-(c) PL intensity of the nanocrystal increase in contact with the tip. At 43 μW PL intensity if antenna/NC system saturates, therefore it stays at the same level even at higher laser powers, 60 μW . This is not the case for the free nanocrystal. When the tip is far from the nanocrystal, a gradual increase in the PL intensity is observed even beyond 60 μW .

To investigate this interaction in more detail, lifetime response should also be considered. Figures 5.9e-h show the lifetime maps of the qdot with respect to the distance from the tip. In some areas it is not possible to determine the lifetime due to lack of photons, this is shown as white pixels in the images. Considering these images, no considerable change in the lifetime data is observed in contact with the tip. In all cases lifetime of the free nanocrystal equals around 20 ns, and this stays the same in contact with the antenna. Therefore, according to these experiments bowtie antenna has no influence on the total decay rate of the nanocrystal. Meaning, sum of radiative rates and non-radiative rates stays the same in contact with the antenna. However, more PL intensity in contact with the antenna can be described by enhanced excitation of the nanocrystal in contact with the antenna feedgap. This is done by enlarging the absorption cross section of the nanocrystal by the antenna. Details of such analysis is presented in section6.1.

Chapter 6

Characteristics of "Antenna/NC" System

In chapter 4 it was shown that the bowtie antenna changes the emission properties of the nanocrystal. However, in experiments shown in chapter 4, only PL intensity and lifetime signatures of the nanocrystal were used to probe the interactions between nanocrystal and bowtie antenna. Since, nanocrystal in contact with the bowtie antenna is "*not quenched*" other interactions can be investigated. This is according to my knowledge the first time that different photophysical properties of a single emitter is investigated by the EM fields confined the region with some tens of nanometer (feedgap $\sim 40 - 80nm$). In this chapter absorption cross section, emission polarization and photon antibunching of the free NC as compared to antenna/NC is studied.

6.1 Absorption Cross Section

Absorption cross section is defined as the physical area, from which a quantum emitter can absorb photons [30]. Hence, such area is highly dependent on the physical size of the quantum emitter. Average radius for absorption cross section of single molecules is around 0.15 nm [9]. For quantum dot nano-crystals this area is bigger since their physical size is bigger. Based on power dependence measurements under 2PE, absorption cross section of nanocrystals is in the range of $4-36 \sim 10^{-37} \text{cm}^4 \text{s}$. In contact with antenna absorption cross section changes. In two-photon excitation experiments this is observed as enhanced excitation. The main goal in this section is understanding the alteration of two-photon absorption cross section in contact with the antenna tip.

6.1.1 Theory

For dilute dispersions of quantum dots extinction coefficient (which is a sum of absorption and scattering) of the dispersion can be calculated using the Beer's law [67] which is,

$$\epsilon_\lambda = \frac{A_\lambda}{cl} \quad (6.1)$$

Where, A_λ is wavelength dependent absorbance, c is the concentration of the fluorophores and " l " is the path length. Extinction coefficient ($\text{M}^{-1} \text{cm}^{-1}$) can be converted to absorption cross section (cm^2) using the following equation:

$$C_{abs} = \frac{2303 \cdot \epsilon_\lambda}{N_A} \quad (6.2)$$

where N_A is the avogadro's number. In contact with metallic structures ab-

sorption cross section undergoes drastic changes [85, 59]. In case of enhancement, antenna changes in the absorption cross section of the nanocrystal. This can be written as the following expression [90],

$$|\alpha|^2 \simeq \frac{\sigma^{(2)}}{\sigma_0^{(2)}} \quad (6.3)$$

$|\alpha|^2$ is the enhancement factor and $\sigma^{(2)}$ is the two-photon absorption cross section of the system in the presence of antenna and $\sigma_0^{(2)}$ is the two-photon absorption cross section of the free nanocrystal. Based on the equation 6.3 in the presence of the antenna absorption cross section is larger. Which means, antenna can collect the photons from the environment and feed them into the quantum system.

6.1.2 Results and Discussions

To study this effect in detail, power dependence of one specific nanocrystal in the free state and coupled to the antenna was acquired. From the intensity dependence of the emission of the emission and knowing the energy of the emitted photon as well as the collection efficiency of the set-up, absorption cross section can be determined. As it was explained in section 5.3.2 and Fig. 5.9 interaction of one single quantum dot in contact with an antenna under two photon excitation has been studied. Using the data points in figure 5.9(a)-(d) we can plot the power dependence of that specific quantum dot in the free state and in contact with the antenna. Data points for the free qdot were obtained where antenna is far ($> 2\mu m$) from the nanocrystal. And, data points for antenna/NC system were obtained where the enhancement point appears (antenna is on top of the qdot). The selected excitation powers are derived from the power dependence of qdots

under two photon excitation described in section 3.5.2. Saturation power for qdots under two photon excitation is around $80 \mu\text{W}$. Since the dependence under two photon excitation is quadratic, below $20 \mu\text{W}$ hardly any signal is observed. Therefore, the selected laser powers are, 20, 30, 43 and $60 \mu\text{W}$. Above $60 \mu\text{W}$ there is the risk of melting the tip under laser illumination, which has been observed for other tips. These four points are enough to obtain the knowledge about absorption cross section of the qdot in the free state and coupled to the antenna. Results are shown in figure 6.1. In Fig.6.1 (a), hollow-black rectangles are the data points for the free quantum dot and the solid-blue circles for antenna/NC system, as a function of the laser power. For antenna/NC, PL intensity is clearly higher than the free nanocrystal. PL intensity increases with laser power up to $43\mu\text{W}$. At this point, PL count rate of the antenna/NC system saturates. However, PL intensity of the free nanocrystal keeps increasing with power up to $60\mu\text{W}$. This is defined as enhanced excitation in which coupled chromophore saturates at lower laser powers [91]. Based on the increase in the PL intensity in contact with the antenna at $43\mu\text{W}$ laser power, enhancement factor can be written as,

$$|\alpha|^2 = 3.2 \tag{6.4}$$

Figure 6.1 (b) shows the first three data points of (a) which are below saturation in a log-log scale. Fitting a linear curve into both data sets results a slope of 2 which is clear proof of the two-photon processes that is happening for the chromophore system. Therefore, to calculate the absolute values of the two-photon absorption cross section, we can use the theory developed for quantum emitters under two-photon excitation [92] which has also been used for nanocrystals under

continuous wave lasers [72].

At low power (i.e. below saturation which coincides with the first three point in Fig. 6.1) power dependence of the quantum emitter under two photon excitation can be written as:

$$R = \frac{\xi\tau k_{rad}\sigma^{(2)}}{(h\nu)^2} I^2 \quad (6.5)$$

This equation is obtained for a two-level system in which, R is the emission rate of the system under two photon excitation, ξ is the collection efficiency of the optical set-up, τ is the lifetime of the excited state, k_{rad} is the radiative rates and $\sigma^{(2)}$ is the two-photon absorption cross section. $h\nu$ determines energy of the emitted photons and I is the laser intensity. Lifetime of the system is defined as $\tau = 1/(k_{rad} + k_{nrad})$. For semiconductor nanocrystals with unit quantum efficiency, non-radiative rates are close to zero [68], i.e. $\tau = 1/(k_{rad})$. Therefore, equation 6.5 can be re-written as,

$$R = \frac{\xi\sigma^{(2)}}{(h\nu)^2} I^2 \quad (6.6)$$

Assuming that:

$$A_{tot} = \frac{\xi\sigma^{(2)}}{(h\nu)^2} \quad (6.7)$$

We have:

$$R = A_{tot} I^2 \quad (6.8)$$

according to equation 6.8 with fitting a parabolic function to the data points in Fig. 6.1a, A_{tot} can be determined. And from that, we can calculate the

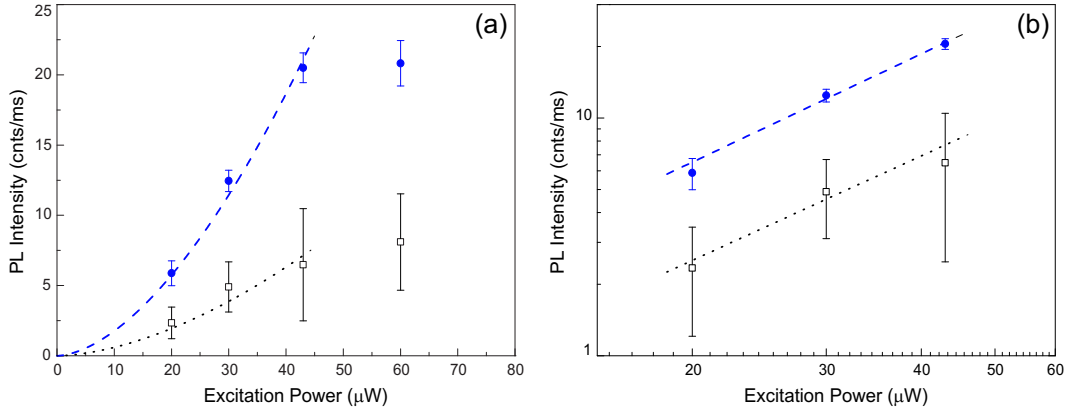


Figure 6.1: (a) Power dependence of free emitting quantum dot (hollow black rectangles) and the same quantum dot coupled to antenna (solid blue circles). Dotted black line and dashed blue line are parabolic fit to the first three points which representative of data below saturation. (b) The same in log-log scale, dotted black line and dashed blue lines are linear fit.

absorption cross sections of the free nanocrystal and in contact with the antenna.

In Fig. 6.1 dotted black line is the parabolic fit to the data of the free-emitting qdot and dashed blue line is for antenna coupled data points. A_{tot} obtained for both cases are, 0.035 ± 0.0012 for antenna/NC system and 0.011 ± 0.0013 for free nanocrystal. With knowing that energy of the emitted photon (585 nm) is $h\nu = 2.12 \text{ eV}$ ($3.4 \times 10^{-19} \text{ J}$) and collection efficiency of the set-up $\eta \simeq 2\%$, absolute number of absorption cross sections can be obtained,

$$\sigma_0^{(2)} = 6.3 \pm 0.75 \times 10^{-37} (\text{cm}^4 \text{s}) \quad (6.9)$$

and

$$\sigma^{(2)} = 20.2 \pm 0.69 \times 10^{-37} (\text{cm}^4 \text{s}) \quad (6.10)$$

By dividing the equation 6.10 to the equation 6.9 the influence of the antenna

on the absorption cross section is quantitatively determined. Therefore, we have,

$$|\alpha|^2 = \frac{\sigma}{\sigma_0} = 3.2 \pm 0.11 \quad (6.11)$$

This division precisely matches with the enhancement factor obtained in equation 6.4. This is a experimental and quantitative proof of the assumption made in equation 6.3 which has been used in many cases [93].

6.2 Emission Polarization

Transition dipole moment of single chromophores is an important characteristic which highly determines the luminescence behavior with respect to exciting light, including photoluminescence rate and lifetime [63]. An important question in the context of the current work is the influence of the antenna on the emission polarization of the nanocrystal. Bowtie antenna under laser illumination contain a strong dipole along the antenna. Interaction of this dipole with dipole of the nanocrystal can influence the emission polarization of the nanocrystal. In this section emission polarization of the free nanocrystal and antenna/NC system is studies using polarization microscopy.

6.2.1 Introduction and Theory

Most observation show that single fluorescent molecules posses a linear transition dipole [94] whose angle with respect to the polarization of the exciting light and dielectric interface determines the coupling strength. Several methods have been proposed for probing the orientation of the transition dipole moment of single molecules. Scanning near-field optical microscopy by spatially varying

the longitudinal and transverse field components can give information about 3D orientation of the transition dipole in single molecules [95, 96]. In far-field optical microscopy, annular illumination approach by enhancing the longitudinal field components have mapped out the orientation of the transition dipole [65]. De-focused imaging [97] and direct imaging of the emission pattern [98] have also been used for probing the transition dipole orientation. In far-field techniques polarization microscopy is used for determining the orientation of excitation and transition dipole moments in single molecules, it can only provide 2D information [99, 100, 101], about the orientation of the transition dipole.

In case of single emitters with a "bright axis" transition dipole, the transition strength is proportional to $|\hat{\mu} \cdot \hat{E}|^2$, where $\hat{\mu}$ is the transition dipole vector and \hat{E} is unit electric field vector for absorbed or emitted light [102]. Consequently, the intensity of the detected signal is proportional to $\cos^2(\theta)\cos^2(\phi)$, in which θ is the angle between the emission polarization and projection of μ on the sample plane, and ϕ is the tilt angle between μ and the sample plane (in other words the out-of-plane angle). In this case, rotating a polarizer in the emission pathway will modulate the signal between $I_{min} = 0$ and $I_{max} = |\mu|^2 \cdot \cos^2(\phi)$. Result of such modulation is %100 polarized emission through which the in-plane angle (θ) can be determined.

Although transition dipole in single molecules is highly linear, in case of semiconductor nanocrystals the situation is totally different [17]. The transition dipole in CdSe quantum dots is determined by unidirectional hexagonal Wurtzite crystal structure and the prolate shape of the nano-crystallite as well as the electron-hole interaction [103]. As a result, band edge states of the CdSe nanocrystal, is split into 5 states, of which 3 are optically active and 2 are optically in-active. Each of these active states can have its own transition dipole [104]. The first optically

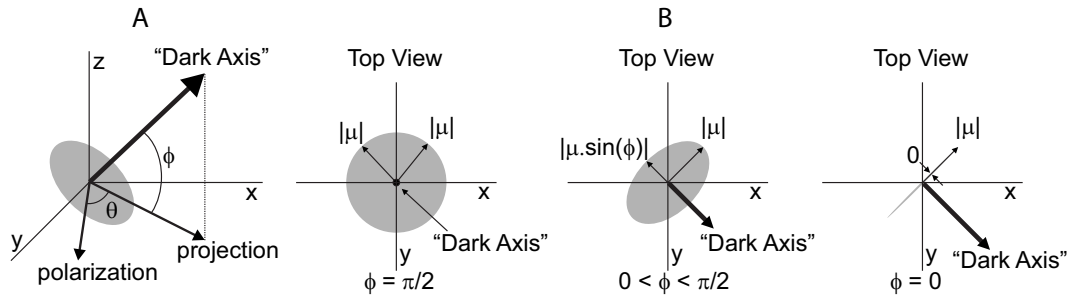


Figure 6.2: Schematic illustration of the "dark axis" orientation in a quantum dot with light propagation along the z axis and xy as the sample plane. (A) is 3D picture, shaded disk is the degenerate dipole moment oriented normal to the dark axis. (B) Top views which show the projection of the dark axis onto the sample plane (x - y) in three different cases for ϕ . Each case corresponds to a specific modulation in emission polarization.

active state is similar to single molecules with a bright axis oriented parallel to the hexagonal c -axis. Transitions involved this state should have polarization dependence similar to single molecules with %100 complete modulation. The other two optically-active states have a doubly degenerate two-dimensional transition dipole oriented isotropically in the xy plane of the hexagonal structure [17]. In this case what remains is a unidirectional "dark axis" along which no light is emitted. While the orientation of the transition dipoles are known, theoretical and experimental investigations have not yet determined which if these states contributes to recombination to the lowest excited state. Overlapping these states while excited simultaneously can decrease the degree of polarization. This is in contrary to CdSe quantum rods which have highly linear transition dipole in absorption [105] and emission [106], which shows the importance of the aspect ratio in emission polarization of CdSe crystals.

Fig. 6.2 schematically shows the orientation of the dark axis in a quantum dot while light is propagating along the z axis. ϕ is the out-of-plane angle between the dark axis and the sample plane (here shown as xy) and θ is the angle

between the emission polarization and projection of the dark axis on the sample plane. In Fig. 6.2, **A** is the 3D picture. Schematic pictures in **B** are top views for three different cases. First, when the dark axis is perpendicular to the sample plane ($\phi = \pi/2$). second, dark axis has an angle between the sample plane and its normal ($0 < \phi < \pi/2$) and third, dark axis is in the sample plane ($\phi = 0$). Transition strength of such a "dark axis" is proportional to $(1-\cos^2(\theta)\cos^2(\phi))$. Once an analyzer is rotated in the emission pathway intensity will modulate between $I_{min} = |\mu|^2$ and $I_{max} = |\mu|^2 \cdot \sin^2(\phi)$ [107]. Based on these theories ϕ and θ can be directly measured using polarization microscopy, as well as the absolute value of the transition dipole ($|\mu|^2$) since it equals the I_{max} . For a situation that ϕ is $\pi/2$ no intensity modulation is expected and when $\phi = 0$ the result is complete modulation. According to high-resolution transmission electron microscopy (HRTEM) studies these two situation corresponds to positions that nanocrystal is sitting on the sample plane [108]. Energetically it is more favorable for quantum dot to be on the surface lying on the larger surface ($\phi = 0$) to decrease the surface energy. But since the aspect ratio of colloidal nanocrystals is only around 1.1-1.2 [109, 110] the other case ($\phi = \pi/2$) is not impossible. The third case is when nanocrystal stands on the surface with c -axis oriented between the sample plane and its normal. In this case depending on the out-of-plane-angle modulation will have a specific depth. Depth of modulation (MD) will determine the polarization degree (PD) of each nanocrystal followed by equation 6.12. Consequently, through polarization microscopy four values of a single nanocrystal can be obtained, ϕ (out-of-plane angle of the dark axis), θ (in-plane angle of the dark axis), $|\mu|^2$ (absolute value of the transition dipole moment) and PD (polarization degree of the emission).

$$PD = \frac{I_{max} - I_{min}}{I_{max}} \quad (6.12)$$

6.2.2 Results and Discussions

Emission polarization of single nanocrystals was studied by detecting emission intensity while a linear polarizer (analyzer) is turning in the emission pathway. Although this method has already been used successfully for studies on nanocrystal emission polarization [107], here an APD was used for detection system, similar to the reference [108]. The main problem of such a detection arises from the small size of the active area on APD which introduces an artificial modulation every 180 degree of the analyzer. The procedure taken for data correction of emission polarization is described in appendix A. To verify that the experimental set-up has no intrinsic polarization dependence un-polarized light from lamp was sent into the detection set-up via objective. Un-polarized light after passing through the turning analyzer was detected by APD. No modulation was observed (except the modulation described in appendix A caused by moving the focus on the APD) which is a clear proof that set-up has no other artifact. In another step to characterize the set-up polarization dependence, DiI molecules were studied by the same technique. Results showed a complete modulation due to their "bright axis" which introduces a linear dipole moment.

In order to measure the emission polarization of nanocrystals, one nanocrystal was immobilized in the laser focus and its emission intensity was acquired while an analyzer is turning in the detection path. Fig. 6.3 shows the polarization modulation of two different quantum dots on the sample as a function of the analyzer angle, where zero angle corresponds to the laser polarization direction. In Fig. 6.3 two different cases of quantum dots can be observed. For qdot1 the

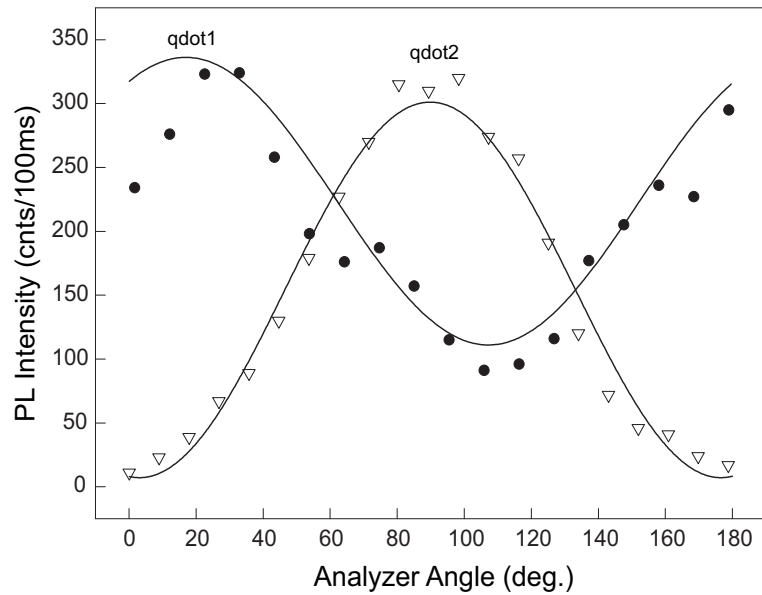


Figure 6.3: Emission intensity of two different nano-crystallites as a function of the analyzer angle. Solid lines are fit the sine-squared function of analyzer angle, which has a period of 180 degree.

modulation is not complete which means that dark axis of this quantum dot is oriented with an angle between 0 and 90 with respect to the sample plane. For qdot2 modulation is complete which is a sign of quantum dot having its dark axis on the sample plane. In Fig. 6.3, maximum point for qdot1 appears after 10 degree and for qdot2 after 80 degree. These angles are the angles between the projection of the dark axis on the sample plane with respect to the emission polarization, which is in this case the same as the laser polarization.

In order to study the influence of the antenna on the emission polarization of the nanocrystals, experiments similar to section 5.3.1 were performed. One quantum dot was immobilized inside the laser focus under one-photon excitation and antenna tip scans around the focal area. Figs. 6.4(a&b) show the photoluminescence and lifetime maps of quantum dot as a function of the tip position. Enhancement factor in Fig. 6.4 is not high, therefore coupling between antenna

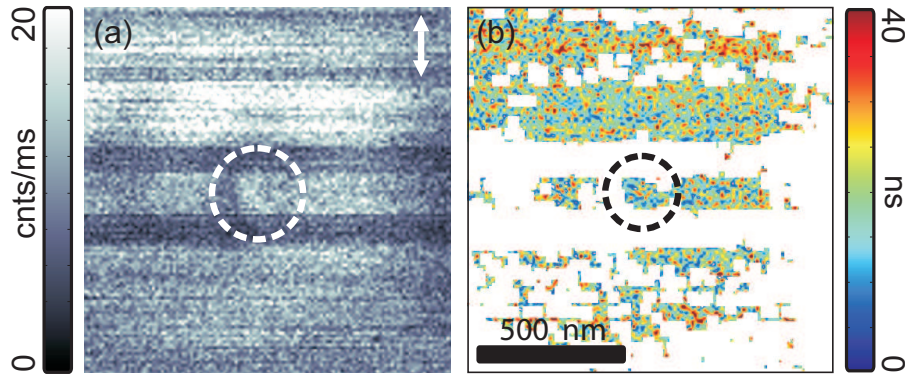


Figure 6.4: (a) & (b) PL rate and lifetime maps of NC as a function of the antenna-tip position. Dashed circles in both show the interaction area and where the antenna-tip is positioned for data shown in Fig. 6.5.

and nanocrystal is not very strong. Analyzing the lifetime response, it can be seen that under the influence of the antenna-tip lifetime is slightly shorter. Since nanocrystal in contact with the antenna is not quenched, emission polarization of the antenna/NC system can be compared with free nanocrystal.

Figure 6.5(a) shows the emission intensity of the free nanocrystal as a function of the analyzer angle. Sin-squared fit (black line) reveals the maximum and minimum intensities and the angle that they take place. Details of the information obtained from Fig. 6.5 is presented in table 6.1. As it can be seen this nanocrystal is oriented with its dark axis 40 degree out-of-plane with polarization degree of 0.58. Angular distance between the "dark axis" projection on the sample plane and emission polarization in this case is 83 degree, while its projection has absolute value of 470. In Fig. 6.5(b) the same data as (a) is shown in polar format in which direction of long axis of sine-squared fit shows direction of maximum. In other words angular distance between the dark axis projection of the sample plane and emission polarization. It should be taken into account that laser polarization is at zero degree which clearly shows that observed effect is an intrinsic behavior

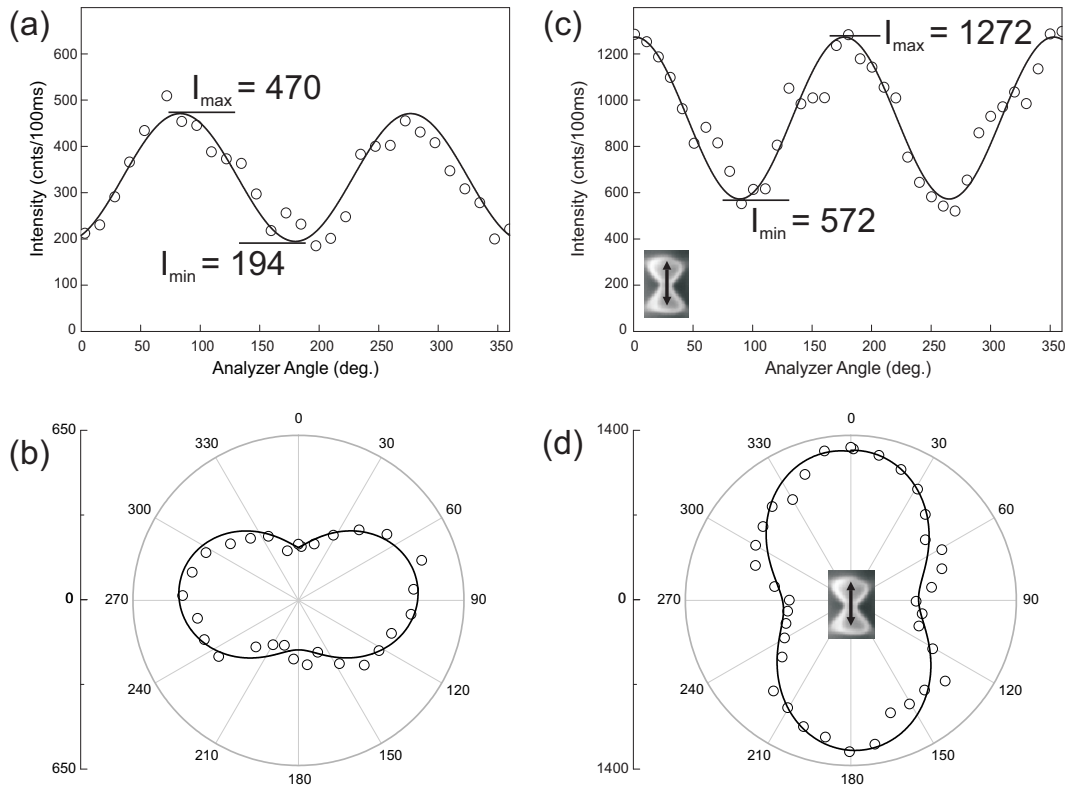


Figure 6.5: (a) PL intensity of the free NC as a function of the analyzer angle while laser polarization and antenna orientation are at zero angle. (b) The same as (a) in polar format. (c) PL rate of the same NC as a function of the analyzer angle while the antenna is placed on the top of nanocrystal. (d) The same as (c) in polar format. Overlay of the tip image in (d) shows the orientation of the antenna with respect to analyzer angle and NC emission.

Table 6.1: Emission polarization data of free NC and antenna-coupled NC

EP Data	Free NC	Antenna-coupled NC
ϕ (degree)	40	42
θ (degree)	83	~ 0
$ \mu ^2$	470	1272
PD^a	0.58	0.55
MD^b	276	700

$$^a \text{ PD: Polarization Degree} = (I_{max} - I_{min})/I_{max}$$

$$^b \text{ MD: Modulation Depth} = I_{max} - I_{min}$$

of the nanocrystal.

In Fig. 6.4(a&b) the interaction area of the nanocrystal and antenna is circled. Center of the circle is equivalent to the position of the nanocrystal. With positioning the tip on the top of nanocrystal (center of the circle) similar data as shown in 6.5(a&b) can be acquired. Fig. 6.5(c) shows the PL rate of nanocrystal as a function of the analyzer angle while the antenna tip is placed on the top of NC (i.e. emission polarization of the superemitter). Comparing to free nanocrystal, although polarization degree and out-of-plane angle remain the same (table 6.1) but in plane angle and absolute value of transition dipole undergo drastic changes. In-plane angle has completely turned towards zero which corresponds to the orientation of the antenna. Figure 6.5d with image of the tip as an overlay clearly displays this correspondence. Another important change of the NC system in contact with the antenna is I_{max} or in other words absolute value of the projection of the transition dipole on the sample plane $|\mu|^2$ by a factor of almost three. Change in the value of the transition dipole moment coincides with the phase shift of the in-plane angle of transition dipole. This shows that absolute value of the transition dipole in contact with the antenna is larger than the free nanocrystal. Thus, coupling to the antenna enlarges the transition dipole of the nanocrystal and shifts it towards the orientation of the EM field inside the an-

tenna feedgap. This result associated with enlarging the absorption cross section of the NC system in contact with the antenna (section 6.1) is a clear proof of dipole-dipole coupling which occurs between the nanocrystal and antenna system. Therefore, NC coupled to the antenna system a more emissive dipole which is the specification of the "superemitter". This proves that NC/Antenna system acts as a powerful dipole which radiates along the antenna length and its size is determined by the coupling between the nanocrystal and the antenna.

In summary, antenna/NC system "superemitter" has specific emission polarization which is elongated along the length of the antenna. Size of the transition dipole is determined by coupling strength inside the superemitter.

6.3 Photon Anti-Bunching

Photon antibunching of a quantum system is a measure of the tendency of that system to emit one (and only one) photon at a time. This means, once a two-level system is excited recombination process generates one photon and no other photon can be emitted immediately. In order to generate another photon a new excitation-recombination cycle is required [111]. Based on this definition, a two-level system acts as a single photon source, i.e. "photon gun". Single emitters based on their electronic structure show this response (antibunching) under illumination. Time distance between two successive single photons generated from the single emitter depends on the lifetime of the excited-state. Therefore, if an external object changes the lifetime by resonant coupling, it will definitely influence the antibunching behavior. As it was explained in section 5.3.1, under one-photon excitation lifetime of the nanocrystal fluorescence reduces in contact with the antenna. Therefore, it would be interesting to study the antibunch-

ing response of the nanocrystal while in contact with the feedgap of the bowtie nanoantenna. In the experiments presented in this section, it will be shown that antenna/NC system is a more efficient single photon source as compared to a free nanocrystal.

6.3.1 Introduction

Second order correlation function 6.13 describes the probability of detecting a photon at time t and another one at time $t+\tau$ [11] and is defined as the following,

$$g^{(2)}(\tau) = \frac{\langle I(t)I(t+\tau) \rangle}{\langle I(t) \rangle^2} \quad (6.13)$$

A histogram of the time-intervals between the consecutive photons gives the distribution of each pair of photons. Second-order correlation function describes the distribution of all pairs of photons. A simple way to study anti-bunching behavior is the technique which was introduced by Hanbury-Brown & Twiss in 1956 [112]. This method is based on non-polarized beam splitter in the detection pathway. Two detectors are used to detect the photon arriving from the beam-splitter. One of the detectors serves as the starting point and the other acts as the stop and the time interval between the start and stop is measured. With histogramming the inter-photon times (or, time delay between two successive photons) coincidences of each photon pair can be studied. For perfectly antibunched light coincidence of two photons with zero delay time is zero. In other words,

$$g^{(2)}(0) = 0 \quad (6.14)$$

A physical system with such characteristic can act as a single photon source

which can be widely used in quantum information processing [113] and quantum cryptography [114, 115]. Several systems have been studied which can deliver single photons on demand [116], including atoms [117], ions [118] and nitrogen vacancy centers [119]. Single photon generation has also been observed from single dye molecules at low temperatures [120] as well as ambient environments [76, 121].

MBE grown semi-conductor quantum dots are another sources for single photons [122, 123]. Although anti-bunching has been observed in MBE grown quantum dots from different compounds [124] on different substrates [125] but their antibunching behavior changes by temperature. Increasing the temperature from 4 K promotes the multi-photon emission which decreases the probability to generate single photon [126].

Photon antibunching have also been observed from colloidal semiconductor nanocrystals under continuous wave (CW) [127, 128] and pulsed excitation [129]. Colloidal quantum dots are known to be stable single photon sources since their quantum yield is very close to unity. Moreover, stability of quantum dots (i.e. photobleaching time) is much longer than single molecules. The main advantage of colloidal quantum dots in this respect is that they can still emit single photons at room temperatures. Fig. 6.6 shows an antibunching curve of a single nanocrystal under pulsed excitation. Laser intensity in this measurement was kept far less than the saturation intensity. As it can be seen the peak at zero is missing which confirms there can be no second photon emitted at small time-intervals. In order to emit another photon from this qdot, the system must be excited by another laser pulse. All the peaks here are separated by 200 ns which is related to the repetition rate of the laser (5 MHz). Gray line is the fit to the data yielding a lifetime of 22 ± 1 ns for this qdot. Details of the exponential fits

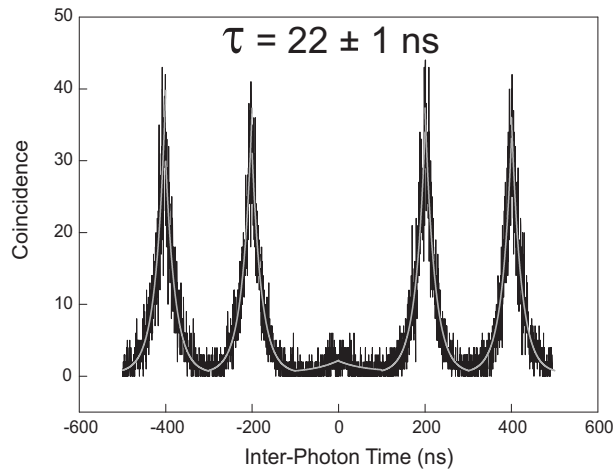


Figure 6.6: Histogram of inter-photon times of a single nano-crystal under pulsed excitation. The gray line is exponential fit to the data giving a lifetime of around 22 ns.

to the anti-bunching results is explained in appendix B.

Although colloidal quantum dots known as artificial atoms emit single photon similar to atoms and single molecules (as described earlier). The main difference between nanocrystals and atoms, single molecules and even bulk semiconductors is that nano-meter sized nanocrystals can have multi-exciton. In a nanocrystal several excitons can occupy a volume smaller than the bulk excitons. This is known to be due to "squeezed" excitonic states in nanocrystals [130]. The observation of antibunching in nanocrystals (fig. 6.6) confirms that multi-exciton should emit non-radiatively. Otherwise, the chance to produce more than one photon per excitation pulse would have been much higher. In other words, in Fig. 6.6 a strong peak at zero would have been observed as other peaks. A possible way of electron-hole recombination in a non-radiative way are Auger processes. In which, non-radiative recombination of electron-hole produces electron instead of photon (in radiative recombination). In an Auger picture, recombination of electron-hole pairs leads to energy transfer to a third particle (electron or hole)

which is re-excited to a higher energy state. In semiconductor nanocrystals a ground state bi-exciton decays to into an excited state mono-exciton which will then decay non-radiatively in a very short time scale in the order of pico-second [131]. Both experimental observations [132] and pseudo-potential many body calculations [133] confirms the presence of Auger transitions in competition with radiative de-population of excited states which quench the photoluminescence intensity.

Although colloidal quantum dots perform anti-bunching behavior there is one major restriction for them to be used as a single photon source. The main drawback in emission of nano-crystals is the "On" and "Off" periods known as fluorescence intermittency [134]. Possible explanation for blinking behavior is the Auger recombination [135]. In this picture relaxation of a bi-excitonic state (two pairs of $e-h$) ejects one carrier from the quantum dot which leads to autoionization of the nanocrystal. This process is non-radiative which causes the "off" period in the photoluminescence. Based on this scheme the duration of "on" periods depends highly on the excitation intensity, nanocrystal radius and excitation frequency. Recent Monte Carlo simulations [136] and experimental observation [137, 138] shows that at low laser intensities Auger processes are negligible and "on"- "off" blinking is mainly dominated by carrier trapping at surface or interfaces via direct tunneling. Therefore, it can be understood that nanocrystal environment plays a very important role in their fluorescence intermittency [139]. Based on this picture surface passivation of colloidal nanocrystals is the key to suppress their blinking behavior. This method has been tried by molecules containing Thiol groups (e.g. β -mercaptoethanol) [140]. Surrounding the nanocrystal environment with this molecule leads to almost complete suppression of the "on"- "off" behavior.

6.3.2 Theory

For a *theoretical* consideration of the single photon generation by a *two-level system* we assume a single dipole under *pulsed excitation*. The two level system (see Fig. 3.13) is with unit quantum efficiency and illuminated by a train of laser pulses with duration of d (pulse duration) and temporal separation of T (i.e. repetition rate of $1/T$). Level populations can be written as the following:

$$\dot{p}_2 = k_{12}p_1 - k_{21}p_2 \quad (6.15)$$

$$\dot{p}_1 = -k_{12}p_1 \quad (6.16)$$

Solution of level $|2\rangle$ populations at time t with starting from level $|1\rangle$ at time t_0 for times smaller than the pulse duration, $t \leq d$, is:

$$p_1(t, t_0) = \exp[-k_{12}(t - t_0)] \quad (6.17)$$

$$p_2(t, t_0) = \frac{k_{12}}{k_{12} - k_{21}} (\exp[-k_{21}(t - t_0)] - \exp[-k_{12}(t - t_0)]) \quad (6.18)$$

and, for times longer than the pulse duration, $t \geq d$ is,

$$p_1(t, t_0) = p_1(d, t_0) \quad (6.19)$$

$$p_2(t, t_0) = \exp[-k_{21}(t - d)]p_2(d, t_0) \quad (6.20)$$

The probability to emit at least one photon between two pulses in the interval

$[0, T]$, P_e is then:

$$P_e = k_{21} \int_0^T p_2(t, 0) dt \quad (6.21)$$

$$P_e = 1 - \exp(-k_{12}d) - \frac{k_{12}}{k_{12} - k_{21}} \exp(-k_{21}T) \times [1 - \exp((k_{21} - k_{12})d)] \quad (6.22)$$

Since T has to be much larger than compared to the lifetime of the excited state ($\tau = 1/k_{21}$) equation 6.22 can be simplified to the following:

$$P_e \approx 1 - \exp(-k_{12}d) \quad (6.23)$$

Thus the probability to emit exactly n photons is given by:

$$P_n = \sum_a p_a^{(n)}(T, 0) = \int_0^T dt \left\{ 1 - k_{21} \int_t^T p_2^{(0)}(t', t) dt' \right\} \times k_{21} p_2^{(n-1)}(t, 0) \quad (6.24)$$

Equation 6.24 corresponds to the probability to emit photon n at time t and no photons within $[t, T]$. In the limit, $\exp(-k_{21}T) \rightarrow 0$, the probability P_1 is given by the following expression:

$$P_1 = \left(\frac{k_{12}}{k_{12} - k_{21}} \right)^2 [\exp(-k_{21}d)] - \left(\frac{k_{12}k_{21}d}{k_{12} - k_{21}} \right) [\exp(-k_{12}d)] \quad (6.25)$$

Equation 6.25 describes the exponential population and depopulation of the excited and ground states of the two level system under pulsed excitation with unit quantum efficiency (which is almost the case for semiconductor nanocrys-

tals). Processes taking place in a system with non-perfect quantum efficiency and three level system is explained elsewhere [141]. As can be seen in equation 6.25 limiting factors in single photon generations are the excitation (k_{12}) and re-combination rate (k_{21}), which cause a "dead time" between two successive photons. In experiments presented here, a bowtie nanoantenna will be used to reduce this dead times in the photon streams.

6.3.3 Results and Discussions

In the context of current research it is expected that interaction between antenna and nanocrystal will change the photon correlation function of the nanocrystal. In chapter 5 it was explained that positioning the antenna feedgap on the top of quantum dot promotes the radiative rates by coupling between antennas and nanocrystal. Slightly de-tuning the antenna position and placing the antenna arm on the nanocrystal will promote the non-radiative rates with energy transfer to the metal. This causes quenching the fluorescence and hence generating no photon by the nanocrystal. In order to study the influence of the antenna on the photon antibunching behavior of nanocrystal, experiments similar to section 5.3.1 under one photon excitation is done. The reason that one photon excitation is selected as excitation scheme is that the change in the lifetime (shortening) was only observed under 1PE. Under two photon excitation as it was explained earlier large energy mismatch between the excitation and emission frequency leads to enhanced excitation and not enhanced emission. A single nanocrystal was immobilized inside the laser focus and antenna tip (figure 4.5) scanned around the focal area. PL intensity and lifetime of the nanocrystal were simultaneously acquired. The result is shown in figure 6.7. As it can be seen in the intensity image (a), antenna feedgap has promoted the emission. This area has been circled

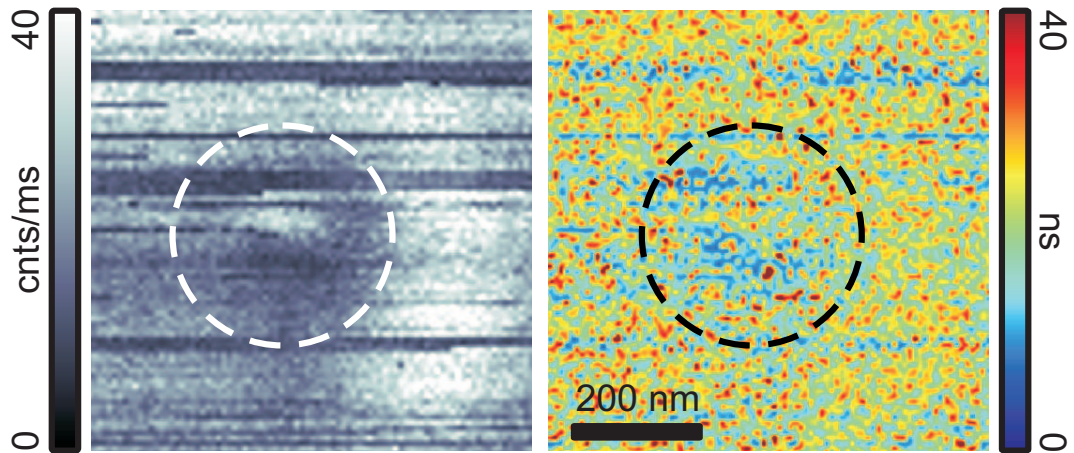


Figure 6.7: PL intensity (a) and lifetime (b) maps of the nanocrystal as function of the antenna-tip position. Experiments were performed under one photon excitation with high laser intensity around 700 nW.

for emphasis. On the top and bottom of the enhanced point there are quenched areas caused by the arms of the antenna. Looking at the lifetime response of the nanocrystal to the antenna (Fig. 6.7b) it can be seen that lifetime of the interaction area (circled) is shorter than the free quantum dot by almost a factor of 2 (from around 20 ns to 10 ns). In this experiments a laser intensity of ~ 700 nW was used in order to observe the antenna effect. This is a relatively high laser power which is close to the saturation level of the nanocrystals under one-photon excitation.

In the next step, photon antibunching of the nanocrystal of the free nanocrystal and in contact with the bowtie antenna was acquired. For this purpose non-polarizing beam splitter was placed in front of the detector and a second avalanche photodiode was used as the stop pulse provider in TTTR data acquisition (section 3.2.2). When a photon hits the first APD measurement starts until a second photon hits the second APD which gives the stop signal. With histogramming the inter-photon times (time intervals between start and stop signal), photon co-

incidences can be obtained. A delay line added to the stop pulse was 800 ns in order to see the equal number of pulses around zero. First tip was positioned far away from the nanocrystal and photon correlation was acquired which is shown in Fig. 6.8 (a). The dip at zero delay confirms the anti-bunching response and that nanocrystal system is producing one photon at a time. The small peak observed at zero can also be attributed to biexcitonic emission caused by high intensity laser [142]. Antenna-tip is then positioned on the top of the nanocrystal which means on the bright area in Fig.6.7. Another photon correlation data was acquired from the nanocrystal coupled to the antenna which is shown in figure 6.8(b).

Comparing the figures 6.8 (a) and (b) a very clear difference in the photon correlation is observed. Although free nanocrystal acts as a single photon source with lifetime of 21 ns lifetime is reduced to around 10 ns in contact with the antenna. Nanocrystal system is still emitting single photon per excitation pulse even in contact with the antenna. A more important effect is that tip has reduced the lifetime by promoting the radiative rates (k_r). This means, the cycles of excitation-deexcitation are done faster in the contact with the antenna. This is a very important property for a single photon source. Because, between the first excitation-emission there is a "deadtime" for the single photon source. This "deadtime" is a period that nanocrystal needs to be re-excited and re-combined again for the generation of the next photon. In contact with the antenna this "deadtime" is half shorter which makes the quantum emitter a faster system for single photon generation. Another important feature of the antibunching response of the antenna/NC system is the larger peak at zero delay. Assuming that the zero peak for the free nanocrystal is caused by multi-excitonic emission from the nanocrystal under high laser intensities [143], these processes have

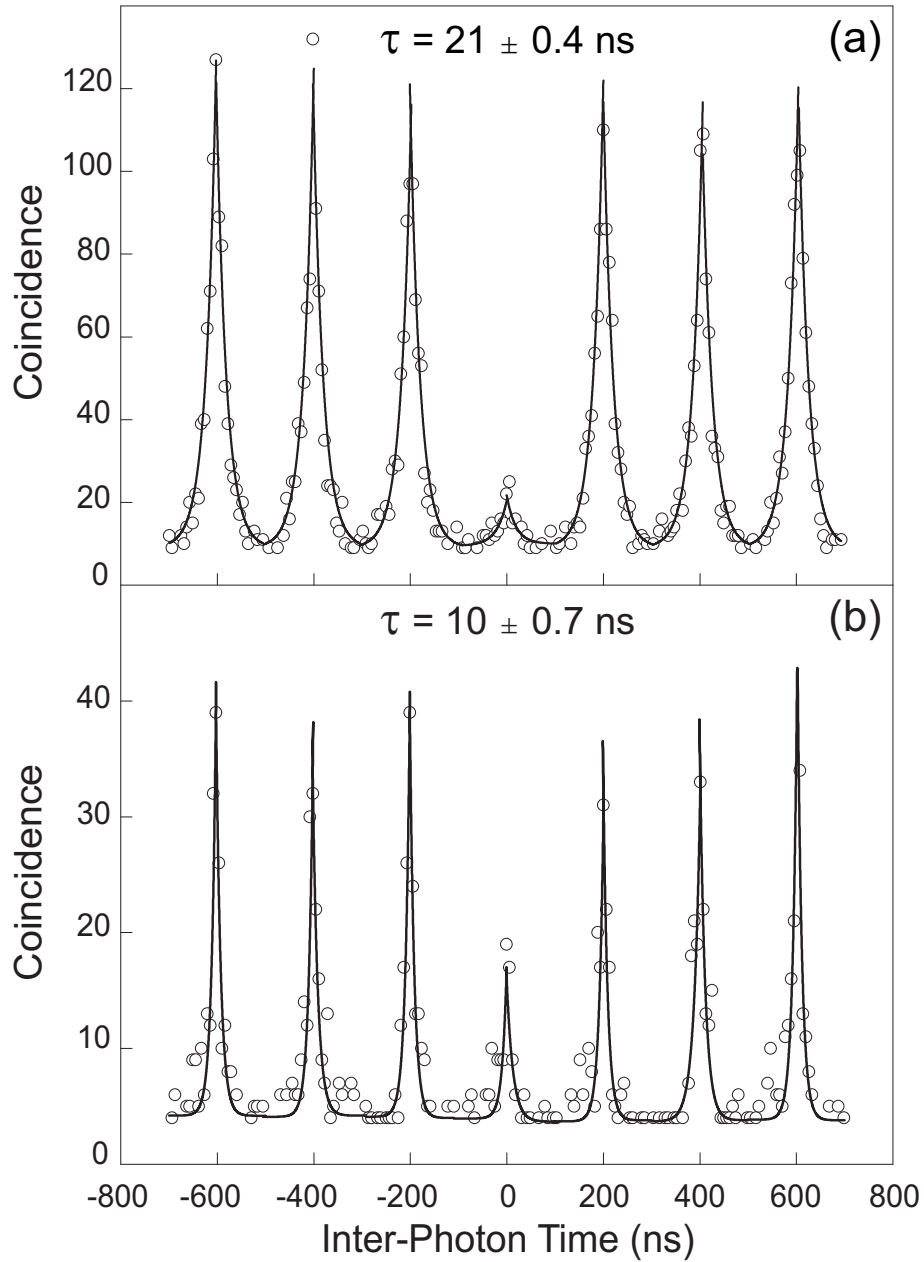


Figure 6.8: Photon coincidence counts of CdSe nanocrystal in the free emitting state with lifetime of 22 ± 0.4 ns (a) and coupled to antenna feedgap with lifetime of 10 ± 0.7 ns (b). Laser power 700 nW

been promoted in contact with the antenna. However, more detail studies need spectroscopic investigations on the antenna/NC system under high laser powers. Assuming the quantum dot as an artificial atom the observed effect can be *compared* with Purcell effect [144] where radiative properties of a quantum emitter is modified by resonant coupling to cavity modes. This result (Fig. 6.8) implies that "superemitter" [50] which is formed by resonant coupling of a single emitter to an antenna can be another way of modifying the emission properties of quantum emitters. And it is highly in competition with optical modes in a microcavity based on a microdisk [145] or a photonic crystal defect cavity modes [146]. This opens the way for quantum dots coupled to bowtie nanoantennas, that in strong coupling regimes can be used for cavity-quantum electrodynamics (C-QED) [147].

In summary, coupling of quantum dots to the bowtie nanoantenna promotes the radiative rates. "Superemitter" which is the result of this efficient coupling is still a single photon emitter since each photon is still generated via successive excitation-emission cycles. Unless, the cycles are done faster compared to free quantum dot (Fig. 6.8). Since radiation properties of the superemitter is highly determined by the spatial position of the gap and quantum emitter. Slightly mispositioning the antenna with respect to the quantum dot it can lead to quenching and no more single photon is generated.

Chapter 7

High-Resolution Optical Microscopy

7.1 Introduction

The main goal of scanning near-field optical microscopy (SNOM) is to extend the spatial resolution of optical microscopy beyond the diffraction limit [8, 148, 149] defined by Abbe around $\sim \lambda/2$. Introduction of aperture probes [150] has allowed fluorescence imaging with sub-diffraction resolution as well as determining the orientation of the dipole moment of fluorescent molecules [95]. Since then SNOM has attracted interests in many disciplines such as materials science, chemistry and biology [151, 152]. Aperture probes are based on aluminum coated fiber tips with un-coated foremost end of the fiber, which acts as the aperture [153]. This approach highly suffers from the low light through-put in the fiber which can be on the order of 10^{-4} for a 100 nm aperture. Resolution determined by aperture technique has been down to 30-50 nm which can be highly falsified by artifacts [154].

Aperture-less near-field optical microscope was introduced first to overcome the light through-put problem [155, 156]. In this method, the tip is illuminated from the side and locally perturbs the field at the sample surface [157]. A major advantage of this approach is the possibility to study non-transparent samples. In the perturbing tip approach which is also known as scattering-type scanning near-field optical microscopy (SNOM) [158] with exploiting surface plasmons resolution down to 3 nm [159] or even 10 angstrom with interferometric measurements while tip position is modulated [160] have been reported.

Another category of apertureless techniques are based on tip-enhanced microscopy [161, 162, 163]. These measurements are based on metallic tips in the focus of a femtosecond pulsed laser. Enhancement originates from a combination of the electrostatic **lightning-rod effect** [164] which is due to geometric singularity of sharply pointed structures, and localized surface plasmon resonances which highly depend on excitation wavelength. Excitation light drives the free electrons in the metal along the direction of polarization. While the charge density is zero inside the metal, charge accumulates on the surface of the metal. With light polarization perpendicular to the tip axis, diametrically opposed points on the tip surface have opposite charges. Consequently, tip apex remains uncharged and no field enhancement is achieved. On the other hand, when laser is polarized along the tip axis, induced surface charge density is rotationally symmetric and has the highest amplitude at the end of the tip and is highly confined to the tip apex. Enhanced field generated at the apex of such tips has been used to excite J-aggregates under two photon excitation [161, 83]. Apparently detected signal in this experiments which lead to resolutions as high as 20 nm is coming from a point far from the tip-sample interaction area. This is caused by strong energy transfer along the aggregate. Hence, doing similar type of experiments

with single emitters might lead to quenching and no observable signal.

Second-harmonic generation microscopy is another category of apertureless techniques which has been extensively studied [165, 166]. In these measurements thin metallic films were excited by a femtosecond pulsed laser coupled to an optical probe. These studies revealed that second harmonic light is not distributed homogeneously over the metal film but rather coming from randomly located confined areas [167]. The increased second harmonic response of these areas is in correlation with large electromagnetic enhancement which is originated from local excitation of resonant surface plasmons. By positioning a gold tip inside one of the longitudinal field lobes [168] and laser polarized along the tip axis, a very strong field enhancement is observed [169] which gives rise to second harmonic generation and is highly localized to the tip apex. Emission pattern of the emitted second harmonic light is identical to dipole oriented vertically on a dielectric substrate.

Another aspect of field enhancement generated at the apex of metallic tip under proper polarization is tip-enhanced Raman scattering, imaging and spectroscopy of carbon nanotubes as well as organic compounds [170, 83]. This approach is based on a relatively old background coming from surface enhanced Raman scattering (SERS) where Raman signal of the molecules on metallic surfaces is enhanced by orders of magnitude [91]. However, this effect in tip-enhanced Raman is highly localized to the tip apex. Plasmonic excitations on the tip apex increase the Raman scattering cross sections abruptly. This approach has led to resolutions down to 20 nm. Recently with exploiting the field enhancement of a sharp gold tip and detecting the Raman signal of G-band of single-walled carbon nanotubes resolution around 10 nm is also documented [171]. Similar approaches have taken in the so called, coherent anti-Stokes Raman scattering

(CARS) [172]. This technique utilizes three incident fields, pump field, Stokes field and probe field which induces nonlinear polarization at a specific frequency. When this frequency matches one of the specific molecular vibrational frequency of Raman-active modes, anti-Stokes Raman signal is generated and is highly confined around the tip apex. Although tip-enhanced Raman methods have lead to very high resolutions but there has not yet been any example of their application to resolve single emitters.

Combining the aperture SNOM with apertureless SNOM would lead to another type of near-field probes called "tip-on-Aperture" [53]. In this method a metallic tip is mounted at end of an fiber tip which is illuminated by light. Incident light excites the plasmons at the base of the metallic tip. They propagate along the tip which will then cause concentration of charges at the apex of the metallic tip (similar to lightning rod effect). By this technique single molecules with resolutions around 10 nm have been resolved despite strong quenching effects induced by the tip. Another approach that apparently have lead to resolving single semiconductor nanocrystals with resolution better than 10 nm is based on a tapping silicon tip, in tapping-mode AFM on the a sample of CdSe nanocrystals, the so called FANSOM [173, 174]. With time-gated imaging, that is, collecting the photons which are generated only when the tip taps the surface intensity image is formed. There are two unclear aspects in these results. One, Why a silicon tip which is a semiconductor should lead to field enhancement? Lightning rod effect is a result of oscillating free electrons which is not the case in a semiconductor which a few electron volt gap between the valence and conduction band. Two, silicon itself has fluorescence which is energetically at the same range of the nanocrystals used in this experiments. How fluorescence from the tips is split from the sample PL.

Although plasmonic excitations of a single metallic nanoparticle has been extensively studied [33, 38] there has not yet been any evidence of its potential to be used for fluorescence enhancements. This approach is based on Mie scattering a nanometer sized gold particle attached to the apex of a tip, whose plasmonic excitation lifetime decreases while approaching the surface.

The main task for a probe in scanning near-field optical microscopy is to capture the radiation from the selected "dipole" while discriminating the radiation from neighboring ones as effective as possible [45, 6]. In all the works based on a "metallic tip" and "single emitter" there is a competition going on, between the fluorescence quenching and enhancement. In some experiments PL is quenched [14] or enhanced [162], in close proximity to a tip. Based on most experimental observations and theoretical calculations the final result depends on many factors which can be categorized as the following. Tip material and geometry [175], architecture of the metallic tip [50, 176], polarization direction of the light with respect to tip axis [161], distance between the tip and orientation of the quantum emitter [175]. Optical antenna as it was explained in chapter 5 have very strong potentials to be used as a probe for near-field optical microscopy [177]. A very important aspect of the antenna probes is that the enhanced region is dependent on the gap size of the antenna, the smaller the gap the higher the resolution. Another important aspect is that when a single emitter is positioned inside the gap direct contact to the metal is negligible. Therefore, the chances of quenching is far less than than the elongated metallic tips. In the next section experiments which leads to high-resolution optical microscopy of single emitters are described. It will be shown how the fields existing inside the gap are exploited to resolve single semiconductor nanocrystals. The method is general and can also be applied to single molecules and other quantum emitters.

7.2 Results

Experiments in this section were all done under one-photon excitation. First a single quantum dot was immobilized inside the laser focus and antenna tip scans around the focal area. PL intensity map and lifetime map of the quantum dot as a function of the tip position are acquired, similar to Fig. 5.4. In the next step antenna tip is placed on the top of the bright area in the intensity image. This ensures that the antenna is positioned inside the laser focus. This is similar to the experiments done in sections 6.2 and 6.3. While the tip is frozen in this point sample scanner starts scanning the sample. This way, at any time that a nanocrystal enters the feedgap region of the antenna similar effects to Fig. 5.4 should take place, apart from the fact that here the nanocrystal is being scanned instead of tip. This way localized excitation of the nanocrystal leads to a fluorescence image of the sample with resolutions depending on the gap size. Figure 7.1 (e) shows the results of this experiments. As it can be seen each nanocrystal has several lobes of photoluminescence similar to Fig. 5.4 which is caused by reflections from the tip. In the center of all these lobes there is a highly confined bright spot which due to the interaction of the nanocrystal with feedgap of the antenna. The size of this bright points determines the resolution of this technique. To cross check that this effect is coming from the antenna, tip was retracted completely from the surface and sample scanner scanned the region marked in 7.1 (e) by red rectangle. The result is shown in 7.1 (a). It is clear that all the near field spots are gone and confocal signature of the nanocrystals is the result of microscopy. This clearly proves that the effect observed in (e) is originated from the tip. To compare the confinement and for resolution determination, the same nanocrystal in both measurements was selected, which is shown by green rectangle in Fig. 7.1

(a) & (e), shown in (b) and (c). A line-cut over the entire scan region in (b) and (c) gives the achieved confinement which is shown in Fig. 7.1 (d). When the tip is absent resolution is diffraction-limited, something around 300 nm in FWHM, the blue curve in (d). Near-field image of the same nanocrystal meaning when the tip is in the focus leads to a resolution of around 70-80 nm in FWHM identical to the gap size. This is shown in red curve of figure 7.1 (d). Another major difference is that although laser intensity in both measurements has kept the same (200 nW) same nanocrystal has a higher PL intensity in the presence of the tip which is almost 3 times more than the confocal of the same. This is another positive point of the effect that is caused by enhancement through the antenna feedgap. Based on the results presented in Fig.7.1 a resolution of $\lambda/7$ is documented by optical antennas as near-field optics probes.

Since lifetime data acquisition is in parallel with the intensity more information can still be obtained. The antenna effect is caused by the enhancement in the emission so the lifetime under one photon excitation is always shorter than the free dipole (section 5.4). Nanocrystal marked by blue rectangle in Fig. 7.1 (e) was selected for lifetime analysis whose intensity and lifetime data is shown in Figs. 7.1 (f) & (g). Comparing the lifetime of the bright point in the intensity image with surrounding environment it is obvious that photons in the bright point have shorter lifetime as compared to the others. This number is around 10 ns (blue in the color scale). This confirms that that enhanced point shown in Fig. 7.1 (f) is coming from a different origin rather than laser excitation which is localized fields of the antenna feedgap. These are convincing evidences for antenna probes to resolve single emitters with high-resolution (here $\lambda/7$). Resolution of this technique can be improved by better designing of the antenna. Smaller feedgaps will lead to higher-resolutions and higher enhancement factors.

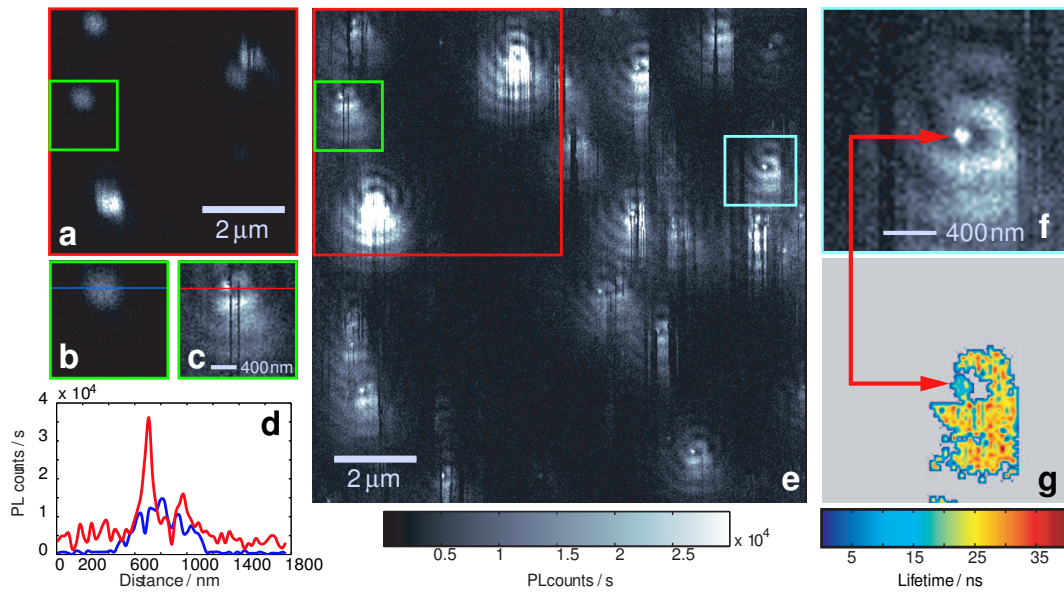


Figure 7.1: (a) PL intensity confocal image of quantum dot sample from the region marked by red rectangle in (e), this corresponds to the time when tip is retracted from the surface. (b) PL intensity image while the tip is retracted of the quantum dot marked by green rectangle in (a). (c) PL intensity image of the same quantum dot as (b) but when the tip is in contact. This qdot is marked by green rectangle in (e). (d) Line profiles of (b) and (c) for detail resolution analysis. (e) Apertureless near-field image of the nanocrystal sample acquired when the tip is inside the focus. (f) & (g) PL intensity and lifetime images of the nanocrystal shown by blue rectangle in (e) respectively.

Chapter 8

Summary

Proximity of a metallic tip to a single quantum emitter quenches the fluorescence via non-radiative energy transfer to the tip. In this thesis, it was shown by designing unique metallic nanostructures, i.e. bowtie nanoantennas, quenching processes can be overcome. In this work we isolated two dipoles, classical dipole of the bowtie antenna and quantum mechanical dipole of the single emitter, and their interactions were studied. In this configuration we could understand different processes including, radiative and non-radiative channels opened up for the single quantum emitter in contact with the antenna. We have learnt that the processes involved in this interaction is not only limited to the naive picture of *quenching* and *enhancement*. Emission properties of the single emitter, here CdSe{ZnS} nanocrystals, undergoes drastic changes in contact with the antenna *feedgap*. The alterations in the photoluminescence characteristics involve, radiative and non-radiative rates, quantum efficiency, absorption cross section, emission polarization and second-order autocorrelation function of the two-level system. Modifications of each of these fluorescence properties is influenced by the coupling between the antenna and nanocrystal as well as the

pumping regime. Therefore, antenna/NC system can be assumed as a new type emitter with widely adjustable radiation properties which we call a "tunable superemitter". Photophysical properties of such a superemitter, i.e. antenna/NC system, as compared with free nanocrystal is totally different, although they both originate from the same source which is excitation-relaxation cycles inside the semiconductor nanocrystal. Upon enhanced emission of the nanocrystal induced by the bowtie antenna under one-photon excitation, PL intensity of the antenna/NC system is more than the free nanocrystal, Fig. 5.4. This is associated by a reduction in lifetime of the antenna/NC system with respect to the free nanocrystal. To confirm the origin of such effect, the results can easily be compared with a fully-coated tip, Fig 5.3. Strong PL quenching in contact with the fully-coated tip proves the observed PL enhancement in contact with the antenna is caused by antenna structure of which the feedgap is the most significant. Using two-photon excitation, the antenna increases the absorption cross section of the nanocrystal, due to enhanced excitation by the antenna. This is confirmed by PL intensity and lifetime response of the nanocrystal in contact with the antenna, Fig. 5.9. In this condition, antenna increases the PL count rate but has no effect on the lifetime of the excited-state. Two-photon absorption cross sections of the free nanocrystal and antenna/NC system were studied in detail. Two-photon absorption cross section of a nanocrystal increased from $6.3 \times 10^{-37} \text{cm}^4 \text{s}$ to $20.2 \times 10^{-37} \text{cm}^4 \text{s}$ in contact with the bowtie antenna, Fig. 6.1. Ratio of the enlargement in absorption cross sections coincides with the measured enhanced excitation factor, ~ 3.2 . Another major difference in the emission properties of the antenna/NC system as compared to the free nanocrystal was the emission polarization characteristics. The in-plane angle of the emission polarization of nanocrystal undergoes a phase shift in contact with the antenna. In other words,

the in-plane angle of the emission or the emission direction of the nanocrystal in contact with the antenna is determined by the antenna orientation, Fig. 6.5. Another major signature of coupling intra-superemitter, is the larger value of the transition dipole with respect to the free nanocrystal. Absolute value of the transition dipole is dependent on the coupling between antenna and nanocrystal. This proves that characteristics of the emission polarization of the antenna/NC system, as an independent single emitter, are mainly determined by the bowtie nanoantenna. More insights on the electronic transitions inside nanocrystal were obtained by measurements of the second-order autocorrelation function of the free nanocrystal and in contact with the antenna, Fig. 6.8. Under one-photon excitation, the antenna leads to a lifetime reduction by promoting the radiative relaxation rates. As a result excitation-recombination cycles needed for single photon generation, occur faster. Hence, antenna/NC system can act as a more efficient single photon source compared to free nanocrystal. Since emission polarization of the superemitter is determined by the bowtie antenna orientation, single photons generated from the nanocrystal in contact with the antenna, are highly polarized along the antenna arms. This may have application in quantum cryptography. Development of a highly sensitive optical microscope based on bowtie antennas, with resolutions far beyond the diffraction limit was specifically pursued, as one of the goals of nano-optics research, Fig.7.1. Based on this measurements with bowtie antenna tips, a new type of apertureless sample scanning near-field optical microscope capable of detecting *single fluorophores* with resolutions down to $\sim 70 - 80nm$ was developed ($\lambda/7$). Resolution in this technique can still be improved by improving antenna feedgap.

Outlook

In this work absorption and emission characteristics of the antenna/NC system under different excitation regimes were studied. However, some aspects of the coupling between nanocrystal and bowtie antenna can be investigated in more details. With improving the characteristics of the antenna structure (total length and feedgap size) stronger coupling regimes can be achieved. Under stronger coupling regimes some properties of the superemitter can be investigated in more details, such as photon antibunching. In antibunching measurements, in order to confirm the biexcitonic emission from the antenna/NC system, spectroscopic studies can be performed. Possibility of such biexcitonic emissions as sources for entangled photons can be investigated, which has strong potentials for quantum information processing [178]. Absorption cross section of the nanocrystal in contact with the antenna can be investigated under one-photon excitation. Sensitivity and resolution of the antenna-based optical microscopy can be improved by smaller gaps of the antenna structure. Here superemitter was formed via coupling between an FIB designed antenna and a nanocrystal. However, similar studies can be done on well-designed chemically bounded metallic particles in contact with single molecules.

Bibliography

- [1] R.P. Feynman. There's plenty of room at the bottom. *Eng. Sci. Mag.*, 23:22, 1960.
- [2] G. Binning, H. Rohrer, Ch. Gerber, and E. Weibel. Surface studies by scanning tunneling microscopy. *Phys. Rev. Lett.*, 49:57, 1982.
- [3] G. Binning, C.F. Quate, and Ch. Gerber. Atomic force microscope. *Phys. Rev. Lett.*, 56:930, 1986.
- [4] K.-B. Lee, S.-J. Park, C.A. Mirkin, J.C. Smith, and M. Mrksich. Protein nanoarrays generated by dip-pen nanolithography. *Science*, 295:1702, 2002.
- [5] L.M. Demers, D.S. Ginger, S.-J. Park, Z. Li, S.-W. Chung, and C.A. Mirkin. Direct patterning of modified oligonucleotides on metals and insulators by dip-pen nanolithography. *Science*, 296:1836, 2002.
- [6] D.W. Pohl. Optics at the nanometer scale. *Phil. Trans. R. Soc. Lond. A*, 362:701, 2004.
- [7] H.S. Nalva. *Handbook of Nanostructured Materials and Nanotechnology, Vol. 1: Synthesis and Processing*. Academic Press, San Diego, CA, 2000.
- [8] D.W. Pohl, W. Denk, and M. Lanz. Optical stethoscopy: Image recording with resolution $\lambda/20$. *Appl. Phys. Lett.*, 44:651, 1984.
- [9] L. Novotny and B. Hecht. *Principles of Nano-Optics*. Cambridge University Press, Cambridge, 2006.
- [10] M. Ohtsu and H. Hori. *Near-Field Nano-Optics*. Kluwer Academic, New York, 1999.
- [11] B. Lounis and M. Orrit. Single-photon sources. *Rep. Prog. Phys.*, 68:1129, 2005.
- [12] B. Darquie, M.P.A. Jones, J. Dingjan, J. Beugnon, S. Bergamini, Y. Sortais, G. Messin, A. Browaeys, and P. Grangier. Controlled single-photon emission from a single trapped two-level atom. *Science*, 309:454, 2005.

- [13] A.P. Alivisatos. Semiconductor clusters, nanocrystals and quantum dots. *Science*, 271:933, 1996.
- [14] W. Tröbsinger, A. Kramer, M. Kreiter, B. Hecht, and U.P. Wild. Single-molecule near-field optical energy transfer microscopy. *Appl. Phys. Lett.*, 81:2118, 2002.
- [15] W. Tröbsinger, A. Kramer, M. Kreiter, B. Hecht, and U.P. Wild. Single-molecule near-field optical energy transfer microscopy with dielectric tips. *J. Microsc.*, 209:249, 2002.
- [16] B. Hecht. Nano-optics with single quantum systems. *Phil. Trans. R. Soc. Lond. A*, 362:881, 2004.
- [17] S.A. Empedocles, R. Neuhauser, K. Shimitzu, and M.G. Bawendi. Photoluminescence from single semiconductor nanostructures. *Adv. Mater.*, 11:1243, 1999.
- [18] V.I. Klimov. Nanocrystal quantum dots, from fundamental photophysics to multicolor lasing. *Los Alamos Science*, 28:214, 2003.
- [19] P. Alivisatos. The use of nanocrystals in biological detection. *Nature Biotechnology*, 22:47, 2004.
- [20] B.O. Dabbousi *et al.* (CdSe)ZnS core-shell quantum dots: synthesis and characterization of a size series of highly luminescent nanocrystallites. *J. Phys. Chem. B*, 101:9463, 1997.
- [21] X. Zhu and M. Ohtsu. *Near-Field Optics: Principles and Applications*. World Scientific, Beijing, China, 1999.
- [22] H.A. Atwater, S. Maier, A. Polman, J.A. Dionne, and L. Swearlock. The new "p-n" junction: Plasmonics enables photonic access to the nanoworld. *MRS Bulletin*, 30:385, 2005.
- [23] C.J. Murphy, T.K. Sau, A. Gole, and C.J. Orendorff. Surfactant-directed synthesis and optical properties of one-dimensional plasmonic metallic nanostructures. *MRS Bulletin*, 30:349, 2005.
- [24] E. Hutter and J.H. Fendler. Exploitation of localized surface plasmon resonance. *Adv. Mater.*, 16:1685, 2004.
- [25] O.J.F. Martin. Plasmon resonances in nanowires with a non-regular cross section. In J. Tominaga and D.P. Tsai, editors, *Manipulation of Surface and Local Plasmons*, Heidelberg, 2002. Springer.

-
- [26] S. Berciaud, L. Cognet, P. Tamarat, and B. Lounis. Observation of intrinsic size effects in the optical response of individual gold nanoparticle. *Nano Lett.*, 5:515, 2005.
- [27] A. Arbouet, D. Christofilos, N.D. Fatti, F. Vallee, J.R. Huntzinger, L. Arnaud, P. Billaud, and M. Broyer. Direct measurement of the single-metal-cluster optical absorption. *Phys. Rev. Lett.*, 93:127401, 2004.
- [28] J. Aizpurua, P. Hanarp, D.S. Sutherland, M. Kaell, G.W. Bryant, and F.J. Garcia de Abajo. Optical properties of gold nanorings. *Phys. Rev. Lett.*, 90:057401, 2003.
- [29] Y. Xia and N.J. Halas. Shape-controlled synthesis and surface plasmonic properties of metallic nanostructures. *MRS Bulletin*, 30:338, 2005.
- [30] C.F. Bohren and D.R. Huffman. *Absorption and scattering of light by small particles*. Wiley Interscience, United States of America, 1983.
- [31] U. Kreibig and M. Vollmer. *Optical Properties of Metal Clusters*. Springer, Berlin, 1995.
- [32] T. Kalkbrenner, U. Håkanson, and V. Sandoghdar. Tomographic plasmon spectroscopy of a single gold nanoparticle. *Nano Lett.*, 4:2309, 2004.
- [33] T. Kalkbrenner, U. Håkanson, A. Schädle, S. Burger, C. Henkel, and V. Sandoghdar. Optical microscopy via spectral modifications of a nanoantenna. *Phys. Rev. Lett.*, 95:200801, 2005.
- [34] E. Dulkeith, M. Ringler, T.A. Klar, J. Feldman, A.M. Javier, and W.J. Parak. Gold nanoparticles quench fluorescence by phase induced radiative rate suppression. *Nano Lett.*, 5:585, 2005.
- [35] J. Jiang, K. Bosnick, M. Maillard, and L. Brus. Single molecule raman spectroscopy at the junctions of large Ag nanocrystals. *J. Phys. Chem. B*, 107:9964, 2003.
- [36] J. Aizpurua, G.W. Bryant, L.J. Richter, F.J. Garcia de Abajo, B.K. Kelley, and T. Mallouk. Optical properties of coupled metallic nanorods for field-enhanced spectroscopy. *Phys. Rev. B*, 71:235420, 2005.
- [37] A.M. Michaels, J. Jiang, and L. Brus. Ag nanocrystal junctions as the site for surface-enhanced raman scattering of single Rhodamine 6G molecules. *J. Phys. Chem. B*, 104:11965, 2000.
- [38] B.C. Buchler, T. Kalkbrenner, C. Hettich, and V. Sandoghdar. Measuring the quantum efficiency of the optical emission of single radiating dipoles using a scanning mirror. *Phys. Rev. Lett.*, 95:063003, 2005.

- [39] Z. Gueroui and A. Libchaber. Single-molecule measurements of gold-quenched quantum dots. *Phys. Rev. Lett.*, 93:166108, 2004.
- [40] E. Dulkeith *et al.* Fluorescence quenching of dye molecules near gold nanoparticles: Radiative and nonradiative effects. *Phys. Rev. Lett.*, 89:203002, 2002.
- [41] G.C. Papavassiliou. Optical properties of small inorganic and organic metal particles. *Prog. Solid State Chem.*, 12:185, 1979.
- [42] A.J. Hallock, P.L. Redmond, and L.E. Brus. Optical forces between metallic particles. *Proc. Natl. Acad. Sci. USA*, 102:1280, 2005.
- [43] C.A. Balanis. *Antenna Theory*. Harper & Row, New York, 1982.
- [44] C.A. Balanis. Antenna theory: A review. *Proceedings of the IEEE*, 80:7, 1992.
- [45] D.W. Pohl. Near Field Optics Seen as an Antenna Problem. In X. Zhu and M. Ohtsu, editors, *Near-Field Optics: Principles and Applications*, Beijing, China, 1999. World Scientific.
- [46] P. Muehlschlegel, H.-J. Eisler, O.J.F. Martin, B. Hecht, and D.W. Pohl. Resonant optical antennas. *Science*, 308:1607, 2005.
- [47] D.P. Fromm, A. Sundaramurthy, P.J. Schuck, G. Kino, and W.E. Moerner. Gap-dependent optical coupling of single "Bowtie" nanoantennas resonant in the visible. *Nano Lett.*, 4:957, 2004.
- [48] P.J. Schuck, D.P. Fromm, A. Sundaramurthy, G.S. Kino, and W.E. Moerner. Improving the mismatch between light and nanoscale objects with gold bowtie nanoantennas. *Phys. Rev. Lett.*, 94:017402, 2005.
- [49] A. Sundaramurthy, K.B. Crozier, G.S. Kino, D.P. Fromm, P.J. Schuck, and W.E. Moerner. Field enhancement and gap-dependent resonance in a system of two opposing tip-to-tip Au nanotriangles. *Phys. Rev. B*, 72:165409, 2005.
- [50] J.N. Farahani, D.W. Pohl, H.-J. Eisler, and B. Hecht. Single quantum dot coupled to a scanning optical antenna: A tunable superemitter. *Phys. Rev. Lett.*, 95:017402, 2005.
- [51] K.B. Crozier, A. Sundaramurthy, G.S. Kino, and C.F. Quate. Optical antenna: Resonators for local field enhancement. *J. Appl. Phys.*, 94:4632, 2003.

-
- [52] P.B. Johnson and R.W. Christy. Optical constant of noble metals. *Phys. Rev. B*, 6:4370, 1972.
- [53] H.G. Frey, S. Witt, K. Felderer, and R. Guckenberger. High-resolution imaging of single fluorescent molecules with the optical near-field of a metal tip. *Phys. Rev. Lett.*, 93:200801, 2004.
- [54] W.L. Barnes. Fluorescence near interfaces: the role of photonic mode density. *J. Mod. Phys.*, 45:661, 1998.
- [55] R.R. Chance, A. Prock, and R. Silbey. Molecular fluorescence and energy transfer near interfaces. *Adv. Chem. Phys.*, 37:1, 1978.
- [56] L. Novotny. Single molecule fluorescence in inhomogeneous environments. *Appl. Phys. Lett.*, 69:3806, 1996.
- [57] R.R. Chance, A. Prock, and R. Silbey. Lifetime of an emitting molecule near a partially reflecting surface. *J. Chem. Phys.*, 60:2744, 1974.
- [58] J.I. Gersten and A. Nitzan. Spectroscopic properties of molecules interacting with small particles. *J. Chem. Phys.*, 75:1139, 1981.
- [59] D.A. Weitz, S. Garoff, J.I. Gersten, and A. Nitzan. The enhancement of raman scattering, resonance raman scattering and fluorescence from molecules adsorbed on a rough silver surface. *J. Chem. Phys.*, 78:5324, 1983.
- [60] M. Minski. *Microscopy Apparatus, U.S. Patent: 3013467*. 1957.
- [61] D. O'Connor and D. Philips. *Time-Correlated Single-Photon Counting*. Academic, London, 1984.
- [62] W. Tröbsinger, C.G. Huebner, B. Hecht, and U.P. Wild. Continuous real-time measurement of fluorescence lifetimes. *Rev. Sci. Instr.*, 73:3122, 2002.
- [63] M. Kreiter, M. Prummer, B. Hecht, and U.P. Wild. Orientation dependence of fluorescence lifetimes near an interface. *J. Chem. Phys.*, 117:9430, 2002.
- [64] T. Basche, W.E. Moerner, M. Orrit, and U.P. Wild. *Single-Molecule optical Detection, Imaging and Spectroscopy*. VCH Verlagsgesellschaft mbH, Weinheim, 1997.
- [65] B. Sick, B. Hecht, and L. Novotny. Orientational imaging of single molecules by annular illumination. *Phys. Rev. Lett.*, 85:4482, 2000.
- [66] B. Sick, B. Hecht, U.P. Wild, and L. Novotny. Probing confined fields with single molecules and *vice versa*. *J. Microsc.*, 202:365, 2001.

- [67] C.A. Leatherdale, W.-K. Woo, F.V. Mikulec, and M.G. Bawendi. On the absorption cross section of CdSe nanocrystal quantum dots. *J. Phys. Chem. B*, 106:7619, 2002.
- [68] X. Brokmann, L. Coolen, M. Dahan, and J.P. Hermier. Measurement of radiative and nonradiative decay rates of single CdSe nanocrystals through a controlled modification of their spontaneous emission. *Phys. Rev. Lett.*, 93:107403, 2004.
- [69] I. Chung and M.G. Bawendi. Relationship between single quantum-dot intermittency and fluorescence decays from collection of dots. *Phys. Rev. B*, 70:165304, 2004.
- [70] P.T.C. So, C.Y. Dong, B.R. Masters, and K.M. Berland. Two-photon excitation fluorescence microscopy. *Ann. Rev. Biomed. Eng.*, 02:399, 2000.
- [71] E.J. Sanchez, L. Novotny, G.R. Holtom, and X.S. Xie. Room-temperature fluorescence imaging and spectroscopy of single molecules by two-photon excitation. *J. Phys. Chem. B*, 101:7019, 1997.
- [72] A.M. van Oijen, R. Verbeek, Y. Durand, J. Schmidt, J.N.J. van Lingen, A.A. Bol, and A. Meijerink. Continuous-wave two-photon excitation of individual CdSe nanocrystallites. *Appl. Phys. Lett.*, 79:830, 2001.
- [73] M. Albota *et al.* Design of organic molecules with large two-photon absorption cross sections. *Science*, 281:1653, 1998.
- [74] N. Mukherjee and A. Mukherjee and B.A. Reinhardt. Measurement of two-photon absorption cross sections of dye molecules doped in thin films of polymethylmethacrylate. *Appl. Phys. Lett.*, 70:1524, 1997.
- [75] D.R. Larson *et al.* Water-soluble quantum dots for multiphoton fluorescence imaging in vivo. *Science*, 300:1434, 2003.
- [76] Y. Lill and B. Hecht. Single dye molecules in an oxygen-depleted environment as photostable organic triggered single-photon sources. *Appl. Phys. Lett.*, 84:1665, 2004.
- [77] U.P. Wild. Characterization of triplet states by optical spectroscopy. *Topic. Curr. Chem.*, 55:1, 1975.
- [78] R.G. Neuhauser, K.T. Shimizu, W.K. Woo, S.A. Empedocles, and M.G. Bawendi. Correlation between fluorescence intermittency and spectral diffusion in single semiconductor quantum dots. *Phys. Rev. Lett.*, 85:3301, 2000.

-
- [79] V.I. Klimov. Optical nonlinearities and ultrafast carrier dynamics in semiconductor nanocrystals. *J. Phys. Chem. B*, 104:6112, 2000.
- [80] J. Meingailis. Focused ion beam technology and applications: critical review. *J. Vac. Sci. Technol. B*, 5:469, 1987.
- [81] J.T. Krug II, E.J. Sanchez, and X.S. Xie. Fluorescence quenching in tip-enhanced nonlinear optical microscopy. *Appl. Phys. Lett.*, 86:233102, 2005.
- [82] E.J. Sanchez, L. Novotny, and X.S. Xie. Near-field fluorescence microscopy based on two-photon excitation with metal tips. *Phys. Rev. Lett.*, 82:4014, 1999.
- [83] A. Hartshuh, E.J. Sánchez, X.S. Xie, and L. Novotny. High-resolution near-field raman microscopy of single-walled carbon nanotubes. *Phys. Rev. Lett.*, 90:095503, 2003.
- [84] J. Azoulay, A. Debarre, A. Richard, and P. Tchenio. Quenching and enhancement of single-molecule fluorescence under metallic and dielectric tips. 51:374, 2000.
- [85] J. Gersten and A. Nitzan. Electromagnetic theory of enhanced raman scattering by molecules absorbed on surfaces. *J. Chem. Phys.*, 73:3023, 1980.
- [86] M.R. Beverlius, A. Bouhelier, and L. Novotny. Continuum generation from single gold nanostructures through near-field mediated intraband transitions. *Phys. Rev. B*, 68:115433, 2003.
- [87] M. Kobayashi, K. Fujita, O. Nakamura, and S. Kawata. Time-gated imaging for multifocus second-harmonic generation microscopy. *Appl. Phys. Lett.*, 76:073704, 2005.
- [88] M. Lippitz, M.A. van Dijk, and M. Orrit. Third-harmonic generation from single gold nanoparticles. *Nano Lett.*, 5:799, 2005.
- [89] R.A. Farrer, F.L. Butterfield, V.W. Chen, and J.T. Fourkas. Highly efficient multiphoton-absorption-induced luminescence from gold nanoparticles. *Nano Lett.*, 5:1139, 2005.
- [90] K.T. Shimitzu, W.K. Woo, B.R. Fisher, H.J. Eisler, and M.G. Bawendi. Surface-enhanced emission from single semiconductor nanocrystals. *Phys. Rev. Lett.*, 89:117401, 2002.
- [91] M. Moskovits. Surface-enhanced spectroscopy. *Rev. Mod. Phys.*, 57:783, 1985.

- [92] T. Plakhotnik, D. Walser, M. Pirotta, A. Renn, and U.P. Wild. Nonlinear spectroscopy on a single quantum system: two-photon absorption of a single molecule. *Science*, 271:1703, 1996.
- [93] J.S. Biteen, D. Pacifici, S. Lewis, and H.A. Atwater. Enhanced radiative emission rate and quantum efficiency in coupled silicon nanocrystal-nanostructured gold emitters. *Nano Lett.*, 5:1768, 2005.
- [94] J.J. Macklin, J.K. Trautman, T.D. Harris, and L.E. Brus. Imaging and time-resolved spectroscopy of single molecules at an interface. *Science*, 272:255, 1996.
- [95] E. Betzig and R.J. Chichester. Single molecule observed by near-field scanning optical microscopy. *Science*, 262:1422, 1993.
- [96] A.G. Ruiter, J.A. Veerman, M.F. Garcia-Parajo, and N.F. van Hulst. Single molecule rotational and translational diffusion observed by near-field scanning optical microscopy. *J. Phys. Chem. A*, 101:7318, 1997.
- [97] M. Boehmer and J. Enderlein. Orientatin imaging of single molecules by wide-field epifluorescence microscopy. *J. Opt. Soc. Am. B*, 20:554, 2003.
- [98] M.A. Lieb, J.M. Zavislan, and L. Novotny. Single-molecule orientations determined by direct emission pattern imaging. *J. Opt. Soc. Am. B*, 21:1210, 2004.
- [99] T. Ha, Th. Enderle, D.S. Chemla, P.R. Selvin, and S. Weiss. Single molecule dynamics studied by polarization microscopy. *Phys. Rev. Lett.*, 77:3979, 1996.
- [100] F. Guettler, M. Croci, A. Renn, and U.P. Wild. Single molecule polarization spectroscopy: pentacene in p-terphenyl. *Chem. Phys.*, 211:421, 1996.
- [101] T. Ha, T.A. Laurence, D.S. Chemla, and S. Weiss. Polarization spectroscopy of single fluorescent molecules. *J. Phys. Chem. B*, 103:6839, 1999.
- [102] M.A. Bopp, Y. Jia, G. Haran, E.A. Morlino, and R.M. Hochstrasser. Single-molecule spectroscopy with 27 fs pulses: time-resolved experiments and direct imaging of orientational distributions. *Appl. Phys. Lett.*, 73:7, 1998.
- [103] Al.L. Efros, M. Rosen, M. Kuno, M. Nirmal, D.J. Norris, and M. Bawendi. Band-edge exciton in quantum dots of semiconductors with a degenerate valence band: Dark and bright exciton states. *Phys. Rev. B*, 54:4843, 1996.
- [104] Al.L. Efros. Luminescence polarization of CdSe microcrystals. *Phys. Rev. B*, 46:7448, 1992.

-
- [105] E. Rothenberg, Y. Ebenstein, M. Kazes, and U. Banin. Two-photon fluorescence microscopy of single semiconductor quantum rods: direct observation of highly polarized nonlinear absorption dipole. *J. Phys. Chem. B*, 108:2797, 2004.
- [106] J. Hu, L.S. Li, W. Yang, L. Manna, L.W. Wang, and A.P. Alivisatos. Linearly polarized emission from colloidal semiconductor quantum rods. *Science*, 292:2060, 2001.
- [107] S.A. Empedocles, R. Neuhauser, and M.G. Bawendi. Three-dimensional orientation measurements of symmetric single chromophores using polarization microscopy. *Nature*, 399:126, 1999.
- [108] F. Koberling, U.Kolb, G. Philipp, I. Potapova, T. Basche, and A. Mews. Fluorescence anisotropy and crystal structure of individual semiconductor nanocrystals. *J. Phys. Chem. B*, 107:7463, 2003.
- [109] S. Empedocles and M. Bawendi. Spectroscopy of single CdSe nanocrystal-lites. *Acc. Chem. Res.*, 32:389, 1999.
- [110] X. Michalet, F. Pinaud, T.D. Lacoste, M. Dahan, M.P. Bruchez, A.P. Alivisatos, and S. Weiss. Properties of fluorescent semiconductor nanocrystals and their application to biological labeling. *Single Mol.*, 2:261, 2001.
- [111] M.O. Scully and M.S. Zubairy. *Quantum Optics*. Cambridge University Press, Cambridge, 1997.
- [112] R. Hanbury-Brown and R.Q. Twiss. A test of a new type of stellar interferometer on sirius. *Nature*, 178:1046, 1956.
- [113] P. Kumar, P. Kwait, A. Migdall, S.W. Nam, J. Vuckovic, and F.N.C. Wong. Photonic technologies for quantum information processing. *Quant. Inf. Proc.*, 3:215, 2004.
- [114] N. Gisin, G. Ribordy, W. Tittel, and H. Zbinden. Quantum cryptography. *Rev. Mod. Phys.*, 74:145, 2002.
- [115] A. Beveratos, R. Brouri, T. Gacoin, A. Villing, J.-P. Poizat, and P. Grangier. Single photon quantum cryptography. *Phys. Rev. Lett.*, 89:187901, 2002.
- [116] B. Lounis and W.E. Moerner. Single photons on demand from a single molecule at room temperature. *Nature*, 407:491, 2000.
- [117] H.J. Kimble, M. Dagenais, and L. Mandel. Photon antibunching in resonance fluorescence. *Phys. Rev. Lett.*, 39:691, 1977.

- [118] F. Diedrich and H. Walther. Nonclassical radiation of a single stored ion. *Phys. Rev. Lett.*, 58:203, 1978.
- [119] C. Kurtsiefer, S. Mayer, P. Zarda, and H. Weinfurter. Stable solid-state source of single photons. *Phys. Rev. Lett.*, 85:290, 2000.
- [120] A. Kiraz, M. Ehrl, Th. Hellerer, Ö.E. Muestecaplioğlu, C. Bräuchle, and A. Zumbush. Indistinguishable photons from a single molecule. *Phys. Rev. Lett.*, 94:223602, 2005.
- [121] L. Fleury, J.-M. Segura, G. Zumofen, B. Hecht, and U.P. Wild. Nonclassical photon statistics in single-molecule fluorescence at room temperature. *Phys. Rev. Lett.*, 84:1148, 2000.
- [122] C. Santori, M. Pelton, G. Solomon, Y. Dale, and Y. Yamamoto. Triggered single photons from a quantum dot. *Phys. Rev. Lett.*, 86:1502, 2001.
- [123] V. Zwiller, H. Blom, P. Jonsson, N. Panev, S. Jeppesen, T. Tsegaye, E. Goobar, M. Pistol, L. Samuelson, and G. Björk. Single quantum dots emit single photons at a time: Antibunching experiments. *Appl. Phys. Lett.*, 78:2476, 2001.
- [124] V. Zwiller, T. Aichele, W. Seifert, J. Persson, and O. Benson. Generating visible single photons on demand with single InP quantum dots. *Appl. Phys. Lett.*, 82:1509, 2003.
- [125] V. Zwiller, T. Aichele, F. Hatami, W.T. Masselink, and O. Benson. Growth of single quantum dots on preprocessed structures: Single photon emitters on a tip. *Appl. Phys. Lett.*, 86:091911, 2005.
- [126] K. Sebald, P. Michler, T. Passow, D. Hommel, G. Bacher, and A. Forchel. Single-photon emission of CdSe/ZnS quantum dots at temperatures up to 200 K. *Appl. Phys. Lett.*, 81:2920, 2002.
- [127] P. Michler, A. Imamoglu, M.D. Mason, P.J. Carson, G.F. Strouse, and S.K. Buratto. Quantum correlation among photons from a single quantum dot at room temperature. *Nature*, 406:968, 2000.
- [128] B. Lounis, H.A. Bechtel, D. Gerion, and P. Alivisatos and W.E. Moerner. Photon antibunching in single CdSe/ZnS quantum dot fluorescence. *Chem. Phys. Lett.*, 329:399, 2000.
- [129] X. Brokmann, E. Giacobino, M. Dahan, and J.P. Hermier. Highly efficient triggered emission of single photons by colloidal CdSe/ZnS nanocrystals. *Appl. Phys. Lett.*, 85:712, 2004.

-
- [130] M. Achermann, J.A. Hollingsworth, and V.I. Klimov. Multiexcitons confined within a subexcitonic volume: Spectroscopic and dynamical signatures of neutral and charged biexcitons in ultrasmall semiconductor nanocrystals. *Phys. Rev. B*, 68:245302, 2003.
- [131] V.I. Klimov, A.A. Mikhailovsky, D.W. McBranch, C.A. Leatherdale, and M.G. Bawendi. Quantization of multiparticle auger rates in semiconductor quantum dots. *Science*, 287:1011, 2000.
- [132] V.I. Klimov. Optical nonlinearities and ultrafast carrier dynamics in semiconductor nanocrystals. *J. Phys. Chem. B*, 104:6112, 2000.
- [133] L.-W. Wang, M. Califano, A. Zunger, and A. Franceschetti. Pseudopotential theory of Auger processes in CdSe quantum dots. *Phys. Rev. Lett.*, 91:056404, 2003.
- [134] M. Nirmal, B.O. Dabousi, M.G. Bawendi, J.J. Macklin, J.K. Trautman, T.D. Harris, and L.E. Brus. Fluorescence intermittency in single cadmium selenide nanocrystals. *Nature*, 383:802, 1996.
- [135] A.L. Efros and M. Rosen. Random telegraph signal in the photoluminescence intensity of a single quantum dot. *Phys. Rev. Lett.*, 78:1110, 1997.
- [136] M. Kuno, D.P. Fromm, S.T. Johnson, A. Gallagher, and D.J. Nesbitt. Modeling distributed kinetics in isolated semiconductor quantum dots. *Phys. Rev. B*, 67:125304, 2003.
- [137] V.I. Klimov, D.W. McBranch, C.A. Leatherdale, and M.G. Bawendi. Electron and hole relaxation pathways in semiconductor quantum dots. *Phys. Rev. B*, 60:13740, 1999.
- [138] V.I. Klimov, Ch.J. Schwarz, D.W. McBranch, C.A. Leatherdale, and M.G. Bawendi. Ultrafast dynamics of inter- and intraband transitions in semiconductor nanocrystals: Implications for quantum-dot lasers. *Phys. Rev. B*, 60:R2177, 1999.
- [139] M. Kuno, D.P. Fromm, H.F. Hamann, A. Gallagher, and D.J. Nesbitt. "On"/"off" fluorescence intermittency of single semiconductor quantum dots. *J. Chem. Phys.*, 115:1028, 2001.
- [140] S. Hohng and T. Ha. Near-complete suppression of quantum dot blinking in ambient conditions. *J. Am. Chem. Soc.*, 126:1324, 2004.
- [141] R. Brouri, A. Beveratos, J.-P. Poizat, and P. Grangier. Single-photon generation by pulsed excitation of a single dipole. *Phys. Rev. A*, 62:063817, 2000.

- [142] B. Fisher, J.M. Caruge, D. Zehnder, and M. Bawendi. Room-temperature ordered photon emission from multiexciton states in single CdSe core-shell nanocrystals. *J. Phys. Chem. B*, 101:9463, 1997.
- [143] B. Fisher, J.M. Caruge, D. Zehnder, and M.G. Bawendi. Room-temperature ordered photon emission from multiexciton states in single CdSe core-shell nanocrystals. *Phys. Rev. Lett.*, 94:087403, 2005.
- [144] E.M. Purcell, H.C. Torrey, and R.V. Pound. Resonance absorption by nuclear magnetic moments in a solid. *Phys. Rev.*, 69:37, 1946.
- [145] E. Peter, P. Senellart, D. Martrou, A. Lemaître, J. Hours, J.M. Gérard, and J. Bloch. Exciton-photon strong-coupling regime for a single quantum dot embedded in a microcavity. *Phys. Rev. Lett.*, 95:067401, 2005.
- [146] A. Badolto, K. Hennessy, M. Atatüre, J. Dreiser, E. Hu, P.M. Petroff, and A. Imamoglu. Deterministic coupling of single quantum dots to single nanocavity modes. *Science*, 308:1158, 2005.
- [147] A. Kiraz, C. Reese, B. Gayral, L. Zhang, W.V. Schoenfeld, B.D. Gerardot, P.M. Petroff, E.L. Hu, and A. Imamoglu. Cavity-quantum electrodynamics with quantum dots. *J. Opt. B: Quantum Semiclass. Opt.*, 5:129, 2003.
- [148] W.D. Pohl. Optical near-field scanning microscope. *U.S. Patent*, 4,604,520:1–8, 1986.
- [149] E. Betzig, J.K. Trautman, T.D. Harris, J.S. Weiner, and R.L. Kostelak. Breaking the diffraction barrier: Optical microscopy on a nanometer scale. *Science*, 251:1468, 1991.
- [150] E. Betzig and J.K. Trautman. Near-field optics: microscopy, spectroscopy, and surface modification beyond the diffraction limit. *Science*, 257:189, 1992.
- [151] R.C. Dunn. Near-field scanning optical microscopy. *Chem. Rev.*, 99:2891, 1999.
- [152] R.X. Bian, R.C. Dunn, X.S. Xie, and P.T. Leung. Single molecule emission characteristics in near-field microscopy. *Phys. Rev. Lett.*, 75:4772, 1995.
- [153] B. Hecht, B. Sick, U.P. Wild, V. Deckert, R. Zenobi, O.J.F. Martin, and D.W. Pohl. Scanning near-field optical microscopy with aperture probes: Fundamentals and applications. *J. Chem. Phys.*, 112:7761, 2000.
- [154] B. Hecht, H. Bielefeldt, Y. Inouye, D.W. Pohl, and L. Novotny. Facts and artifacts in near-field optical microscopy. *J. Appl. Phys.*, 81:2492, 1997.

-
- [155] F. Zenhausern, M.P. O'Boyle, and H.K. Wickramasinghe. Apertureless near-field optical microscope. *Appl. Phys. Lett.*, 65:1623, 1994.
- [156] H.K. Wickramasinghe and C.C. Williams. Apertureless near-field optical microscope. *U.S. Patent*, 4,947,034:1–7, 1990.
- [157] R. Hillenbrand, T. Taubner, and F. Keilmann. Photon-enhanced light-matter interaction at the nanometer scale. *Nature*, 418:159, 2002.
- [158] R. Hillenbrand, B. Knoll, and F. Keilmann. Pure optical contrast in scattering-type scanning near-field microscopy. *J. Microsc.*, 202:77, 2001.
- [159] M. Specht, J.D. Pedarling, W.M. Heckl, and T.W. Hänsch. Scanning plasmon near-field microscope. *Phys. Rev. Lett.*, 68:476, 1992.
- [160] F. Zenhausern, Y. Martin, and H.K. Wickramasinghe. Scanning interferometric apertureless microscopy: Optical imaging at 10 angstrom resolution. *Science*, 269:1083, 1995.
- [161] E.J. Sanchez, L. Novotny, and X.S. Xie. Near-field fluorescence microscopy based on two-photon excitation with metal tips. *Phys. Rev. Lett.*, 82:4014, 1999.
- [162] A. Kramer, W. Trabesinger, B. Hecht, and U.P. Wild. Optical near-field enhancement at the metal tip probed by a single fluorophore. *Appl. Phys. Lett.*, 80:1652, 2002.
- [163] J. Azoulay, A. Débarre, A. Richard, and P. Tchério. Field enhancement and apertureless near-field optical spectroscopy of single molecules. *J. Microsc.*, 194:486, 1999.
- [164] A. Hartshuh, M.R. Beversluis, A. Bouhelier, and L. Novotny. Tip-enhanced optical spectroscopy. *Phil. Trans. R. Soc. Lond. A*, 362:807, 2004.
- [165] A.V. Zayats and V. Sandoghdar. Apertureless near-field optical microscopy via local second harmonic generation. *J. Microsc.*, 202:94, 2001.
- [166] S.I. Bozhevolnyi and V.Z. Lozovski. Second-harmonic scanning optical microscopy of individual nanostructures. *Phys. Rev. B*, 65:235420, 2002.
- [167] S.I. Bozhevolnyi, J. Beermann, and V. Coello. Direct observation of localized second-harmonic enhancement in random metal nanostructures. *Phys. Rev. Lett.*, 90:197403, 2003.
- [168] A. Bouhelier, M. Beversluis, and L. Novotny. Near-field scattering of longitudinal fields. *Appl. Phys. Lett.*, 82:4596, 2003.

- [169] A. Bouhelier, M. Beversluis, A. Hartshuh, and L. Novotny. Near-field second harmonic generation induced by local field enhancement. *Phys. Rev. Lett.*, 90:193903, 2003.
- [170] N. Hayazawa, Y. Inouye, Z. Sekkat, and S. Kawata. Near-field raman imaging of organic molecules by an apertureless metallic probe scanning optical microscope. *J. Chem. Phys.*, 117:1296, 2002.
- [171] A. Hartshuh, H. Qian, A.J. Meixner, N. Anderson, and L. Novotny. Nanoscale optical imaging of excitons in single-walled carbon nanotubes. *Nano Lett.*, 5:2310, 2005.
- [172] T. Ichimura, N. Hayazawa, M. Hashimoto, and Y. Inouye and S. Kawata. Tip-enhanced coherent anti-Stokes Raman scattering for vibrational nanoimaging. *Phys. Rev. Lett.*, 92:2208010, 2004.
- [173] T.J. Yang, G.A. Lessard, and S.R. Quake. An apertureless near-field microscope for fluorescence imaging. *Appl. Phys. Lett.*, 76:378, 2000.
- [174] J.M. Gerton, L.A. Wade, G.A. Lessard, Z. Ma, and S.R. Quake. Tip-enhanced fluorescence microscopy at 10 nanometer resolution. *Phys. Rev. Lett.*, 93:180801, 2004.
- [175] J. Azoulay, A. Debarre, A. Richard, and P. Tchenio. Quenching and enhancement of single-molecule fluorescence under metallic and dielectric tips. *Europhys. Lett.*, 51:374, 2000.
- [176] J.-H. Song, T.A. Atay, S. Shi, H. Urabe, and A.V. Nurmikko. Large enhancement of fluorescence efficiency from CdSe/ZnS quantum dots induced by resonant coupling to spatially controlled surface plasmons. *Nano Lett.*, 5:1557, 2005.
- [177] J.N. Farahani, H.-J. Eisler, D.W. Pohl, and B. Hecht. Optical antennas as local probes for near-field optics. *in preparation*.
- [178] O. Gywat, G. Burkard, and D. Loss. Biexcitons in coupled quantum dots as a source of entangled photons. *Phys. Rev. B*, 65:205329, 2002.
- [179] W. Lukosz. Light emission by magnetic and electric dipoles close to a plane dielectric interface. iii. radiation patterns of dipoles with arbitrary orientation. 69:1495, 1979.

Appendix A

Emission Polarization

Measurements

In section 6.2 measurements regarding emission polarization, including in-plane angle and out-of-plane angle of semiconductor nanocrystals leading to 3D information of their orientation was presented. Several aspects of these results should be further clarified. In the following paragraphs I explain the procedure taken to measure the presented data (figure 6.5) which will be followed by the required correction caused by the optical system. Finally, the actual meaning of interpretation of these results which are based on radiating dipole in free space is explained. Since the sample is on a quartz substrate the emission pattern is slightly different than in the free space.

A.1 Measurements

In this measurements we assume a radiating dipole in the sample plane. This means, the out-of-plane angle of this dipole is zero. This is done to simplify the

data analysis. In data shown in Fig. A.2 this is modeled by using a polarized laser light. A schematic representation of the dipole is shown in Fig. A.1(a). This figure shows the top view of the sample plane (x-y). Collection axis (z) is normal to the sample plane. Gray circle is representative of the analyzer which is rotating in the detection path. Gray line connecting the zero point of the analyzer to 180 deg. shows the analyzer axis in which light is transmitted. Orientation of the analyzer axis in this figure is the status at the starting point of the measurements. Dipole is oriented in-plane with 90 degree phase lag with respect to the analyzer axis at the beginning of the experiments. With starting the measurements motor rotates the analyzer with a speed of $3.84 \pm 0.3 \text{ sec}/\pi$. Arrival time of photon stream can be converted to angular modulation using the motor calibration. In the selected example what is expected is to see maximum of the modulation after 90 degree rotation of the analyzer. At the starting point since analyzer axis is normal to the dipole orientation the minimum should occur.

Figure A.2 (a) shows the results of this measurements. X-axis is the angular position of the analyzer which covers three complete rounds ($3\pi = 1080\text{deg.}$). Y-axis is the intensity of detected photon at each angle of the analyzer axis. As it can be seen at the beginning (zero degree) photon intensity is minimum which corresponds to the 90 degree phase difference between the analyzer axis and dipole orientation. While analyzer rotates and approaches the 90 degree ($\pi/2$) intensity of the detected photons increases to the maximum and falls off into the minimum after 180 (2π) degree traveling the analyzer. Intensity increases again while the analyzer turns towards 270 degree ($3\pi/2$) and goes off after one complete turn (2π) of the analyzer. Due to the fact that laser light used in this experiments is highly polarized, intensity modulation is complete. Meaning at $0, \pi, 2\pi, \text{ect.}$ intensity has vanished to zero. With this technique the in-plane angle of the

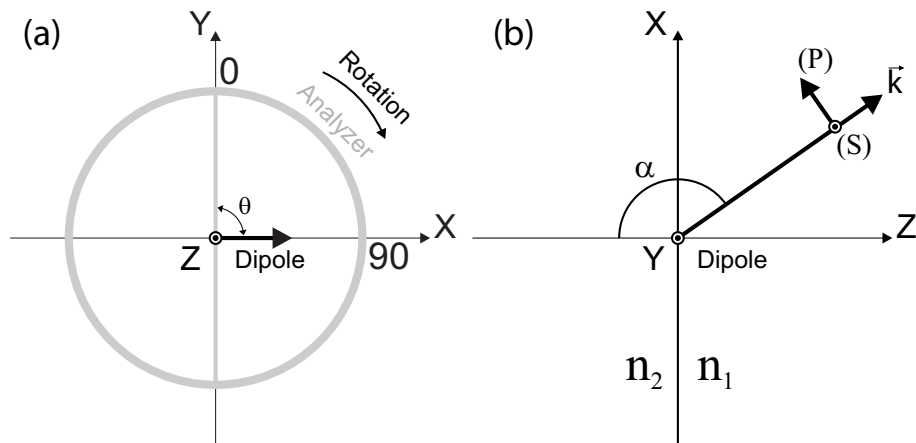


Figure A.1: (a) Coordinate system for polarization measurements. The x-y plane is the sample plane which is normal to the z-axis which corresponds to the collection axis. Gray circle is representative of the analyzer with 0-180 line which show the direction through which light passes the analyzer. Orientation of the analyzer is shown for the starting point of the measurements while it rotates during the measurements. One dipole which zero out-of-plane angle, on the sample plane is shown. Orientation of the dipole moment is 90 degree phase lag with respect to the analyzer at the starting point of the measurements, i.e. $\theta = 90 \text{ deg.}$. (b) Light emitted in direction \vec{k} , defined by spherical coordinates α and ϕ . α is defined with respect to z-axis relative to x-axis. Orientation of S and P is defined relative to \vec{k} -z plane. (\odot means pointing out of page).

dipole which the phase lag between the zero point and the first maximum can be determined. Since the orientation of the analyzer is done in a continuous fashion precision is high. The only limiting factor is motor calibration which is in the order of a few degrees. The only problem is this measurements is what is thought to be due to the movement of the laser focus on the APD. This can be estimated from the height of the maximum peaks in $\pi/2$ and $3\pi/2$. Although optics alignments have been done with high accuracy but apparently slightly off-axis position of the analyzer induces this artifact. This instrumental problem can be corrected via this calibration measurements. In the next section procedure taken for this correction is illustrated.

A.2 Data Correction

Following the experiments in the previous section small movement of the laser focus on the APD causes the artifact shown in figure A.2 (b). At 90 degree analyzer position intensity peaks up to 320 and 270 degree at 210. The difference between these two maximums is something in the order of %35. For correcting this artifact all the data point between 180 degree (π) and 360 degree (2π) are multiplied by this by the intensity difference ($\Delta I = \%35$). The result is shown in figure A.2 (c). After the data correction both peaks are about the same level and they prove a complete depletion of the intensity with respect to analyzer axis orientation. This correction was done for calculating the out-of-plane angle and depth of modulation as a measure of polarization of the emitting dipole which is in our experiments quantum dot. There in no influence introducing from the correction on the in-plane angle measurements. Since θ is directly measured by the phase difference of the starting point of the measurements and appearance of

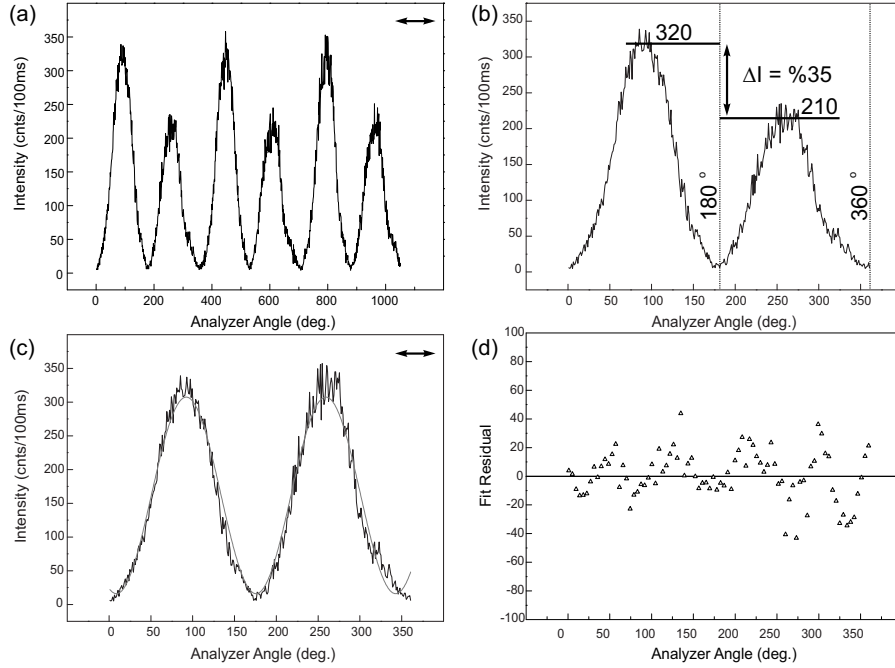


Figure A.2: (a) Emission polarization of a dipole oriented similar to figure A.1 without corrections, as measured. (b) Selected angular range from (a) between 0 to 180 degree before correction. (c) The same as (b) after correction for the angles between 180 to 360 degree. Gray line is a fit to Sine-squared function. (d) Residual of the sine-squared fit in (c) with respect to original data.

the first maximum peak. Even without correction our measurements would lead to the same conclusion regarding phase change of the quantum dot in contact with the antenna.

In figure A.2 (c) gray line is a fit to sine-squared equation which confirms the dipolar behavior resulted from the data points (descriptions are in section 6.2). The dipolar behavior of the polarized laser light can be cross-checked looking at the residual of the Sine-squared fit and the original data points (figure A.2(d)). As it can be seen residuals are relatively low compared to original data points which increases the precision that our measurement system has for calculating the out-of-plane angle (ϕ) as well as modulation depth. Descriptions presented here imply that the data presented in table 6.1 are precise and reliable based on

the interpretation of a dipole in the free space which is in practice not the case.

A.3 Data Interpretation

As it was noted earlier data obtained by analyzer rotation in the emission pathway is interpreted assuming a dipole emitting the in the free space. In this case as it is shown in figure A.1(b) light is propagating in \vec{k} direction where x-y is the sample plane and z-axis collection axis. Dipole lies in the x-z plane with out-of-plane angle θ relative to x-axis. α and ϕ are spherical coordinates where α is relative to z-axis and ϕ relative to x-axis. In these situations S and P components relative to \vec{k} -z plane are the followings,

$$S(\alpha, \phi, \theta) = \frac{3}{8\pi} \cdot \sin^2 \theta \cdot \sin^2 \phi \quad (\text{A.1})$$

$$P(\alpha, \phi, \theta) = \frac{3}{8\pi} (\cos \theta \cdot \sin \alpha + \sin \theta \cdot \cos \phi \cdot \cos \alpha)^2 \quad (\text{A.2})$$

Equations A.2 and A.1 are only valid for radiation pattern of a dipole in free space placing the dipole on a dielectric substrate will have significant effects on the radiation pattern as formulated by Lukosz [179].

$$S(\alpha', \phi, \theta) = \frac{3}{2\pi} \cdot \frac{\cos^2 \alpha' \cdot \sin^2 \theta \cdot \sin^2 \phi}{\left\{ \cos \alpha' + n \cdot \cos \left[\sin^{-1} \left(\frac{\sin \alpha'}{n} \right) \right] \right\}^2} \quad (\text{A.3})$$

$$P(\alpha', \phi, \theta) = \frac{3}{2\pi} \cdot \frac{\cos^2 \alpha' \cdot \left\{ n \cdot \cos \theta \cdot \sin \alpha' - \sin \theta \cdot \cos \phi \cdot \cos \left[\sin^{-1} \left(\frac{\sin \alpha'}{n} \right) \right] \right\}^2}{\left\{ n \cdot \cos \alpha' + \cos \left[\sin^{-1} \left(\frac{\sin \alpha'}{n} \right) \right] \right\}^2} \quad (\text{A.4})$$

Where θ and ϕ stay the same and $\alpha' = \pi - \alpha$ and $n = \frac{n_2}{n_1}$ where n_2 is the

refraction index of sample substrate and n_1 is the refraction index of air. Equation A.3 and A.4 describe the radiation pattern for the dipole on the low refraction index side of the dielectric interface for other configurations reader is referred to reference [179].

Although introducing a dielectric interface has changed the radiation pattern drastically but qualitatively measurements done in section 6.2 are reliable. Since the environment for experiments with and without tip is the same for the quantum dot the changes in the emission polarization induced by the antenna as well as and conclusions regarding dipole-dipole coupling between antenna and quantum dot stay the same.

Appendix B

Photon Anti-bunching Measurements

Photon anti-bunching data was presented in section 6.3. The raw data points in figure 6.7 are the measured data which show a dip at zero time delay between successive photons. This confirms the anti-bunching behavior and the fact that system is producing a photon per excitation pulse and no more until excitation by the next laser pulse. Since excitation de-excitation path ways are exponential with respect to the lifetime of the quantum system. Another important information hidden in anti-bunching data is the lifetime of the two-level system. Therefore, in order to determine the lifetime of the system from anti-bunching measurements one has to fit exponential curves for each rise and fall for each peak. After fitting successive exponential growth and decay lifetime of the system can be determined by averaging over all the lifetimes which is shown in figure 6.7.

Figure B.1 shows the antibunching fits which is the same as figure 6.7. In order to obtain shown fits, lifetime factor in exponential fits was kept the same

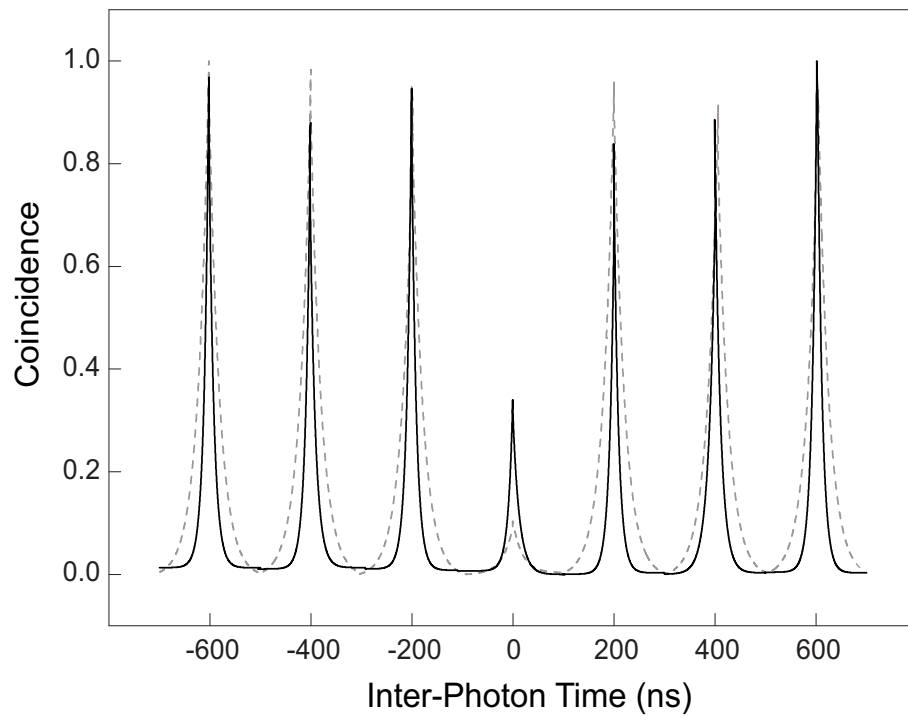


Figure B.1: Exponential fits for anti-bunching measurements done for nanocrystal in the free state (dashed gray line) and coupled to antenna (solid black line).

which was an average of the over all lifetimes as well as background factor which was also averaged overall. With having these two factors constant fitting was done again to display the fitted curve.

List of publications

Publications

- J.N. Farahani, D.W. Pohl, H.-J. Eisler and B. Hecht, "Single Quantum Dot Coupled to a Scanning Optical Antenna: A Tunable Superemitter", *Phys. Rev. Lett.* 95, 017401 (2005).
- J.N. Farahani, D.W. Pohl, H.-J. Eisler and B. Hecht, "Optical Antennas as Local Probes for Near-Field Optics", *in preparation for NanoLetters*.
- J.N. Farahani, D.W. Pohl, H.-J. Eisler and B. Hecht, "Emission Characteristics of Nanocrystal-Antenna System", *in preparation*.

Talks

- "Field Enhanced Scanning Near-Field Optical Microscopy Based on Nano-Optical Antennas", The 8th International Conference on Near-field Optics and Related Techniques (NFO8), September 2004, Seoul, Korea.
- "Optical Microscopy with Optical Antennas: far beyond the diffraction limit", BioNano Conference, January 2005, Lenzerheide, Switzerland.
- "Metallic Nano-Structures near Single Fluorophores", December 2005, ETHZ, Zurich, Switzerland.

Acknowledgements

First of all I would like to acknowledge my supervisor Prof. Bert Hecht for giving me the opportunity to do my Ph.D. in his group. His scientific and financial support provided the way to complete my thesis. I would like to acknowledge his endurance to my stupid questions. I would like to appreciate Dr. Hans-Juergen Eisler whose fascinating scientific discussions and encouragement contributed a lot to current work. I was overwhelmed having the chance to work with him. Stimulating discussions with Dieter Pohl have always been joyful.

I thank other members of nano-Optics group, like: Andreas, Jacqueline, Julien, Peter, Senta and Yoriko. Mechanical workshop colleagues who helped a lot in designing different components in the lab are deeply acknowledged. Labmates biophysicists, Doctor Willi and the Indian guy for times that we sent together are thanked. I thank the rest of the people in the Physics institute for being around: Denis, Audrius, Masoud, Bill, Jurg, Reza, (theoretical) Luca, (experimental) Luca, Mark, Timothy, Iris, Ani and the rest of the people that I do not remember now.

This thesis, and most other things that I have (except my skis) are dedicated to my Mother, to whom I owe the most. I will be trying happily repaying you as much as I can. Thank you Mom! for raising such a great boy!

Curriculum Vitae

Personal Information

Full Name: Javad Najafabadi Farahani

Birth: 21 September 1978 in Arak, Iran

Languages: Persian (*native*), English (*fluent*), French & German (*moderate*)

Marital Status: Single

Education

1992-1996 Diploma

High School Education

1996-1999 B.Sc.

Materials Science & Engineering,

Iran University of Science & Technology, Tehran, Iran.

1999-2001 M.Sc.

Materials Science & Engineering,

Iran University of Science & Technology, Tehran, Iran.

Thesis: Fabrication and Characterization of Alumina-Carbon Composites.

2002-2006 Ph.D.

Experimental Physics: Nano-Science,

University of Basel, Basel, Switzerland.

Thesis: Single Emitters Coupled to Bow-Tie Nano-Antennas.